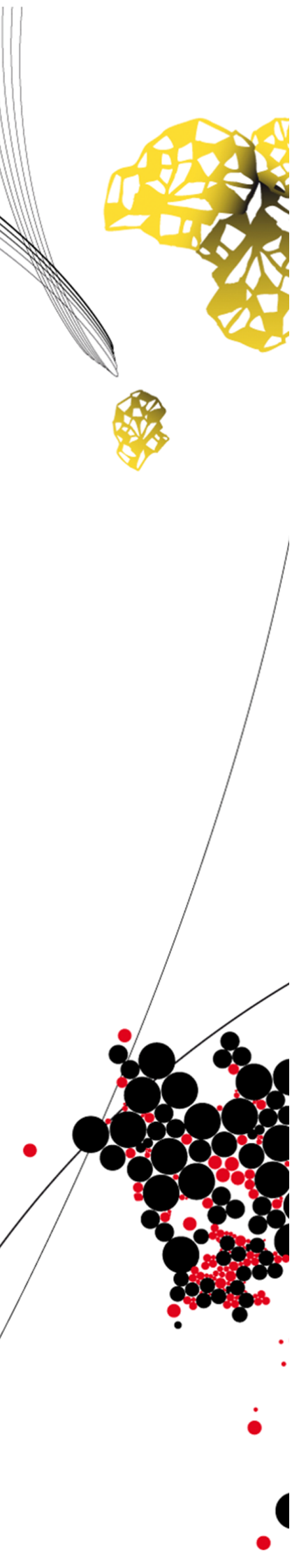

UNIVERSITY OF TWENTE.

Faculty of Engineering Technology

Development of an ice accretion code suitable for mixed-phase icing conditions

M.Sc. Thesis

Pim Adriaan Bullee

January 2015 - December 2015

Supervisors:
ir. E. Norde
dr. ir. E.T.A. van de Weide
prof. dr. ir. C.H. Venner
dr. ir. A.K. Pozarlik

Engineering Fluid Dynamics Group
Faculty of Engineering Technology
University of Twente
P.O. Box 217
7500 AE Enschede
The Netherlands

Document number
225

Acknowledgments

First of all I would like to thank my daily supervisor Ellen Norde. She helped me through all the steps in the process of research and writing this report. She is by far one of the more pleasant persons to work with that I know. I really appreciate here for always being available for questions and willing to help me and show me the right direction.

I would also like to thank my other supervisor Edwin van de Weide. During the first phase of this research I was worried that I was not making progress fast enough. He helped me through this phase by providing me with the insight that with a big project comes a long period of starting up.

More generally I would like to thank the members of the group of Engineering Fluid Dynamics. From the very first moment that I decided to join the Masters program from this group, I enjoyed the no-nonsense attitude and approachability of its members. My experience is that the staff is always willing to help with questions relating to courses, an internship, career choices, and all sorts of practical matters.

My brother Jan-Willem Bullee provided me with useful comments on my academic writing. His input always makes me review my work from a different perspective. Not only the details that he pointed out, but also the comments on the structure and flow of the report were of great use. I think this report has really benefited from his input.

Finally I would like to thank you, for your interest in my work and reading my Masters Thesis. I spent almost a year of my life working on the research presented in this report and I consider it to be the crowning glory of my academic career so far.

Summary

Ice formation on aircraft, or simply aircraft icing, is since long been recognized as a threat towards safe aircraft operation. It is the result of meteorological circumstances and an important object of study in the field of aeronautics. It has only been since the beginning of this century that meteorological and accident investigation revealed that aircraft engines are also vulnerable to icing conditions. When large amounts of ice crystals enter the engine, they can form a heat sink and accrete on the cooler parts inside the engine. Especially the first stages of the compressor, where the temperature is around the freezing temperature of water, are sensitive to these phenomena.

Current ice accretion prediction models are not suited to describe these phenomena. Traditionally, icing is caused by supercooled liquid droplets naturally present in the air. In the case of engine ice accretion, ice crystals, which are also naturally present in the air, also play an important role. Icing codes are based on the principle of the Messinger model, a one-dimensional equilibrium energy balance, which uses the equilibrium temperature of a surface to study ice growth.

Impact parameters for the Messinger model include a particle impingement distribution on the surface. This distribution is determined from the trajectories of the ice crystals and water droplets in the flow around an obstacle. This distribution is a measure for the amount of mass that impacts the surface and is the input for the energy and mass balance on the surface. From the energy and mass balance the surface temperature and the thickness of the accreted ice layer can be solved.

Ice crystals show a different behaviour from supercooled liquid water droplets. Upon impact with a surface they are expected to either fully rebound and remain intact, scatter and partly rebound or fully scatter without rebounding. Parameters important in this process are the kinetic energy and the size of a particle, but also the condition of the surface. A surface can be covered with ice, water or with neither of them. Ice crystals impacting a surface covered with ice can lead to erosion. Water on the surface can be splashed by the impacting surface and ice crystals impacting a dry surface are expected to bounce.

A mixed-phase ice accretion prediction code has been developed in the research described in this report. This code assumes that al the particles stick to the surface upon impact. The erosive action is accounted for by an empirical model that effectively reduces the amount of impinging ice crystals. The phenomena of mass evaporation from the surface have been revised. The influence of these phenomena is shown to be only minor.

In the context of an European project, the High Altitude Ice Crystals Consortium, a number of ice accretion codes have been extended to mixed-phase icing conditions. These extended codes are analysed and used together with the results from wind tunnel experiments to compare results generated by the newly developed code. A number of test cases do give results comparable to the numerical results from other codes, whereas other results are quite different. The aim of this research was however to develop a generally applicable mixed-phase icing model. The codes from which results were compared in this report had either a limited range of application or were built upon a large basis of expertise in ice accretion modelling.

From the tests performed with the newly introduced accretion model is concluded that the mechanisms of erosion and particle impingement are very important for a mixed-phase ice accretion code. In order to build a more accurate ice accretion model, it is therefore strongly suggested that these mechanisms are researched and taken into account in an updated version of the current mixed-phase ice accretion model.

Nomenclature and abbreviations

Cp	specific heat [J/(kg K)]
ds	length of a surface element [m]
d	particle diameter [m]
f	freezing fraction
H	enthalpy [J]
$\dot{H}$	enthalpy flux [J/s]
h_conv	convective heat transfer coefficient [m/s]
h_m	convective mass transfer coefficient [m/s]
Lh	latent heat [J/kg]
m	mass [kg]
$\dot{m}$	mass flux [kg/s]
p	pressure [Pa]
Q	heat [J]
$\dot{Q}$	heat flux [J/s]
R	gas constant
r	recovery factor
T	temperature [K]
U	velocity [m/s]
V	volume [m^3]

Dimensionless numbers

Pr	Prandtl number
Sc	Schmidt number
St	Stanton number
Le	Lewis number

Greek symbols

β	catching efficiency
η	fraction
ρ	density [kg/m^3]

Subscripts

0	stagnation or total
d	droplet
e	edge of boundary layer
f	freezing
ic	ice crystal
rec	recovery
s	surface
w	water
∞	at infinity upstream

Abbreviations

HAIC	High Altitude Ice Crystals
IWC	ice water content
LWC	liquid water content
TWC	total water content

Contents

Chapter 1

Introduction

The formation of ice on an aircraft, or simply aircraft icing has been the subject of study for many years [32]. Icing is a result of meteorological circumstances and can occur in flight as well as on the ground. A study by Petty and Floyd showed that in a period of 19 years between 1982 and 2000 icing caused 583 accidents with over 800 casualties [32]. Although no statistics are know from more recent years, it is safe to assume that aircraft icing is still causing accidents. Aeroplane manufactures are obliged to demonstrate safe aircraft operation in icing circumstances in order to comply with certification rules. Flight performance tests to demonstrate aircraft safety and wind tunnel experiments in general are very expensive. It is therefore desirable to use numerical models to study the behaviour of aircraft components. These kind of models are cheap and can easily be adjusted to simulate different operational conditions. In this report a numerical model is developed and evaluated which deals with the most recently discovered icing threat that compromises aircraft safety.

Ground icing is the result of natural precipitation freezing to the aeroplane. Although undesirable and possible dangerous, it is relatively easy to handle. The aeroplane is after all still on the ground. In flight icing therefore poses a greater threat, since it is of direct influence on the performance of an aircraft. It occurs when an aircraft flies through clouds consisting of supercooled droplets. A supercooled droplet is a drop of liquid water below freezing temperature. This is an unstable state and an input of energy or a nucleus to seed on (for instance a dust particle or sand grain) will make the drop transit to its stable state at that temperature, which is ice. When such a supercooled liquid drop hits the surface of an aeroplane it will experience a more than sufficient input of energy and it will therefore freeze at the surface of the aircraft [12]. Ice on aircraft wings can reduce the lift generated by the wings and increases the drag and weight of the wings. Also the controllability of the aircraft can be reduced due to ice growth on control surfaces such as the ailerons, rudder and elevators, ultimately leading to unsafe situations [31].

Recent aircraft incidents have shown that current certification rules are not sufficient to ensure safe operation in certain specific meteorological circumstances [12]. Among these specific circumstances are for instance Supercooled Large Droplets, subject of the European EXTICE project, which ran for four years between 2008 and 2012. In this project the group of Engineering Fluid Dynamics from the University of Twente contributed through the work of among others Hospers [17] and Norde [29].

It was discovered that ice crystals present in the air can also pose a possible threat to aircraft safety [24]. The altitude of 22.000 feet ($\sim$ 6700 metres) is assumed to be the upper limit for the existence of supercooled liquid water. Above this altitude (or for temperatures below -40 degree Celsius) water is expected to be in the form of ice particles [24]. Ice particles bounce of the external surface of the aeroplane, since the body panels are also at a temperature below zero degree Celsius. So at a flying altitude above 22.000 feet, aeroplanes can be considered to be safe from external ice growth from supercooled droplets. At these altitudes however, over 100 engine power loss events were reported since 1990 [12]. Following the suggestion by Mason et al., it is strongly believed that this engine failure is largely caused by ice particles that enter and accrete in the core of the engine [9, 12, 24, 40]. It is very likely that this mechanism consists out of ice particles adhering to warm surfaces inside the engine, forming a heat sink to the metal surface. This surface will cool down, allowing the formation of a

location suitable to mixed phase ice accretion: a mixture of liquid and ice particles on the surface [24].

The goal of the research described in this report is to create a computer model that predicts the ice shape on the surface as a result from flying through specified icing conditions. The input for the model is based on provided information on the amount of water droplets and ice crystals impacting the surface. Existing computer models that predict the ice shape on the surface only take the effect of supercooled droplets into account, which is insufficient for the above described mixed-phase conditions.

1.1 Ice accretion on jet engines

Ice accretion on aircraft engines can be caused by supercooled liquid droplets and mixed-phase or glaciated icing conditions. The supercooled droplet environment is well documented and regulated by for instance the FAA and EASA, the aviation authorities of respectively the United States and the European Union. This environment is commonly observed in a variety of clouds and atmospheric conditions below the freezing temperature of water down to temperatures of -15 degree Celsius. In rare cases supercooled liquid droplets are even reported in conditions nearing the edge of their existence at -40 degree Celsius [24]. For jet engines the components sensitive to supercooled liquid droplet ice accretion are those with a temperature below the freezing temperature of water. In the case of, for instance, a turbofan engine as depicted in Figure 1.2, these are the inlet lip, fan spinner, fan blade and the stators in front and directly behind the fan [24]. Examples of these are shown in Figure 1.1, by courtesy of aerospaceweb.org cited in [2]

Figure 1.1: Examples of ice accretion due to supercooled droplets on different parts of a turbofan engine. From left to right ice accretion is shown on the spinner of the fan, near the tip of the fan blades and near the base of the fan blades on the pressure side in a close up view [2].

Possible effects from ice accretion on these positions include:

- damage to structural components due to ice shedding from the inlet or the fan;
- malfunctioning sensors caused by ice blockage, resulting in control issues;
- performance instabilities as a result of shed ice entering the core of the engine;
- increased or heavy engine vibrations due to added, unevenly distributed weight from ice on the fan blades.

These effects are all well documented and are taken into account in engine design rules.

The effects of the glaciated and mixed icing environment are less well known and documented than the effects of the supercooled liquid environment. A collection of 46 engine powerloss events from commuter and large transport aircraft in daily usage was documented and analysed in 2006 by Mason et al. [24]. From this analysis it is believed that ice particles present in the glaciated and mixed icing environment can enter and accrete in the core of the engine, without leaving ice accretion on the external (engine) parts of the aeroplane. Areas in the core of the engine that are sensitive to this type of ice accretion are the stages of the low pressure compressor indicated in Figure 1.2.

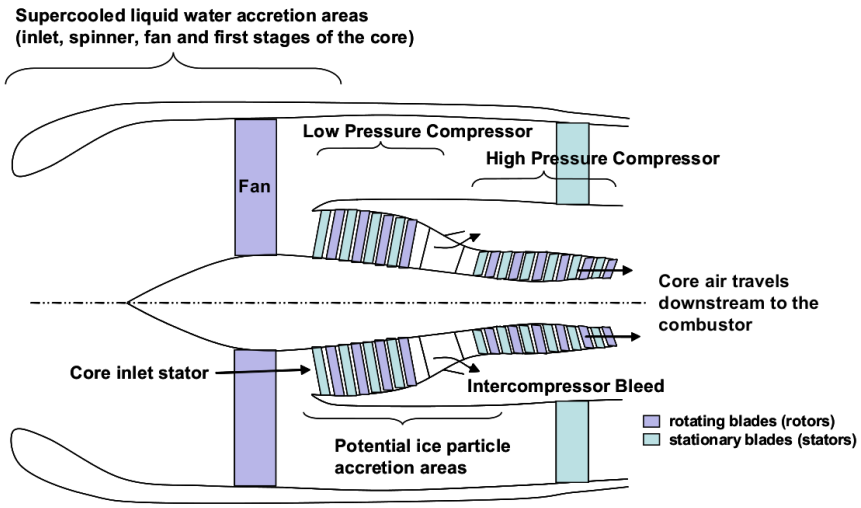

Figure 1.2: Schematic overview of the compression stage of a typical turbofan engine. Indicated are the areas sensitive to different types of ice accretion. Figure is adapted from Mason et al. [24].

1.2 The High Altitude Ice Crystals program

Since the 1990's, more than a hundred weather related in-flight engine power-loss events have been reported [24]. This was reason enough for the scientific and regulatory community to conclude that regions of high ice water content impose a possible danger to aircraft and extra research was required to gain insight in the origins, composition, detectability of such regions and their influence on aircraft flying through regions of high IWC (ice water content). In these studies a difference is made between clouds of ice crystals, called glaciated icing conditions and clouds formed by a mix of supercooled droplets and ice crystals, so called mixed-phase icing conditions [12].

One of the efforts to gain more understanding of these phenomena is the European HAIC (High Altitude Ice Crystals) project. Launched in 2012, its objective is to anticipate the regulation change with respect to the glaciated and mixed-phase icing conditions by developing and providing numerical tools and test facilities to investigate the influence of these conditions to aeroplane and engine performance, as well as detection and awareness systems to detect regions of high IWC [12]. It is a four years programme in which 37 institutes, universities and companies from fourteen countries work together to realize the above stated objective. Partners include aeroplane and engine manufacturers such as Boeing, Airbus, General Electric and Rolls Royce, research institutes such as NLR, DLR, ONERA and INTA, the universities of Braunschweich, Darmstadt and Twente as well as government agencies such as NASA, Météo-France and the Australian Bureau of Meteorology [12].

The activities of the HAIC project are split up in seven sub-projects, consisting of multiple work packages. The Engineering Fluid Dynamics group of the University of Twente contributes to sub-project six: HIWC Tools & Simulation Development. The objectives are to (co-)develop computer models for the distribution of ice and liquid water in the fan and compressor of a jet engine, predicting and modelling the impingement and accretion of the particles on the fan and compressor blades and to participate in the definition of a validation test case of ice-particle accretion phenomena in the compressor stages of a gas turbine [1].

1.3 Ice particles and ice accretion

Clouds consisting of supercooled water droplets and ice crystals are formed by thermal convection, the updraft of warm air near the ground into the higher and cooler layers in the atmosphere, illustrated in Figure 1.3. With this upward flow, water vapour naturally present in the air is carried to these higher and cooler regions. Along this trajectory the water vapour cools down and condenses into

a liquid state. When a certain height is reached, the temperature drops below the freezing point of water at 273.15 Kelvin. This corresponds to a height of 2400 metres as defined by the standard atmosphere [5]. The water in the cloud is now in supercooled state and will maintain this state until an external disturbance or seeding particle is introduced, allowing the water molecules to form the necessary hydrogen bonds to turn into ice. When the humidity at the ground is high, for instance in the tropics, the total water content will also be higher at higher levels in the atmosphere.

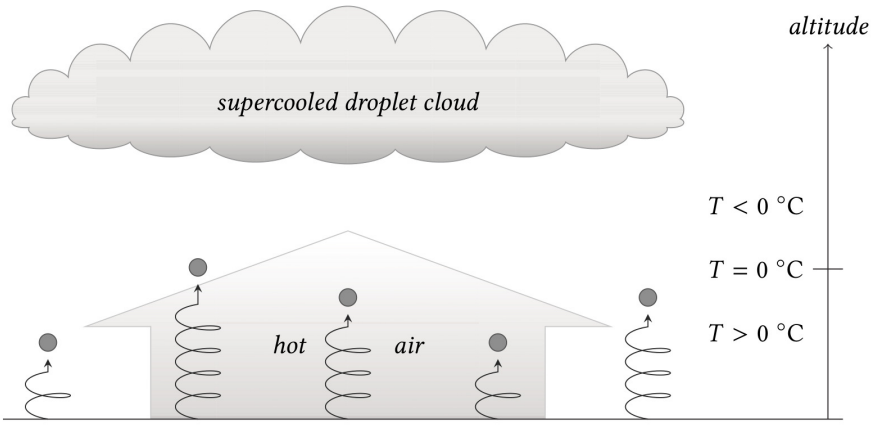

Figure 1.3: Sketch of the formation of a cloud consisting of supercooled droplets, as adapted from Hospers cited in [17].

Ice particles are usually found in the higher levels of the atmosphere, above the freezing level of 6700 metres as mentioned earlier on on Page 1. In general more heavy weather circumstances are required to form clouds consisting of ice crystals. Examples of this heavy weather include anvil clouds, strong wind shear and turbulence, heavy rain, hail, lightning and high water contents. The ice particles can have different shapes and sizes. The smaller particles are on the micron scale, consisting of single ice crystals. The larger particles are aggregates of multiple crystals sticking together, snow flakes, or crystals which have collided with supercooled droplets, forming more dense and spherical particles such as (soft) hail. Hailstones can grow to sizes of multiple centimetres [12]. The smaller the ice particles, the harder they are to detect by the onboard radar of an aeroplane [24]. This radar system is used to detect rain clouds and areas of bad weather which are then avoided by the pilot of the aeroplane.

Ice accretion occurs when the supercooled liquid droplets collide with, for instance, the wing of an aeroplane. Upon impact the droplet freezes almost instantaneously, forming a layer of ice on the wing. When there is a combination of liquid (supercooled) water and ice crystals, the so called mixed-phase, this process is less straightforward. Although the number of experimental studies on the topic of mixed-phase ice accretion is limited, their results indicate that a small amount of liquid water on the surface is required to catch the ice crystals and prevent them from bouncing of the surface. Hence, in order for the ice crystals to contribute to the accretion of ice, both the temperature of the air stream containing the ice and water particles and the surface upon which they impact should equal, or be just above the freezing temperature of water. When the temperature drops to far below the freezing temperature, the ice crystals will bounce off and the ice accretion will be due to the supercooled liquid droplets only. For temperatures well above the freezing temperature of water, no ice accretion will occur, since not enough ice crystals are present in the flow to sufficiently cool the surface [18].

Apart from the ambient temperature, a number of factors are of influence on the position, shape and size of the ice accretion on the surface. These include the humidity of the air, the roughness of the surface, flow speed and the icing time, which is the period in which the surface is subjected to the ice and water particles impacting the surface [17].

The trajectory followed by the particles in the flow around the object they encounter, for instance the wing of an aeroplane, is mainly determined by their size. From the forces acting on a particle changing directory, the gravity, buoyancy and drag forces are dominant. The latter of these three forces is of major influence on the trajectory of a particles [17]. It is however questionable if this simplification is also valid for rotating flow machines.

Generally two different types of ice accretion are recognised: rime-ice and glaze ice.

Rime-ice is formed when all the water in the impinging droplets freezes instantly upon impact. This usually occurs when the airspeed and temperature are low and the water content of the air is also relatively low. The result is that the released latent heat of freezing is not enough to increase the local temperature to the freezing point. Hence all the water in the droplets freezes at impact, resulting in a dry, white opaque ice layer, with a density lower than that of the impinging liquid water. Generally rime-ice has a streamlined shape [17]. The effect of the ice crystals in the mixed-phase rime-ice accretion is small [18]. This can be explained as being the result of the supercooled liquid droplets freezing upon impact, forming a solid, hard layer of ice upon which the ice particles simple bounce of. This is similar to the particles bouncing of the outside surfaces of an aeroplane. An example of rime-icing is shown in Figure 1.4a, adapted from the work of Horák et al. [16].

Glaze-ice is formed when only part of the water in the impinging droplets freezes on impact. It occurs when the water content of the air and the airspeed are relatively high and the temperature is close to, though still below, the freezing temperature of water. In this case the released latent heat of freezing is sufficient to increase the local temperature above the freezing temperature. The result of this is that only part of the water in the impinging droplets freezes at impact, whilst the rest of the water runs back along the aerofoil surface. This runback water often freezes further downstream. The result is a transparent layer of ice, with a density close to the density of the impinging liquid water. Usually this kind of ice accretion has a irregular, non-aerodynamic shape jeopardizing the aerodynamic characteristics of the aerofoil [17]. In mixed-phase glaze-ice accretion, the ice crystals present in the flow are of influence on the resulting ice shape on the surface [18]. This related to the mechanism by which the ice crystals stick to the surface, which requires the present of liquid water. An example of glaze-icing is shown in Figure 1.4b, adapted from the work of Horák et al. [16].

(a) Example of rime-ice [16].

(b) Example of glaze-ice. [16]

1.4 Modelling of icing

Over the years a variety of computer codes have been developed to predict ice accretion on wings and other aerodynamic shapes and surfaces due to (supercooled) liquid droplets. Examples of these include LEWICE, developed at the NASA Lewis Research Center [34], ONERA2D/3D, by ONERA and FENSAP-ICE, from Newmerical Technologies [4]. In the group of Engineering Flow Dynamics from the University of Twente two codes relevant for this research have been developed, 2DFOIL-ICE, from which the first version originates from 1996 [21] and Droplerian which is written by Hospers [17]. The development of computer codes that predict ice accretion in mixed-phased and glaciated icing conditions is relatively new and is one of the objectives of the HAIC project [12]. Every code will have a slightly different approach to predict ice accretion. Therefore it is useful to compare numerical

results not only to experiments, but also to results generated by other codes. This makes it possible to comment on the behaviour of certain parts of the code.

Numerical models to describe the process of ice growth generally involve three steps: 1) solving the flow field, 2) calculating the particle (water droplet and ice crystal) trajectories and 3) the actual ice accretion process. These three steps can be coupled, since the change in shape of the aerofoil due to ice accretion will also influence the flow field, resulting in a repeating process [6].

The Messinger model

From the first two steps the number of particles that impact a certain surface location can be calculated. This so called catching efficiency is the input for the third step and can be used to determine the amount of ice that accretes to the surface. This means that a mass and a energy balance must be created of the incoming water droplets to determine the fraction of water that freezes to the surface. The unfreezing fraction will remain present as water and flows off downstream to the trailing edge of the aerofoil. This energy balance was first set out in 1953 by Bernard Messinger [25]. In its original form, the Messinger model is a one-dimensional equilibrium energy balance, employing the equilibrium temperature of an insulated and unheated surface to study ice growth [27].

Improvements to the original Messinger model have been made by various authors, recognising the limitations of the original model [7, 27, 34]. As part of the HAIC project, the extension to mixed phase conditions has to be made to simulate the ice accretion due to ice crystals [18]. The goal of the research presented in this report is to develop such an extension.

Chapter 2

Literature review

Various authors have already suggested extensions to current ice accretion codes to make them suitable to mixed-phase icing conditions [3, 11, 18, 19, 40, 43]. A number of them will be reviewed in this section. Also the mechanisms important in mixed-phase ice accretion will be discussed. These are for instance the impingement of ice crystals: will they bounce from the surface or scatter into multiple piece, and erosion: the removal of pieces accreted ice by impacting ice crystals. The basis for the extension to mixed-phase icing is the Messinger model which was introduced in Section 1.4. This model will be examined in greater detail in this section. The models and procedures used to solve the flow field around an aerofoil and the trajectories of particles in the flow are introduced. Although these are not part of the model developed in the research presented in this report, it is useful to have knowledge on the origins of the input parameters. First however a study will be reviewed that describes and proves the threat that large concentrations of ice crystals pose to aircraft engine performance and flight safety.

2.1 The ice particle threat to jet engines

A flight test was performed with a multiple engine commuter aeroplane in the summer of 1997 in the state of Alabama, USA, close to a region of thunderstorms. The aircraft was equipped with a normal engine and a modified engine. The latter featured heated second stage compressor vanes, which are the blue stationary blades in the low pressure compressor in Figure 1.2. The temperature of multiple engine elements was measured and the the ice accretion on the external visible parts of the engine was monitored using video cameras. The low pressure compressor fan speed and measured compressor vane temperature of both engines are shown in Figure 2.1. The rotational speeds of the low- and high pressure compressor of the unmodified engine are shown in Figure 2.2. Both figures are adapted from Mason et al. [24].

Initially the cameras recorded no ice accretion on the external parts of the engine, only the presence of ice particles in the inlet flow. At the same time it is indicated by the rollback (reduced rotational speed) of the low pressure compressor and the decreasing temperature of the stators in the compressor of the unmodified engine (see Figure 2.1) that ice is accumulating at those positions. With increasing rollback, the engine became unable to power the anti-icing system. This resulted in ice accretion on the core inlet vanes (IGVs). The unmodified engine tested was a double shaft engine, hence the two graphs in Figure 2.2. From the rollback of the low pressure compressor N1, with the high pressure compressor N2 maintaining its velocity, can be concluded that the ice accretion takes place only on the low pressure compressor vanes, which is confirmed by (not provided) temperature measurements of the stator vanes closer to the core of the engine.

For commuter aircraft the engine power loss is commonly caused by rollback, resulting from ice accumulating. For large aircraft however, the loss in power is rather caused by ice building up and shedding in the core of the engine [24]. Events reported by Mason et al. for large aircraft include:

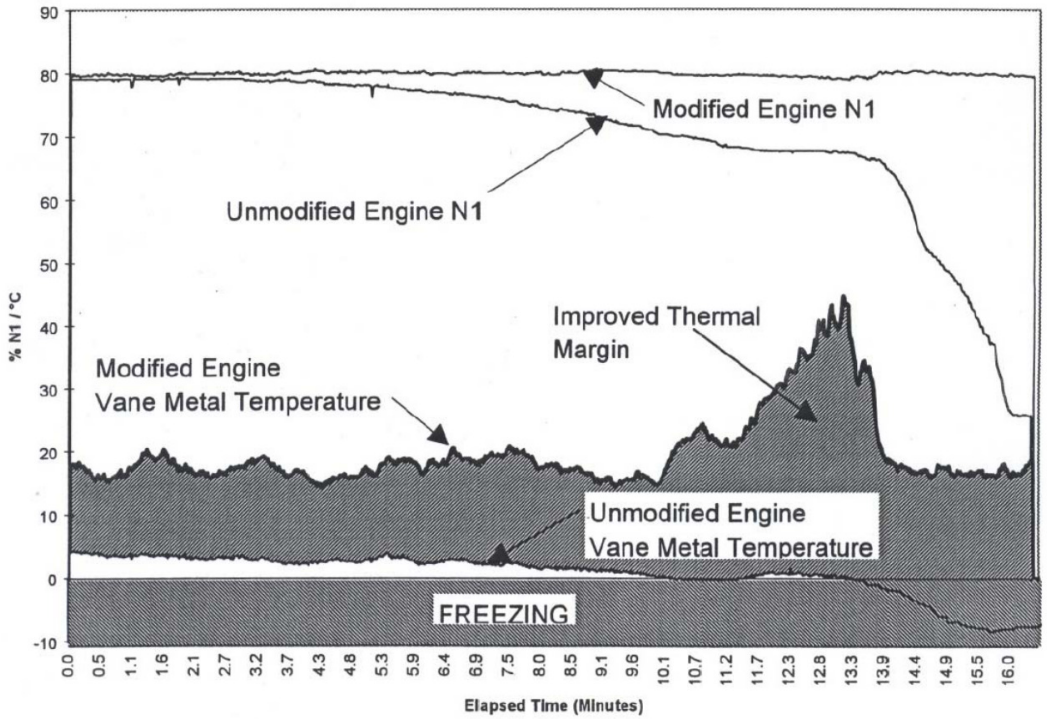

Figure 2.1: The compressor vane temperature and rotational speed of the low pressure compressor of the modified and unmodified engine [24].

- engine surge (sudden flow reversion) resulting in stall. This is caused by a combination of momentum and heat loss due to ice blockage and inefficiency of the compressor resulting from ice accretion;
- flameout, as the result of quantities of ice entering the combustion chamber and quenching the combustion;
- damage to rotor blades and vanes due to impacting ice. Usually the effects are minor, although events of blade release are also reported.

In all the reported cases of engine power loss, the engine was restarted after the event.

The results from the flight test and a case study of 46 engine power loss events bring Mason et al. to the hypothesis that ice particles can adhere to warm metal surfaces inside an aircraft jet engine. Upon doing so, the particles act as a heat sink until the surface temperature drops below the freezing point of zero degree Celsius, making the surface a suitable place for mixed-phase ice accretion. The resulting blockage of the flow in the engine and shedding of the accumulated ice into the engine is the cause of engine malfunction in regions of high ice water content. It is furthermore insisted by Mason et al. that regions of high ice water content, values up to 8 g/m^3 are reported, should be the subject of further research, as well as the (thermodynamic) process of mixed-phase ice accretion [24].

2.2 Particle trajectories and the flowfield

The behaviour of a continues, homogeneous and non-chemically-reacting flow is described by the Navier-Stokes equations. Solving the full Navier-Stokes equations is difficult. Meaningful numerical simulations of all the aspects of a flow, including viscous effects and heat-conduction, is beyond the current capacity of computers [14]. In a large number of practical applications it is fortunately sufficient to require knowledge of global flow characteristics determined by the mean flow. Therefore a number of models are derived from the Navier-Stokes equations to solve these mean flow characteristics. Examples include the Euler equations, which neglect influences from viscosity and heat

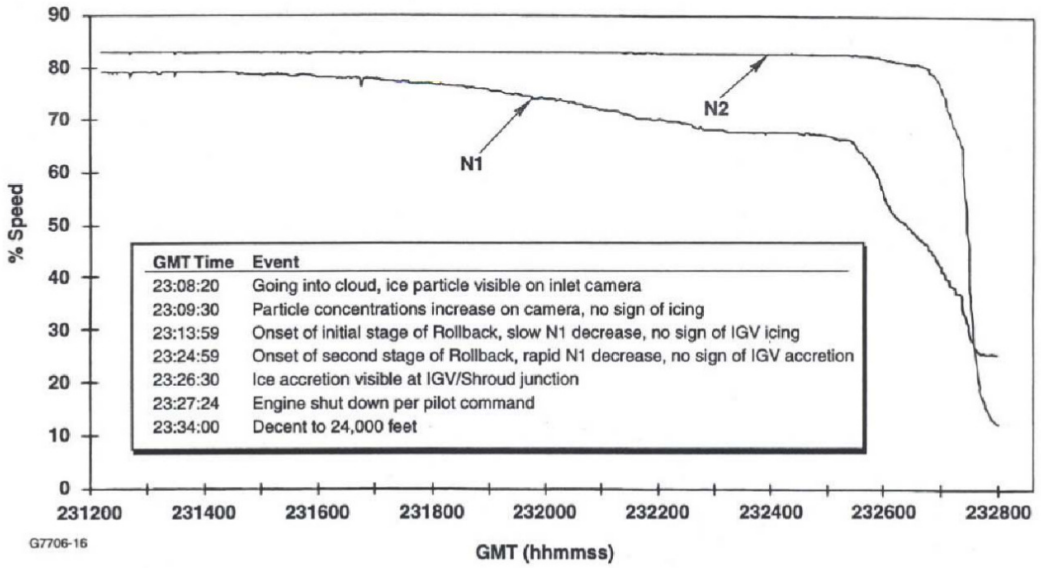

Figure 2.2: The low- and high pressure rotational speeds, denoted N1 and N2 respectively, of the unmodified engine, with an overview of the monitored events during the test flight [24].

conduction and the potential flow theory which also neglects distributed vorticity [14].

The particle trajectories are calculated from the flow field around an aerofoil. This can for instance be done by releasing the particles at a certain point in the flow field and tracing their trajectory. For each particle the velocity along its trajectory can be determined by integrating the equation of motion. The position after a time-step Δt can than easily be determined. For instance 2DFOIL-ICE and LEWICE follow this so-called Lagrangian procedure to calculate the particle trajectories [17, 34]. In 2DFOIL-ICE the dominant forces acting on the particle are assumed to be the gravitational and the drag force. The drag force is the result of the flow field working on the particle. The associated equation of motion is given in Equation 2.1.

$$m_d \frac{d\vec{U}_d}{dt} = \vec{F}_D + \vec{g} m_d \tag{2.1}$$

Here m_d and $\vec{U}_d$ denote respectively the mass and velocity of a (supercooled) water droplet. The drag force $\vec{F}_D$ in this equation is given in Equation 2.2.

$$\vec{F}_D = \frac{1}{2} \rho_a \left| \vec{U}_a - \vec{U}_d \right| \left(\vec{U}_a - \vec{U}_d \right) A_d C_d \tag{2.2}$$

In Equation 2.2 the subscripts a denote the air of which the flow field is composed, ρ_a is therefore the density of the air, and A_d and C_d are the cross sectional area of the droplet and the drag coefficient. Both Equation 2.1 and Equation 2.2 are adapted from the work of Hospers [17]. For solid ice crystals also the shape of the crystal is of influence on its trajectory. For particles with a sphericity ratio smaller than 0.5 a significant difference in particle trajectories was found compared to spherical particles [20].

In both 2DFOIL-ICE and LEWICE a potential flow field is calculated using a panel method. This makes it difficult to accurately solve multi-element aerofoils, since here viscosity plays an important role. In potential flow theory, an irrotational flow model is assumed, leaving no room for viscous flows which generate vorticity [14]. Please note that there are also Lagrangian solvers that do accept a solution from the Euler or Navier-Stokes equations. The disadvantage of using a Lagrangian approach is that finding the particle trajectories can be rather time consuming. Thereby a large number of particles have to be traced to find an accurate solution for the impact locations of the particles [17].

A visualization of a flow field is shown in Figure 2.3 using streamlines around a NACA 0012 profile. The streamlines are created from the velocity field of the air and indicate the direction a massless fluid element will travel at any point in time. The streamlines for the droplets or particles in the

same flow field would show a slightly different behaviour, following the same trend. At the stagnation point, located near the nose of the aerofoil in Figure 2.3, the flow is split up in two parts. One part flows over the top half of the aerofoil, the other part follows the lower half of the aerofoil. The two flows are rejoined at the trailing edge at the right end of the aerofoil. In the stagnation point the flow is decelerated to zero velocity, hence the name, after which it is accelerated over the aerofoil, reaching its maximum velocity.

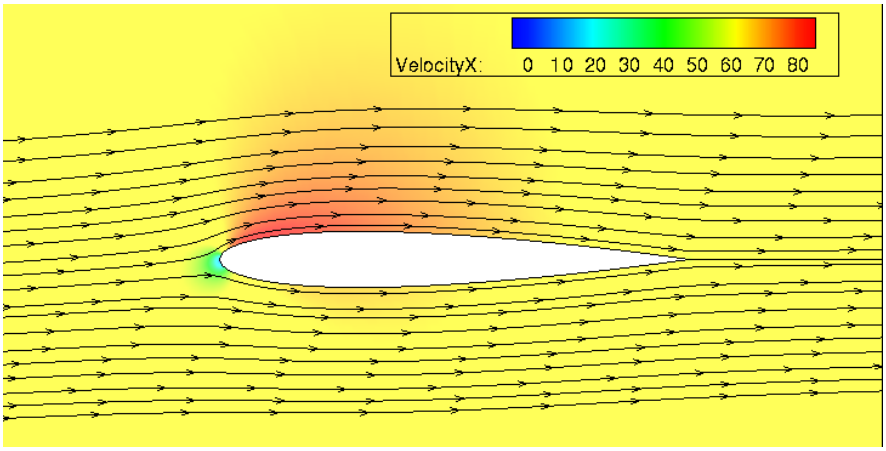

Figure 2.3: Flow field of the air around a NACA 0012 profile, visualized in Tecplot using streamlines.

An Eulerian tracking method is used in Droplerian which lacks the disadvantages of Lagrangian methods. Droplerian, a combination of the words droplet and Eulerian, accepts flow solutions from any model. This includes the potential flow model from 2DFOIL-ICE, but also solutions based on the Euler or full Navier-Stokes equations. Where a Lagrangian method describes the properties of a flow field as a function of time and the position or trajectory of a particle, an Eulerian method describes flow quantities as a function of position in space and time. In Droplerian the flow field of the air is used as input to calculate the velocity- and density field of the droplets around an aerofoil. This is done by deriving the governing equations for the water (droplet) phase as is shown in Equation 2.3 and Equation 2.4 which are adapted from the work of Hospers [17].

$$\frac{\partial \rho_d}{\partial t} + \nabla \cdot \rho_d \vec{U}_d = 0 \tag{2.3}$$

$$\frac{\partial \rho_d \vec{U}_d}{\partial t} + \nabla \cdot (\rho_d \vec{U}_d)\vec{U}_d = \rho_d \vec{f}_D + \rho_d \left(1 - \frac{\rho_a}{\rho_d}\right) \vec{g} \tag{2.4}$$

In Equation 2.4 the drag force is added as a surface force whilst the other two terms on the right hand side are the body forces represented by the gravity and buoyancy force. The latter being due to the difference in density between the air and water [17]. The expression for the drag $\vec{f}_D$ is slightly different from the expression in Equation 2.2. In this case, $\vec{f}_D$ is rather a drag acceleration term, as given in Equation 2.5 which is adapted from the work of Hospers [17].

$$\vec{f}_D = \frac{\rho_a \left|\vec{U}_a - \vec{U}_d\right| \left(\vec{U}_a - \vec{U}_d\right) A_p C_p}{2\rho_w V_d} \tag{2.5}$$

In this equation V_d denotes the volume of the droplets, C_d is equal to the term in Equation 2.2. Equation 2.3 and Equation 2.4 can be solved using a finite-volume method, of which details are described in [17].

From the calculated trajectories in the Lagrangian method a catching efficiency β can be determined. This catching efficiency contains information on the mass of particles impinging the surface. This is an important parameter in determining the amount of ice that accretes on the surface. The definition of the catching efficiency for the Lagrangian method is explained using Figure 2.4 adapted from the work of Hospers [17].

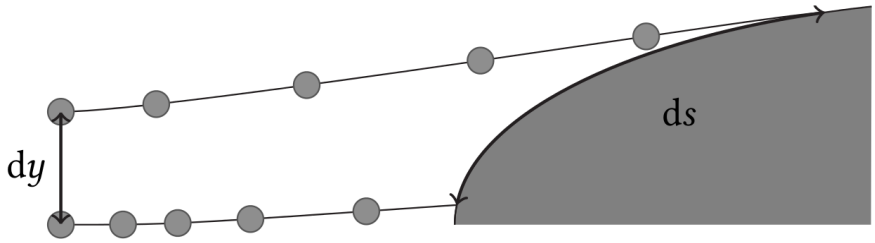

Figure 2.4: Measures used to define local catching efficiency for Lagrangian methods [17].

In Figure 2.4 the distance between the starting locations of two particle trajectories starting close to one another is denoted dy. The distance between their impact locations is called ds. The ratio between these two values says something about the amount of mass contained between the two trajectories from start to impact location. Hence the catching efficiency is defined as

$$\beta = \frac{dy}{ds}, \tag{2.6}$$

which is adapted from Hospers [17].

For the Eulerian method no information is known from the particle trajectory, since the flow field was calculated as a whole. Therefore in Droplerian a catching efficiency has been defined using the liquid water content (LWC) of the cloud, the local droplet velocity $\vec{U}_d$ and the local droplet density ρ_d. Here the local droplet density is the product of the volume fraction of water contained in the droplets α times the local water density near the surface of the aerofoil:

$$\rho_d = \alpha \rho_w. \tag{2.7}$$

The catching efficiency β for the Eulerian method is defined in Equation 2.8 which is adapted from Hospers [17].

$$\beta = \frac{\rho_d \vec{U}_d \cdot \hat{n}}{LWC \left| \vec{U}_{d,\infty} \right|} \tag{2.8}$$

In Equation 2.8 the LWC is written as LWC and $\vec{U}_{d,\infty}$ is the free stream velocity of the droplets, the velocity at a far upstream position. The normal vector $\hat{n}$ is defined as is shown in Figure 2.5 which is adapted from the work of Hospers [17].

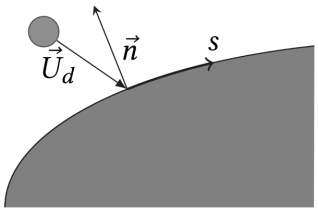

Figure 2.5: Local velocity- and normal vector as defined in the Eulerian method [17].

2.3 The Messinger model

The Messinger model describes the heat and mass balance of a thin and continues water film on top of an insulated surface. In its original form, the Messinger model features only supercooled water droplets. The effects of impinging ice crystals are not taken into account. Usually the model is evaluated at discrete positions starting from the leading edge of the aerofoil using a control volume method. Only the water fraction is inside the control volume, the liquid that freezes moves out of

the control volume to the ice layer. Unknowns are the surface temperature and the freezing factor f. This freezing factor denotes the fraction of water which freezes with respect to the incoming water. Using this ratio, the amount of ice growth and thus the ice profile can be predicted. The fraction of water which remains unfrozen $(1 - f)$ is assumed to flow into the next, neighbouring control volume. The four main assumptions for the original Messinger model are [18]:

1. The system is in a steady state, thus the transition from rime ice to glaze ice can not be described;

2. The water film covering the surface cannot break up or separate but has to constantly cover the surface;

3. There is no residual water, thus incoming droplets or ice crystals have to freeze or flow into the next control volume;

4. The surface and ice and water layers are isothermal and thus no heat conduction is possible.

The mass and energy balance used for the Messinger model are derived from the conservation laws of mass and energy.

The conservation of mass in an arbitrary control volume is given by the continuity equation in Equation 2.9 [22]. The continuity equation applies the principle that, nuclear reactions and relativistic effects aside, mass can not be created nor destroyed. Hence, for a volume placed in a flow, the difference between the mass entering and leaving the volume should equal the amount of mass accumulating in the volume. For a comprehensive derivation of the continuity equation is referred to chapter four of the book Fluid Mechanics by Kundu et al. [23].

$$\frac{\partial}{\partial t}\iint_V \rho_w dV + \int_{\partial V} \rho_w[(\vec{u}_w - \vec{u}_{\partial V}) \cdot \hat{n}]dS = 0 \tag{2.9}$$

Here $\hat{n}$ is the normal vector to the surface directed outwards of the control volume. The velocity of the moving boundary of the control volume is given by $\vec{u}_{\partial V}$. Due to the steady state assumption, the unsteady time term drops out. With V a closed volume and $\vec{u}_{\partial V} = 0$, Equation 2.9 can be reduced to

$$\int_{\partial V} \rho_w(\vec{u}_w \cdot \hat{n})dS = 0 \tag{2.10}$$

The contributions to the mass balance are:

- $\dot{m}_{in}$, the runback water flowing into the control volume, originating from the previous control volume;

- $\dot{m}_{out}$, the non-freezing runback water flowing into the next control volume;

- $\dot{m}_{imp}$, droplets being caught by the surface;

- $\dot{m}_{freeze}$, the fraction of water that freezes and moves out of the control volume;

- $\dot{m}_{evap}$, the fraction of water that evaporates into the layer of air outside of the control volume.

The mathematical relations of the mass flows are shown in Table 2.1. The control volume and the mass flow are shown graphically in Figure 2.6 which is adapted from Jacobs et al. [22]. A selection of the individual terms of the mass balance will be reviewed in further detail in the remainder of this chapter.

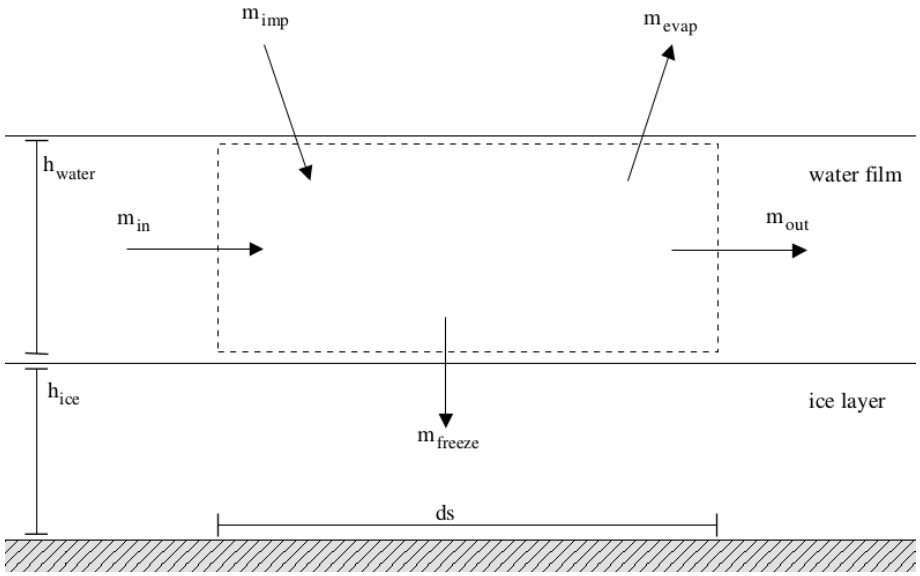

Figure 2.6: Graphical representation of the mass flow in the original Messinger model [22].

From Figure 2.6 the mass balance is stated mathematically in Equation 2.11.

$$\dot{m}_{imp} + \dot{m}_{in} = \dot{m}_{freeze} + \dot{m}_{out} + \dot{m}_{evap} \tag{2.11}$$

To relate the impinging droplets that freeze to the surface to the total amount of droplets impinging the surface, Messinger introduced the freezing factor f. This ratio between impinging and freezing mass is defined in Equation 2.12.

$$f = \frac{\dot{m}_{freeze}}{\dot{m}_{imp}} \tag{2.12}$$

In other studies a different definition is used, for instance Jacobs et al. define the freezing factor f as the fraction of the total amount water that enters the control volume [22]. This relation is presented in Equation 2.13.

$$f = \frac{\dot{m}_{freeze}}{\dot{m}_{imp} + \dot{m}_{in}} \tag{2.13}$$

When this freezing factor f is known for every discrete position on the surface, the resulting ice shape can easily be determined. The mass of water that freezes can be related to the thickness of the ice layer h_{ice} using the density of ice, the dimensions of the surface and the icing time, which is the duration of the exposure of the surface to icing conditions.

The mass balance can be rewritten by combining Equation 2.11 and Equation 2.13, resulting in an expression for the outflowing mass which is given in Equation 2.14.

$$\dot{m}_{out} = (1 - f)(\dot{m}_{imp} + \dot{m}_{in}) - \dot{m}_{evap} \tag{2.14}$$

In this equation there are two unknowns, f and $\dot{m}_{in}$. The latter is the unfrozen water from the upstream element, so ideally an additional equation is required to find the unknowns. Therefore the balance of the energy terms is introduced.

The conservation of energy in terms of total enthalpy H for an arbitrary control volume is given in Equation 2.15 by the energy equation [14]. The conservation of energy is in essence not much difference from the continuity equation. It sums al the contributing energy sources inside a volume and all the energy fluxes flowing in and out of the volume. All energy terms together should be in balance with each other. For a comprehensive derivation of the energy equation is referred to chapter four of the book Fluid Mechanics by Kundu et al. [23].

$$\frac{\partial}{\partial t}\iiint_V \rho E dV + \iint_{\partial V} \rho H[(\vec{u} - \vec{u}_{\partial V}) \cdot \hat{n}]dS = \iiint_V \rho \vec{u} \cdot \vec{f} dV + \iint_{\partial V} (\bar{\bar{\tau}}\vec{u}) \cdot \hat{n} dS + \iiint_V \dot{Q} dV - \iint_{\partial V} \vec{q} \cdot \hat{n} dS \tag{2.15}$$

The only contributions to the energy are from the mass and heat flowing in and out of the control volume. Hence, the terms related to external forces, viscous effects and sources can be neglected. The steady state assumption omits the time dependency, thus Equation 2.15 can be reduced to

$$\iint_{\partial V} \rho H(\vec{u} \cdot \hat{n}) dS = -\iint_{\partial V} \vec{q} \cdot \hat{n} dS \tag{2.16}$$

With H the total enthalpy and $\vec{q}$ the heat flux vector, the contributions to the energy balance are:

- $\dot{H}_{in}$, the change in enthalpy to bring the temperature of inflowing mass of runback water to the temperature inside the control volume;
- $\dot{H}_{out}$, the change in enthalpy related to the non-freezing runback water flowing into the next control volume;
- $\dot{H}_{imp}$, the enthalpy change to bring the droplets being caught by the surface to the temperature of the control volume;
- $\dot{H}_{freeze}$, the change in enthalpy related to the water moving into the ice layer;
- $\dot{H}_{evap}$, the enthalpy related to the fraction of water that evaporates into the layer of air outside of the control volume;
- $\dot{Q}_{Ek,imp}$, the kinetic energy of the droplets being caught by the surface;
- $\dot{Q}_{Lh,f}$, the latent heat related to the fraction of water that freezes and moves out of the control volume;
- $\dot{Q}_{conv}$, the energy lost due to convective cooling by the layer of air outside of the control volume.

These terms are also included in Table 2.1 where the arbitrary reference for zero enthalpy is the temperature of the volume. In the remainder of this chapter a selection of the terms and expressions will be reviewed in greater detail. The control volume and the energy flow are shown graphically in Figure 2.7 which is adapted from Jacobs et al. [22].

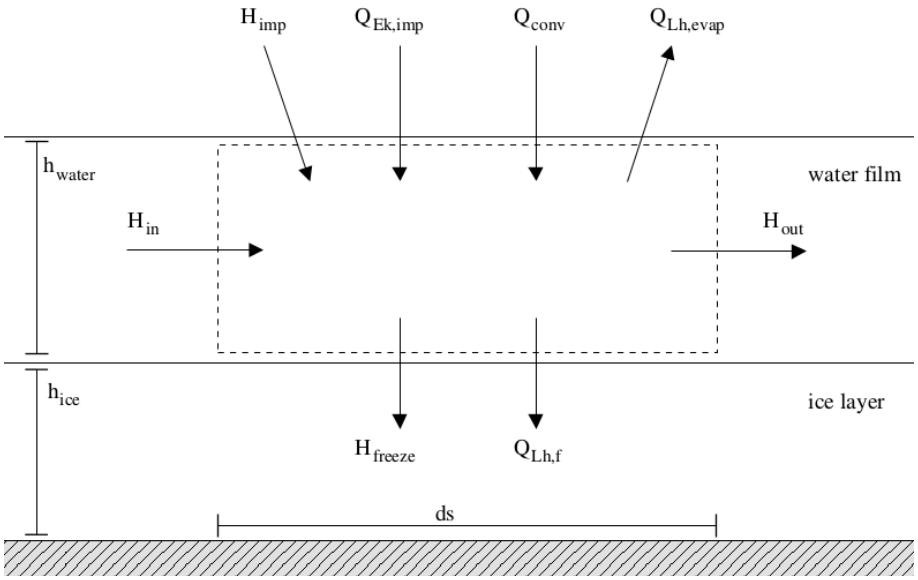

Figure 2.7: Graphical representation of the energy flow in the original Messinger model [22].

From Figure 2.7 the energy balance is stated mathematically in Equation 2.17

$$\dot{H}_{imp} + \dot{Q}_{Ek,imp} + \dot{H}_{in} = \dot{H}_{out} + \dot{H}_{freeze} + \dot{Q}_{freeze} + \dot{Q}_{Lh,evap} + \dot{Q}_{conv} \tag{2.17}$$

With this energy balance a new unknown is introduced, the temperature inside the control volume, or the temperature of the surface T_s.

In order to solve the energy equation and find the amount of freezing mass an assumption has to be made for one of the three variables after which the others van be solved. The procedure followed in LEWICE consists of first stating that the surface temperature is equal to the freezing temperature of water $T_s = T_f$ [34]. The first element for which the mass and energy balance is solved is around the stagnation point, since no runback water is flowing into this element. From the energy balance the freezing fraction f is solved. The value of the freezing fraction should be between one and zero $0 < f < 1$ to match the assumption of $T_s = T_f$. When $f < 0$ the surface temperature should be increased above the freezing temperature. This is done by setting $f = 0$ and solving the energy balance for T_s. Similarly, when $f > 1$, the freezing fraction is set equal to one $f = 1$ and a surface temperature below the freezing temperature is solved from the energy equation [34]. This procedure is shown graphically in Figure 2.8, which is adapted from the work of Hospers [17].

Figure 2.8: Flowchart for the routine of finding the correct freezing fraction rate and surface temperature in the LEWICE and Droplerian code [17].

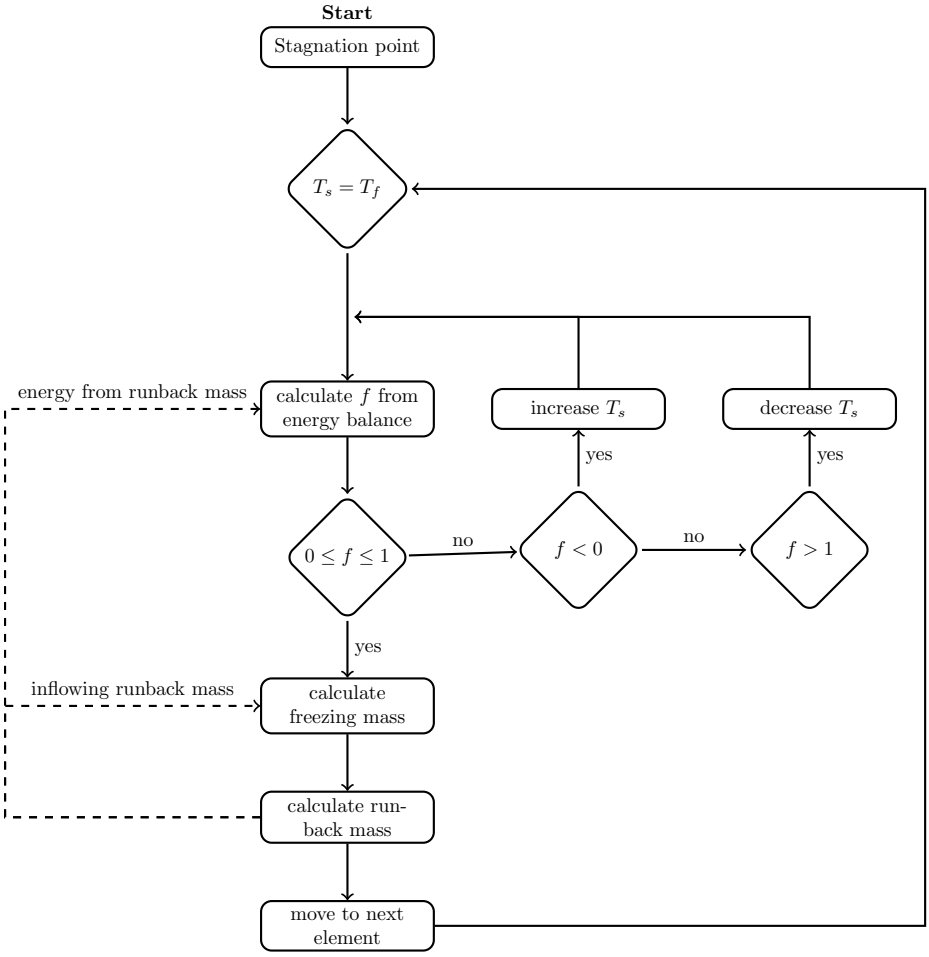

With the freezing fraction known, the freezing mass can be determined, as well as the remaining fraction of water which remains unfrozen and flows into the next downstream element. Now the above procedure is repeated for the adjacent downstream element. First the upper half of aerofoil is solved, until the trailing edge is reached, then this is repeated for the lower half of the aerofoil.

Table 2.1: Overview of the individual mass and energy flux terms in the classic Messinger model.

symbol	formula	description
$\dot{m}_{in}$	$\iint_{\partial V_1} \rho_w \vec{u}_{in} \cdot \hat{n}_1 dS_1$	mass flow of water into the control volume
$\dot{m}_{out}$	$\iint_{\partial V_2} \rho_w \vec{u}_{out} \cdot \hat{n}_2 dS_2$	mass flow of water out of the control volume
$\dot{m}_{imp}$	$\iint_{\partial V_3} \beta\, LWC\, \vec{U}_\infty \cdot \hat{n}_3 dS_3$	droplets being caught by the surface
$\dot{m}_{evap}$	$\iint_{\partial V_3} \bar{\rho} h_m (Y_{vs} - Y_{ve}) \hat{n}_3 dS_3$	the fraction of water that evaporates into the layer of air outside of the control volume
$\dot{m}_{freeze}$	$f(\dot{m}_{in} + \dot{m}_{imp})$	mass flow out of the control volume due to freezing liquid
$\dot{H}_{in}$	$Cp_w(T_{in} - T_s)\dot{m}_{in}$	change in enthalpy due to the temperature difference between the inflowing run back water and the volume
$\dot{H}_{out}$	$Cp_w(T_s - T_{out})\dot{m}_{out}$	change in enthalpy due to the temperature difference between the outflowing run back water and the volume
$\dot{H}_{imp}$	$Cp_w(T_{imp,d} - T_s)\dot{m}_{imp,d}$	change in enthalpy to bring the temperature of impinging droplets to the temperature of the volume
$\dot{H}_{freeze}$	$Cp_w(T_s - T_f)\dot{m}_{freeze}$	change in enthalpy due to freezing water leaving the control volume
$\dot{Q}_{Lh,f}$	$Lh_f \dot{m}_{freeze}$	latent heat of freezing
$\dot{Q}_{Ek,imp}$	$\frac{1}{2} U_\infty^2 \dot{m}_{imp,d}$	kinetic energy of impinging droplets
$\dot{Q}_{conv}$	$\iint_{\partial V_3} h_c (T - T_{rec})\, dS$	energy lost due to convective cooling
$\dot{Q}_{Lh,evap}$	$Lh_{evap} \dot{m}_{evap}$	latent heat of evaporation

2.4 Convective cooling

Heat exchange will take place driven by the temperature difference between the surface and the surrounding air. Starting from the edge of the boundary layer, the fluid is decelerated from its near-free-stream velocity to zero velocity very close to the surface [23]. Along this process, the temperature increases. The temperature very close to the wall, which is called the recovery, or adiabatic wall temperature is used to determine the amount of convective heat exchange.

The recovery temperature is denoted as T_{rec} in the expression for the convective cooling $\dot{Q}_{conv}$ in Table 2.1. It is the increased temperature of a fluid associated to its deceleration nearing a flow obstacle. This is the result of the kinetic energy being converted to internal energy, hence an increase in temperature [15]. When a fluid element is isentropically brought to rest, this recovery temperature can be derived from the stagnation (or total) enthalpy and is defined as the stagnation temperature in Equation 2.18.

$$T_0 = T_\infty + \frac{U_\infty^2}{2C_p} \tag{2.18}$$

In reality fluids usually experience viscous effects and therefore some energy is dissipated into heat and viscous work when the fluid is slowed down. This is an irreversible and thus non-isentropic process. Therefore the increase in temperature during deceleration will be smaller and the final temperature will be lower than the stagnation temperature. To take this irreversibility into account a recovery factor r is defined and given in Equation 2.19 [15].

$$r = \frac{T_{rec} - T_\infty}{T_0 - T_\infty} \tag{2.19}$$

By solving the boundary layer equations an additional, more practical, expression for the recovery factor can be derived. Following the derivation from the book Heat Transfer by Holman [15], the recovery

factor for laminar flow is given in Equation 2.20. For turbulent flow, Holman gives Equation 2.21.

$$\text{laminar:} \qquad r = \mathrm{Pr}^{1/2} \tag{2.20}$$

$$\text{turbulent:} \qquad r = \mathrm{Pr}^{1/3} \tag{2.21}$$

Both Equation 2.20 and Equation 2.21 are valid for Prandtl numbers near unity [15].

When Equation 2.19 is rewritten as an expression for T_0 and plugged in Equation 2.18, an expression for the recovery temperature is found and presented in Equation 2.22

$$T_{rec} = T_\infty + r\frac{U_\infty^2}{2C_p} \tag{2.22}$$

The convective heat transfer coefficient h_c [m/s] in the expression for the convective cooling $\dot{Q}_{conv}$ in Table 2.1 follows from the boundary layer properties. Downstream of the stagnation point of an aerofoil, the heat convection coefficient h_c is determined using the Blasius expression for the turbulent flat-plate boundary layer [22]. The resulting expression is shown below in Equation 2.23

$$h_c(s) = 0.0296\hat{f}\frac{\kappa}{s}\mathrm{Pr}^{1/3}\mathrm{Re}_s^{4/5} \tag{2.23}$$

Here κ is the heat conduction coefficient [W m^{-1} K^{-1}], Pr is the Prandtl number and Re_s the Reynolds number based on the distance s from the stagnation point and the local flow velocity. To account for the irregularities on the surface caused by the ice accretion influencing the flow, a roughness factor is $\hat{f}$ is introduced. Based on experiments it is defined by Jacobs et al. to be equal to 2 [22]. In the stagnation point the heat convection coefficient is defined by Jacobs et al. as given in Equation 2.24.

$$h_{c,stag} = \frac{\kappa}{2}\left(\frac{\rho_a}{\mu_a}\frac{dU_e}{ds}\right)^{1/2} \tag{2.24}$$

Here U_e denotes the flow velocity at the edge of the boundary layer and the subscripts a stands for air.

2.5 Evaporation

The mass flow leaving the control volume due to evaporation is denoted $\dot{m}_{evap}$ in the mass balance introduced in Equation 2.11. It is defined in Equation 2.25 and Table 2.1 as the product of the convective mass transfer coefficient h_m [m/s], and the concentration difference between the vapour at the surface and at the edge of the boundary layer $\rho(Y_{vs} - Y_{ve})$ [18]. This concentration difference is the driving force in the mechanism of evaporation.

$$\dot{m}_{evap} = \iint_{\partial V_3} \bar{\rho} h_m (Y_{vs} - Y_{ve}) \hat{n}_3 dS_3 \tag{2.25}$$

This expression is clarified using the book on Heat Transfer by Çengel [8]. In the chapter on mass transfer the analogy between heat and mass convection is drawn. Mass convection is the transfer of mass between a surface and a moving fluid involving both mass diffusion and bulk fluid motion. The latter enhances the mass transfer by removing the high concentration fluid near the surface. Analogous to Newton's law of cooling in Equation 2.26

$$\dot{Q}_{conv} = h_{conv} A_s (T_s - T_\infty) \tag{2.26}$$

the rate of mass convection is expressed in Equation 2.27 [8].

$$\dot{m}_{mass} = h_{mass} A_s (C_s - C_\infty) \tag{2.27}$$

Here $C_s - C_\infty$ depict the concentration difference and h_m is the convective mass transfer coefficient.

The convective mass transfer coefficient depends, alike its related heat transfer coefficient, on a variety of factors. Examples of these are the surface geometry, the flow velocity and its regime (laminar, turbulent or transitional) but also the composition of the fluid and the variation in fluid properties play an important role [8]. An approximation to the value of h_m can be found by applying the principle of similarity. This principle states that the behaviour of systems that can be described by the same differential equations, subjected to the same boundary conditions will be similar when the coordinate systems are alike. Although in general the differential equations describing heat and mass transport are not that alike, nor are the boundary conditions, the similarity principle can be applied in some specific practical engineering cases [37].

The Chilton-Colburn analogy is one of the better known expressions relating the mechanisms of heat and mass convection. It is given in Equation 2.28 and valid for Prandtl numbers (Pr) ranging between 0.6 and 60 and Schmidt numbers (Sc) between 0.6 and 3000.

$$\frac{f}{2} = \mathrm{St}\mathrm{Pr}^{2/3} = \mathrm{St}_{\mathrm{mass}}\mathrm{Sc}^{2/3} \tag{2.28}$$

In Equation 2.28, St denotes the Stanton number, which is a dimensionless expression for the heat and mass transfer coefficients as defined in Equation 2.29 and Equation 2.30 by making use of Equation 14-77 and Equation 14-78 of Çengel's Heat Transfer: A Practical Approach cited in [8].

$$\mathrm{St} = \frac{h_{conv}}{\rho U_\infty Cp} \tag{2.29}$$

$$\mathrm{St}_{\mathrm{mass}} = \frac{h_{mass}}{U_\infty} \tag{2.30}$$

The dimensionless Prandtl number is a ratio between the magnitudes of momentum diffusion in the velocity boundary layer and heat diffusion in the thermal boundary layer. It can therefore also be seen as the ratio of the thickness between the velocity and thermal boundary layer. The dimensionless Schmidt number is the mass convection variant of the Prandtl number, relating the momentum and mass diffusivity, or the thickness of their respective boundary layers. They are defined in Equation 2.31 and Equation 2.32 by making use of Equation 14-68 and Equation 14-69 of Çengel's Heat Transfer [8].

$$\mathrm{Pr} = \frac{\nu}{\alpha} \tag{2.31}$$

$$\mathrm{Sc} = \frac{\nu}{D_{AB}} \tag{2.32}$$

Filling in for the dimensionless numbers in Equation 2.28 a direct relation between the coefficients of heat and mass convection as is given in Equation 2.33.

$$\frac{h_{conv}}{h_{mass}} = \rho Cp \left(\frac{\mathrm{Sc}}{\mathrm{Pr}}\right)^{2/3} = \rho Cp \left(\frac{\alpha}{D_{AB}}\right)^{2/3} = \rho Cp\, \mathrm{Le}^{2/3} \tag{2.33}$$

The ratio between the mass and thermal diffusivity $\frac{\alpha}{D_{AB}}$ is also known as the dimensionless Lewis number (Le) and is relatively independent of temperature. For mixtures of air and water vapour, the value of $\mathrm{Le}^{2/3} = 0.913$ [8]. In existing icing accretion codes such as the NASA Lewis Ice Accretion Prediction Code (LEWICE) and the Droplerian code as developed in the Engineering Fluid Dynamics group at the University of Twente, indeed the Chilton-Colburn analogy as introduced in Equation 2.28 is applied to determine the convective mass transfer coefficient. For water vapour interfaces the ratio between the convective heat and mass transfer coefficients ranges linearly between 400 and 1200 for air densities between 0.4 and 1.3 kg/m^3. This corresponds to altitudes between 0 and 10 km [5].

The water vapour concentration difference makes up for the second part of Equation 2.25. In the compressible flow around an aerofoil, it will be dependent of the local temperature and pressure. Following the work by Cansdale and Gent [7], a derivation for this concentration difference and the evaporative mass flow will be given.

Starting from the ideal gas law as given in Equation 2.34, the vapour concentration with units [mol/m^3] is given in Equation 2.35. The latter can be multiplied with the molar mass of water to find an expression for the vapour concentration with units [kg/m^3], which is given in Equation 2.36. The term p_v in these equations denotes the vapour (or equilibrium) pressure.

$$pV = nRT \tag{2.34}$$

$$\frac{n}{V} = \frac{p_v}{RT} \tag{2.35}$$

$$\frac{n\,m_w}{V} = \frac{p_v\,m_w}{RT} \tag{2.36}$$

The water vapour concentration difference between the surface and the outer edge of the boundary layer is given in Equation 2.37. The fluid property at the edge of the boundary layer is distinguished using subscript e, for the surface this is subscript s as is shown in Figure 2.9

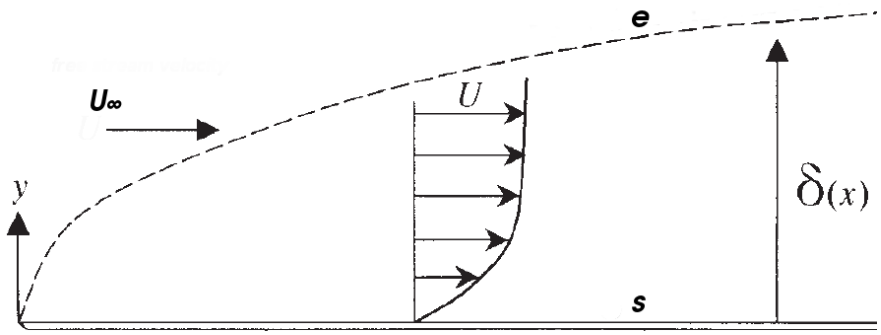

Figure 2.9: Schematic overview of the boundary layer, in which the flow accelerates from zero velocity at the surface (denoted s) to almost free stream velocity (0.99 U_∞) at the edge of the boundary layer (denoted e). The thickness of the boundary layer is denoted by $\delta(x)$ [23].

$$\Delta C = \frac{p_{v,s}\,m_w}{RT} - \frac{p_{v,e}\,m_w}{RT} \tag{2.37}$$

Employing the molar form of the ideal gas law for air, denoted by subscript a in Equation 2.38, the concentration difference in Equation 2.37 can be rewritten into Equation 2.39. The ratio of molar masses m_w/m_a equals 0.622. Here the subscript w denotes water. Applying this results in Equation 2.40

$$\rho_a RT = p\,m_a \tag{2.38}$$

$$\Delta C = \frac{p_{v,s}\rho_{a,s}\,m_w}{P_s\,m_a} - \frac{p_{v,e}\rho_{a,e}\,m_w}{P_e\,m_a} \tag{2.39}$$

$$\Delta C = \frac{0.622 p_{v,s}\rho_{a,s}}{P_s} - \frac{0.622 p_{v,e}\rho_{a,e}}{P_e} \tag{2.40}$$

The pressure in the boundary layer is constant in the direction normal to the surface [23]. Hence, Equation 2.40 can be rewritten into Equation 2.41.

$$\Delta C = \frac{0.622}{p_s}\left(p_{v,s}\,\rho_{a,s} - p_{v,e}\,\rho_{a,e}\right) \tag{2.41}$$

It is assumed that no water condenses in the air travelling from infinity upstream to the edge of the boundary layer. This means that the ratio in densities is constant, as is shown in Equation 2.42. When this is combined with Dalton's law for partial pressures it can be stated that the ratio of partial pressures changes proportional to the change in total pressures [37]. This relation is given in Equation 2.43.

$$\left[\frac{\rho_w}{\rho_a}\right]_e = \left[\frac{\rho_w}{\rho_a}\right]_\infty \tag{2.42}$$

$$\frac{p_{v,e}}{p_{v,\infty}} = \frac{p_e}{p_\infty} \tag{2.43}$$

Applying Equation 2.43, the vapor concentration difference from Equation 2.41 can be rewritten into

$$\Delta C = 0.622 \frac{\rho_{a,e}}{p_s} \left(p_{v,s} \frac{\rho_{a,s}}{\rho_{a,e}} - p_{v,\infty} \frac{p_e}{p_\infty} \right) \tag{2.44}$$

With the ideal gas law as given in Equation 2.45, the ration $\frac{\rho_{a,s}}{\rho_{a,e}}$ from Equation 2.44 can be expressed in terms of temperature since $p_s = p_e$ [23]. This results in Equation 2.46. Assuming isentropic flow conditions inside the boundary layer in the direction normal to the surface, Equation 2.46 is rewritten into Equation 2.47.

$$p = \rho R T \tag{2.45}$$

$$\frac{\rho_{a,s}}{\rho_{a,e}} = \frac{T_e}{T_s} \tag{2.46}$$

$$\frac{T_e}{T_s} = \frac{T_{0,\infty}}{T_s} \frac{T_e}{T_{0,\infty}} = \frac{T_{0,\infty}}{T_s} \left(\frac{p_e}{p_{0,\infty}} \right)^{\frac{\gamma-1}{\gamma}} \tag{2.47}$$

Here $T_{0,\infty}$ denotes the free stream stagnation temperature as defined in Equation 2.18. Combining Equation 2.47 with Equation 2.44 results in the following equation for the concentration difference.

$$\Delta C = 0.622 \, \frac{\rho_{a,e}}{p_s} \left(p_{v,s} \frac{T_{0,\infty}}{T_s} \left(\frac{p_e}{p_{0,\infty}} \right)^{\frac{\gamma-1}{\gamma}} - p_{v,\infty} \frac{p_e}{p_\infty} \right) \tag{2.48}$$

Rewriting Equation 2.48, again using $p_s = p_e$, results in Equation 2.49. This can be simplified to Equation 2.50

$$\Delta C = 0.622 \, \rho_{a,e} \left(\frac{p_{v,s}}{p_s} \frac{T_{0,\infty}}{T_s} \frac{p_e}{p_{0,\infty}} \left(\frac{p_e}{p_{0,\infty}} \right)^{\frac{-1}{\gamma}} - \frac{p_{v,\infty}}{p_\infty} \right) \tag{2.49}$$

$$\Delta C = 0.622 \, \frac{\rho_{a,e}}{p_{0,\infty}} \left(p_{v,s} \frac{T_{0,\infty}}{T_s} \left(\frac{p_e}{p_{0,\infty}} \right)^{\frac{-1}{\gamma}} - p_{v,\infty} \frac{p_{0,\infty}}{p_\infty} \right) \tag{2.50}$$

Combining Equation 2.50 and the mass transfer coefficient h_{mass} from Equation 2.33 into an expression for the evaporative mass flux, alike Equation 2.25 and Equation 2.27, results in Equation 2.51.

$$\dot{m}_{evap} = \frac{0.622 \, h_{conv}}{p_{0,\infty} Cp \, \mathrm{Le}^{2/3}} \left(p_{v,s} \frac{T_{0,\infty}}{T_s} \left(\frac{p_e}{p_{0,\infty}} \right)^{\frac{-1}{\gamma}} - p_{v,\infty} \frac{p_{0,\infty}}{p_\infty} \right) \tag{2.51}$$

The mass flux $\dot{m}_{evap}$ in Equation 2.51 is per surface area, hence the units are [kg/(m^{2}s)]. Although Equation 2.51 might not seem much of an improvement compared to Equation 2.25, all the variables are known, or can relatively be deduced, from the flow solution over the surface. The only troublesome term is the surface temperature T_s, which is one of the outcomes of the solution of the mass and energy balances. This requires the need of an iterative solver to solve the energy balance.

The value of the vapour pressure p_v is an important topic in meteorological research [26]. In the research described in this report, the expression for the vapour pressure of liquid water is adapted from Equation 10 in the work of Murphy and Koop [26]. It is valid for temperature ranging between 123 and 332 Kelvin and is given in Equation 2.52. A plot of the vapour pressure of liquid water as a function of temperature is shown in Figure 2.10.

$$\begin{aligned} \ln(p_{v,liq}) \approx{}& 54.842763 - \frac{6763.33}{T} - 4.210 \ln(T) + 0.000367 \, T \\ &+ \tanh\left[0.0415(T - 218.8)\right] \left(53.878 - \frac{1331.22}{T} - 9.44523 \ln(T) + 0.014025 \, T \right), \\ &\text{for} \qquad 123 < T < 332 \, \mathrm{K} \end{aligned} \tag{2.52}$$

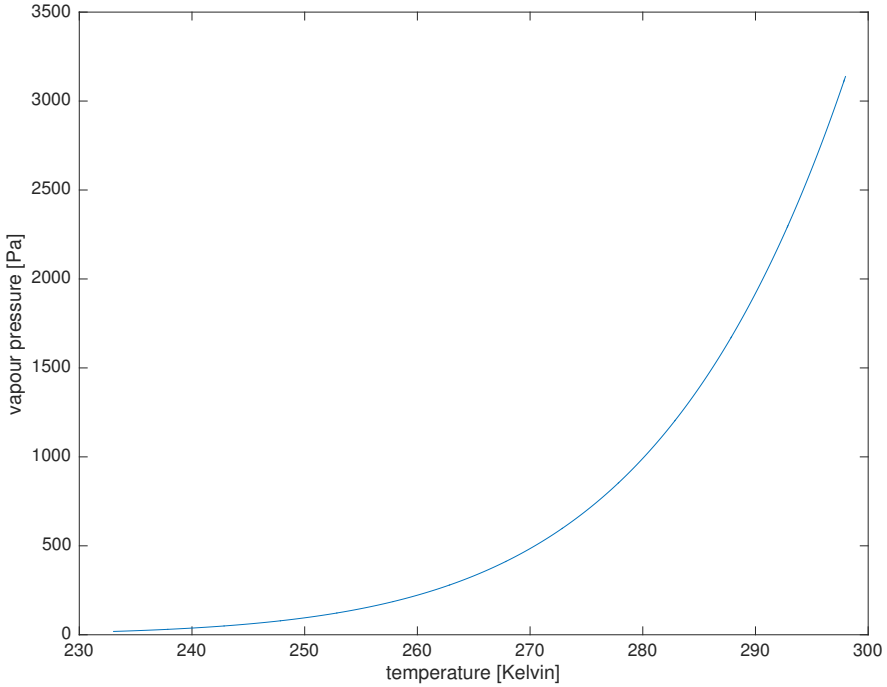

Figure 2.10: Vapour pressure water plotted versus temperature.

In LEWICE and Droplerian, an expression similar to Equation 2.51 is used. This expression is given below in Equation 2.53, which is adapted from Equation A-13 in the LEWICE users manual cited in [34].

$$\dot{m}_{evap} = \frac{h_{conv}}{Cp\,\mathrm{Le}^{2/3}} \left(\frac{\mathrm{Pr}}{\mathrm{Sc}}\right)^{2/3} \left[\left(\frac{p_{v,s}}{T_s} - r\frac{p_e}{T_e}\frac{p_{v,0,\infty}}{p_{0,\infty}}\right) \Big/ \left(\frac{1}{0.622}\frac{p_e}{T_e} - \frac{p_{v,s}}{T_s}\right)\right] \tag{2.53}$$

Unfortunately, it proved to be rather difficult to reproduce this expression, and a derivation was not found in the literature. Therefore it is decided to express the evaporating mass in the remainder of this research as stated in Equation 2.51, which was derived by Cansdale and Gent [7]. In Figure 2.11 graphs are shown of both expressions using input and results from test case 7 presented in Section 3. The total amount of mass lost due to evaporation is less than 1 percent of the total amount of mass impinging the surface. Although both curves in Figure 2.11 have the same shape, the difference between them is a value of 1.2×10^{-7} [kg/s]. The negative values indicates that vapour is actually condensing on the surface. Positive values for mass evaporation have been encountered in other test cases. In Figure 2.11 the stagnation point of the aerofoil lies at element number 107. Elements to the right of element number 107 correspond to the top side of the aerofoil, elements to the left to the bottom of the aerofoil.

2.6 Mixed phase conditions

The High Altitude Ice Crystals (HAIC) project was set up to enhance aircraft safety when flying in mixed phase icing conditions. Part of this HAIC project is dedicated to the development and improvement of numerical models to predict ice growth. This includes the adjustment of the original Messinger model to mixed phase icing conditions. Due to the coexistence of liquid and ice particles in the mixed phase flow entering an aircraft engine and the presence of (initially) heated surfaces in the aircraft engine, the original Messinger model is not sufficient to model the accretion of ice on the surface. Contributors to this research include the Italian Aerospace Research Centre (CIRA), the French Aerospace Lab (ONERA) and Spain's National Institute of Aerospace Technology (INTA). The improvements proposed by the researchers from these institutes will be be introduced in this section. The source for this section is HAIC deliverable number 652 [19].

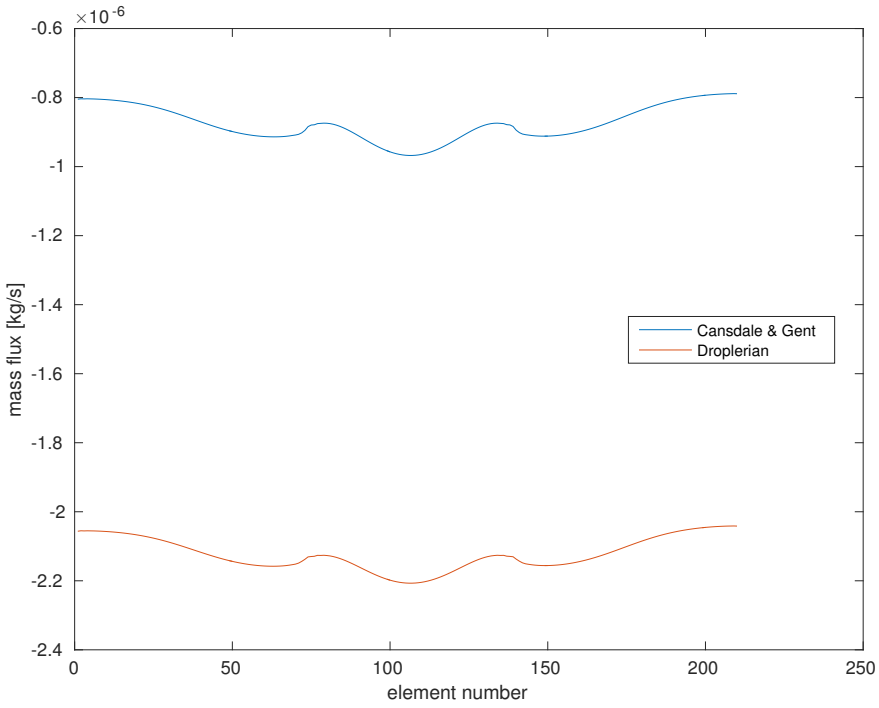

Figure 2.11: Comparison between evaporative rates used in Droplerian with the expression derived by Cansdale and Gent.

2.6.1 CIRA

Due to the mixed phase conditions, three different icing scenarios are recognised, namely:

- Rime condition, with all the incoming water being turned to ice. This is characterized by a surface temperature lower than the freezing temperature of water $T_s < T_f$;
- Glaze condition, when both water and ice are present at the surface. This is characterized by a surface temperature equal to the freezing temperature $T_s = T_f$;
- Film condition, when there is only water present at the surface. This is characterized by a surface temperature higher than the freezing temperature $T_s > T_f$.

In the classic Messinger model, only glaze and rime conditions are clearly distinguished from each other. In glaciated- and mixed-phase icing conditions in general the water film is of greater importance. The surface upon which the droplets and ice crystals impact is of influence on the behaviour of the ice particles. When the surface is wet, in glaze ice or film conditions, ice crystals may bounce, stick or shatter into smaller pieces depending on impact velocity, diameter and liquid film height. When the surface is dry, in rime ice or no film conditions, the crystals will bounce or shatter upon impact with the surface and do not stick to it.

Mass balance

In the CIRA approach, mass balances are created separately for the water and ice phase, which can both be present in the same control volume. The differences with the original Messinger model are the terms accounting for mass flow of impinging ice crystals, denoted by $\dot{m}_{imp,ic}$. Depending on external conditions, the ice crystals can be (partly) melted $\dot{m}_{imp,ic,m}$ or remain in a frozen state $\dot{m}_{imp,ic,f}$.

The increase in mass due to impinging ice crystals $\dot{m}_{imp,ic}$ is defined in Equation 2.54.

$$\dot{m}_{imp,ic} = \iint_{\partial V_3} \eta_{st} \beta_{ic} \, IWC \, \vec{U}_\infty \cdot \hat{n}_3 dS_3 \tag{2.54}$$

In Equation 2.54 a new term is present, η_{st} which denotes the sticking rate. This rate is defined in Equation 2.55 as the fraction of impinging ice crystals that stick to the surface from the total amount of crystals that imping at the surface. The remaining part of the crystals that do not stick to the surface will bounce off from it and possibly scatter during this process.

$$\eta_{st} = \frac{\dot{m}_{st,ic}}{\dot{m}_{imp,ic}} \tag{2.55}$$

This sticking rate is dependent of the height of the water film. Hence some sort of feedback loop is used in the model from CIRA to relate the sticking rate η_{st} to the film height h_f of the water layer. Details on this relation are not specified in Deliverable 652 [19].

The term β_{ic} in Equation 2.54 represents the catching efficiency for the ice crystals. Due to the mixed phase conditions there are two types of impinging particles: water droplets and ice crystals. The result of this is that there will also be two catching efficiencies β. For the water droplets the catching efficiency is defined as β_d and for the ice crystals this is β_{ic}.

To account for the fraction of impinging ice crystals that melt on the surface in glaze ice and water film conditions, the melting rate η_{melt} is introduced. It is defined in Equation 2.56 as the fraction of the crystals that stick and melt at the surface from the total amount of crystals that stick at the surface.

$$\eta_{melt} = \frac{\dot{m}_{imp,icm}}{\dot{m}_{st,ic}} \tag{2.56}$$

Due to the newly introduced rates of sticking and melting, the mass flow of impinging melted ice crystals is defined as $\dot{m}_{imp,ic,m}$ in Equation 2.57.

$$\dot{m}_{imp,ic,m} = \iint_{\partial V_3} \eta_{melt}\eta_{st}\beta_{ic}\, IWC\, \vec{U}_\infty \cdot \hat{n}_3 dS_3 \tag{2.57}$$

The total amount of impinging ice crystals can be split up $\dot{m}_{imp,ic} = \dot{m}_{imp,ic,m} + \dot{m}_{imp,ic,f}$. The fraction of ice crystals which do not melt is defined as $\dot{m}_{imp,ic,f}$ in Equation 2.58.

$$\dot{m}_{imp,ic,f} = \iint_{\partial V_3} (1-\eta_{melt})\eta_{st}\beta_{ic}\, IWC\, \vec{U}_\infty \cdot \hat{n}_3 dS_3 \tag{2.58}$$

Rime ice conditions are characterized by the absence of water on the surface. Hence, no run back water or evaporation can occur. The mass balances for water and ice are therefore defined by CIRA as in Equation 2.59 and Equation 2.60.

$$\dot{m}_{imp,d} + \dot{m}_{in} = \dot{m}_{freeze} \tag{2.59}$$

$$\dot{m}_{freeze} + \dot{m}_{imp,ic} - \dot{m}_{sub} = \dot{m}_{ice} \tag{2.60}$$

The term $\dot{m}_{sub}$ represents the mass lost due to sublimation.

Glaze ice conditions imply that both water and ice are present in the control volume. Here the melting rate η_{melt} is of importance, denoting the amount of melted ice crystals entering the water phase. The mass balances for the glaze ice conditions are defined in Equation 2.61 and Equation 2.62.

$$\dot{m}_{imp,d} + \dot{m}_{imp,ic,m} + \dot{m}_{in} = \dot{m}_{freeze} + \dot{m}_{evap} + \dot{m}_{out} \tag{2.61}$$

$$\dot{m}_{freeze} + \dot{m}_{imp,ic,f} - \dot{m}_{sub} = \dot{m}_{ice} \tag{2.62}$$

Water film conditions are characterized by the absence of any ice. Therefore only a mass balance for the water fraction can be given below in Equation 2.63.

$$\dot{m}_{imp,d} + \dot{m}_{imp,ic} + \dot{m}_{in} = \dot{m}_{evap} + \dot{m}_{out} \tag{2.63}$$

Energy balance

The energy balance for the control volume is defined as the sum of the change in total enthalpy for the water and ice phase $\Delta\dot{H}_w$ and $\Delta\dot{H}_i$ respectively and the heat source and sink terms $\dot{Q}_{in}$ and $\dot{Q}_{out}$. Therefore the overall heat balance for each scenario is given by

$$\Delta\dot{H}_w + \Delta\dot{H}_i = \dot{Q}_{in} - \dot{Q}_{out} \tag{2.64}$$

Filling in for Equation 2.64 all associated terms results in Equation 2.65.

$$\begin{aligned}\dot{H}_{imp,d} + \dot{H}_{in} + \dot{H}_{out} + \dot{H}_{imp,ic} + \dot{H}_{freeze} + \dot{H}_{evap} = \\ \dot{Q}_{Lh,f} + \dot{Q}_{Ek,imp,d} + \dot{Q}_{Ek,imp,ic} + \dot{Q}_{conv} - \dot{Q}_{Lh,sub} - \dot{Q}_{Lh,evap} - \dot{Q}_{Lh,melt}\end{aligned} \tag{2.65}$$

The subscript Lh denotes the latent heat associated to a phase change. For instance $\dot{Q}_{Lh,melt}$ denotes the latent heat absorbed by the melting fraction of impacting ice crystals. In Table 2.2 all the enthalpy and energy terms are listed. Depending on which icing scenario (rime, glaze or water film) is assumed, some of the terms will be present whilst others will be equal to zero and drop out of Equation 2.65.

Solution procedure

The solution procedure for the CIRA model is iterative and consists of first assuming an icing scenario which gives a requirement for the temperature. This will also limit the number of terms in the mass and energy balances. For instance when rime ice conditions are assumed, no water is present, since all the incoming water will freeze instantaneously. The result is that the terms related to evaporation and run back water can be omitted from the equations. A flow chart of the solution procedure in the CIRA model is included in Figure 2.12.

In glaze ice conditions an extra unknown has to be determined in the form of the melting factor η_{melt}, required to determine the fraction of impinging ice crystals that melt into the water layer upon contact. The impinging ice crystals that melt lower the total energy of the system which has to be accounted for by additional freezing of liquid water. To determine if this is necessary and to calculate η_{melt}, the energy equation is slightly altered to read

$$\Delta Q^* = Q_{in} - Q_{out} - \Delta H_w - \Delta H_i - \dot{Q}_{Lh,f} + \dot{Q}_{Lh,melt} \tag{2.66}$$

or when filled in

$$\Delta Q^* = \dot{Q}_{Ek,imp,d} + \dot{Q}_{Ek,imp,ic} + \dot{Q}_{conv} - \dot{Q}_{Lh,sub} - \dot{Q}_{Lh,evap} - \dot{H}_{imp,d} - \dot{H}_{in} - \dot{H}_{imp,ic} \tag{2.67}$$

In Equation 2.66 and 2.67, the ΔQ^* term is the amount of latent heat required at $T_s = T_f$ for a physical phase change. The different possible values for ΔQ^* are:

- $\Delta Q^* > 0$, meaning that some energy is still present within the volume, which can be used to melt a part of the incoming ice crystals to restore the energy balance;
- $\Delta Q^* < 0$, meaning that the volume is short of energy. The energy balance is restored by freezing additional water and releasing the latent heat of freezing;
- $\Delta Q^* = 0$, meaning that the energy balance is already satisfied without taking the additional terms for the latent heat of freezing and melting from Equation 2.66 into account. So the mass of melted ice crystals is counterbalanced by the system by freezing additional water mass.

2.6.2 INTA

Similar to the CIRA approach, the INTA approach also consists of determining all terms that contribute to the energy and mass equation and than solve it for certain scenarios or regimes. Different from the CIRA approach, the INTA approach does not consider partly melted ice crystals impinging on the surface: the impinging mass is only due to supercooled droplets $\dot{m}_{imp,d}$ and solid ice crystals

Figure 2.12: Flowchart of the solution procedure in the CIRA approach.

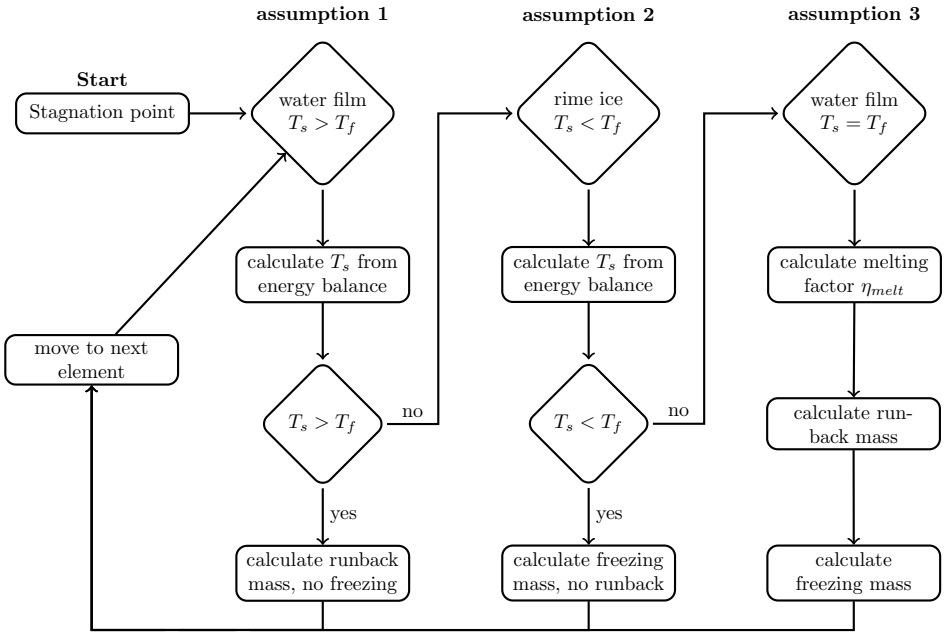

$\dot{m}_{imp,ic}$. The melting action which occurred along its trajectory in the CIRA approach, is accounted for after impact on the surface in the INTA approach. Also INTA does not include the influence of the water film thickness on the sticking rate, meaning that there is no iterative loop between the impingement model and the ice accretion model. INTA uses only one control volume for the water layer. Therefore all particles enter the water layer, after which the energy balance determines how much mass moves into the ice layer.

Mass balance

The mass balance in the INTA approach is given in Equation 2.68 and 2.69.

$$\dot{m}_{imp,d} + \dot{m}_{imp,ic} + \dot{m}_{in} = \dot{m}_{freeze} + \dot{m}_{evap} + \dot{m}_{out} \tag{2.68}$$

$$\dot{m}_{sol} = \dot{m}_{freeze} + (1 - \eta_{melt})\dot{m}_{imp,ic} \tag{2.69}$$

The difference with the mass balance used in the CIRA approach is that in the INTA approach the impinging ice crystals that remain frozen after impact not move directly into the ice layer upon impact. This is accounted for by an additional freezing term in the energy balance. This extra term is $\dot{m}_{imp,ic,u} Cp_i (T_s - T_{imp,ic})$ and corresponds to the enthalpy lost from ice crystals leaving the water volume. The subscript ic, u denotes the fraction of ice crystals that remains frozen (un-melted).

Energy balance

The energy balance in the INTA approach is given in Equation 2.70.

$$\begin{aligned} \dot{H}_{imp,d} + \dot{H}_{in} + \dot{H}_{out} + \dot{H}_{imp,ic} + \dot{H}_{freeze} + \dot{H}_{evap} = \\ \dot{Q}_{Lh,f} + \dot{Q}_{Ek,imp,d} + \dot{Q}_{Ek,imp,ic} + \dot{Q}_{conv} - \dot{Q}_{Lh,sub} \\ -\dot{Q}_{Lh,evap} - \dot{Q}_{Lh,melt} - \dot{m}_{imp,ic,u} Cp_i (T_s - T_{imp,ic}) \end{aligned} \tag{2.70}$$

Solution procedure

The solution procedure consists of first assuming $T_s = T_f$, $\eta_{melt} = 0$ and using these assumptions to solve m_{freeze} from Equation 2.68 to 2.70. Note that these assumptions simplify the mass and

energy balance equations. Depending on the outcome of this, one of the three predefined scenarios is considered valid. These three scenarios are comparable to the rime ice, glaze ice and water film conditions defined in the CIRA approach. The flowchart for this procedure is given in Figure 2.13.

2.6.3 ONERA

The ONERA approach is in essence not much different from the previously introduced CIRA and INTA approaches. Since there are not much specifics regarding the ONERA solution procedure present in the literature used it is decided to omit a in depth analysis of the solution procedure [19].
The feedback loop between the calculation of the water film thickness and the fraction of ice crystals that stick to the surface is however worth mentioning. A formula is introduced which relates the water film thickness h_f to the runback flow of water leaving the control volume. It is given in Equation 2.71.

$$\dot{m}_{out}\Delta s = -\frac{h_f^2}{3\mu_w}\frac{\partial p_a}{\partial s} + \frac{h_f^2}{2\mu_w}\tau_a \tag{2.71}$$

Here τ_a denotes the shear stress exerted by the air at the surface and Δs is the size of the control volume. Note that it is implied that the water film is continuous, i.e. not fragmented. This means that h_f should be interpreted as the average film thickness in the control volume.

The CIRA approach uses a similar relation, whose derivation is repeated below. The velocity in the film is taken from boundary layer theory and is given in Equation 2.72.

$$u(x) = \frac{y}{\mu_w}\tau_{wall} \tag{2.72}$$

This expression in Equation 2.72 can be used to express the average flow velocity $\bar{u}$ in Equation 2.73.

$$\bar{u}(x) = \frac{1}{h_f}\int_0^{h_f} u(x,y)\,dy = \frac{1}{h_f}\int_0^{h_f} \frac{y}{\mu_w}\tau_{wall}\,dy = \frac{h_f}{2\mu_w}\tau_{wall} \tag{2.73}$$

The total amount of water present in the control volume, hence the film thickness, is dependent on the mass source and sink terms such as impingement, freezing and evaporation, as well as the flow velocity of the water. This is expressed in Equation 2.74.

$$\oint \rho\bar{u}h_f(x)\,dS = \dot{m}_{tot}\Delta v \tag{2.74}$$

Here the contour integral is taken over the boundaries of the control volume. The sum of mass sources and sinks is denoted $\dot{m}_{tot}$ and Δv represents the element volume. Filling in for $\bar{u}$ gives Equation 2.75.

$$\oint \frac{h_f}{2\mu_w}\tau_{wall}h_f(x)\,dS = \left[\frac{h_f^2}{2\mu_w}\tau_{wall}\Delta S\right]_{i-1}^{i} = \left[\dot{m}_{tot}\Delta v\right]_i \tag{2.75}$$

In Equation 2.75 the indices i and $i-1$ indicate the current and the previous control volume. Rewriting for h_f gives Equation 2.76.

$$h_f^2\big|_i = \left[\frac{2\mu_w}{\tau_{wall}\Delta s}\right]_i \left(\left[\frac{\tau_{wall}}{2\mu_2}h_f^2\Delta s\right]_{i-1} + \left[\dot{m}_{tot}\Delta v\right]_i\right) \tag{2.76}$$

Similar to the ONERA approach, Equation 2.76 is used to determine the water film thickness. This film thickness depends, among other terms, on mass flow of impinging ice crystals. The number of impinging ice crystals that stick to the surface depends on the water film thickness. Hence an iterative process is applied to close and solve this system.

Figure 2.13: Flowchart of the solution procedure in the INTA approach.

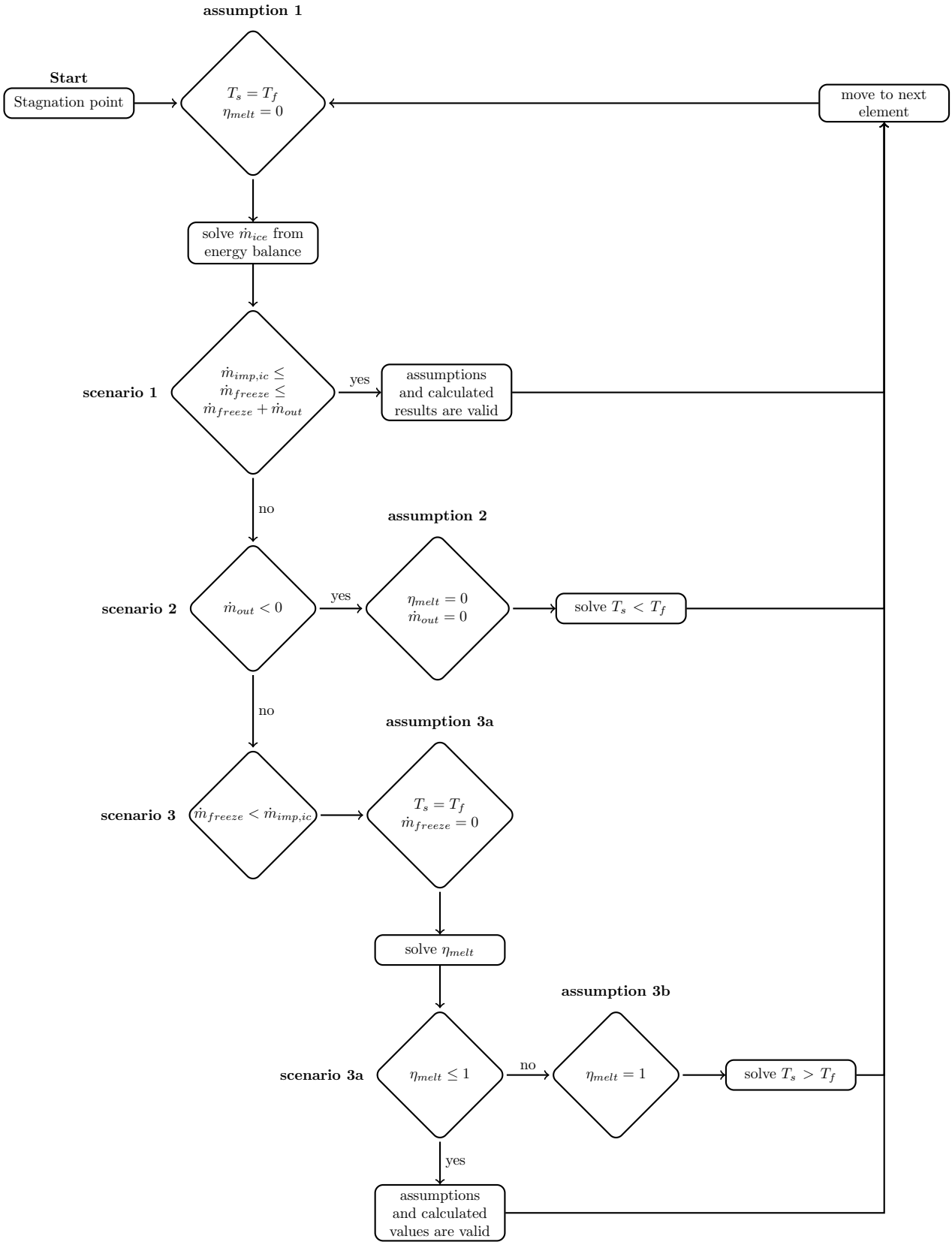

Table 2.2: Overview of the individual mass and energy flux terms in the mixed-phase models.

symbol	formula	description
$\dot{m}_{in}$	$\iint_{\partial V_1} \rho_w \vec{u}_{in} \cdot \hat{n}_1 dS_1$	mass flow of water into the control volume
$\dot{m}_{out}$	$\iint_{\partial V_2} \rho_w \vec{u}_{out} \cdot \hat{n}_2 dS_2$	mass flow of water out of the control volume
$\dot{m}_{imp,d}$	$\iint_{\partial V_3} \beta_d \, LWC \, \vec{U}_\infty \cdot \hat{n}_3 dS_3$	droplets being caught by the surface
$\dot{m}_{imp,ic}$	$\iint_{\partial V_3} \beta_{ic} \, IWC \, \vec{U}_\infty \cdot \hat{n}_3 dS_3$	ice crystals being caught by the surface
$\dot{m}_{evap}$	$\iint_{\partial V_3} \bar{\rho} h_m (Y_{vs} - Y_{ve}) \hat{n}_3 dS_3$	the fraction of water that evaporates into the layer of air outside of the control volume
$\dot{m}_{freese}$	$f(\dot{m}_{in} + \dot{m}_{imp})$	mass flow out of the control volume due to freezing liquid
$\dot{H}_{in}$	$Cp_w(T_{in} - T_s)\dot{m}_{in}$	change in enthalpy due to the temperature difference between the inflowing run back water and the volume
$\dot{H}_{out}$	$Cp_w(T_s - T_{out})\dot{m}_{out}$	change in enthalpy due to the temperature difference between the outflowing run back water and the volume
$\dot{H}_{imp,d}$	$Cp_w(T_{imp,d} - T_s)\dot{m}_{imp,d}$	change in enthalpy to bring the temperature of impinging droplets to the temperature of the volume
$\dot{H}_{imp,ic}$	$Cp_i(T_{imp,ic} - T_s)\dot{m}_{imp,ic}$	change in enthalpy to bring the temperature of impinging droplets to the temperature of the volume
$\dot{H}_{freeze}$	$Cp_w(T_s - T_f)\dot{m}_{freeze}$	change in enthalpy due to freezing water leaving the control volume
$\dot{Q}_{Lh,f}$	$Lh_f \dot{m}_{freeze}$	latent heat of freezing
$\dot{Q}_{Ek,imp,d}$	$\frac{1}{2} U_\infty^2 \dot{m}_{imp,d}$	kinetic energy of impinging droplets
$\dot{Q}_{Ek,imp,ic}$	$\frac{1}{2} U_\infty^2 \dot{m}_{imp,ic}$	kinetic energy of impinging ice crystals
$\dot{Q}_{conv}$	$\iint_{\partial V_3} h_c (T - T_{rec}) \, dS$	energy lost due to convective cooling
$\dot{Q}_{Lh,sub}$	$Lh_{evap} \dot{m}_{evap}$	latent heat of sublimation
$\dot{Q}_{Lh,evap}$	$Lh_{evap} \dot{m}_{evap}$	latent heat of evaporation
$\dot{Q}_{Lh,melt}$	$Lh_{evap} \dot{m}_{evap}$	latent heat of melting ice crystals
ΔQ^*	free energy in control volume	amount of latent heat required at $Ts = Tf$ for a physical phase change

2.7 Erosion

In 2003 a series of tests were performed by Al-Khalil et al. [3] to study the effects of mixed-phase (ice crystals and supercooled liquid droplets) and glaciated (ice crystals only) icing conditions on the performance of thermal anti-icing equipment. One of the observation pointed out in the report is that when glaze ice is being formed in mixed-phase conditions, the presence of ice particles in the flow reduced the overall ice shape on the surface. It is believed that this is caused by a combination of splashing and erosion. Splashing is caused by crystals impacting, splashing and thus reducing the water layer present on the surface. Erosion is the reduction of the amount of ice accreted on the by the impacting ice crystals. The momentum of these impacting ice crystals will then dislodge portions of ice. Also the observed ice shapes in general appeared to have a more smooth surface due to a 'sand blasting' effect caused by the ice crystals were present in the flow.

Shown in Figure 2.14 are some of the result as obtained by Al-Khalil et al. [3]. Note the difference in ice shape in the case of rime ice accretion, which is largely caused by the lower amount of liquid water content (LWC). It is believed by Al-Khalil et al. that the rime ice shape is merely a result

of the supercooled liquid droplets in the mixed-phase flow. The larger ice water content (IWC) in Run 19 is however held responsible for the smoother ice surface. The differences in surface roughness between Run 19 and 20 can be clearly seen in Figure 2.14c. The influence of the ice crystals is much more visible in the case of glaze ice formation. Between run 9 and 10, the total water content (TWC = LWC + IWC) is doubled, by adding an equal amount of IWC to the LWC. The ice shape however is greatly reduced, illustrating the effect of the erosive action by the ice crystals. Thereby the surface roughness in the form of ice horns and feathers is greatly reduced, as the result of the sandblasting effect of the impacting ice crystals. This is also clearly visible in Figure 2.14d.

The mechanical properties of ice, such as its tensile strength, ductility and plasticity, are important in understanding the behaviour of ice. This knowledge can be applied to for instance the field of glaciology, but also in engineering, when looking at the interaction of ice structures with offshore structures and marine vessels. Compared to other materials, ice is relatively brittle at temperatures near its melting point. Failure tests were performed by Rist and Murrell [33] to gain additional insight in the deformation and strength behaviour of ice at different temperatures. It is expected that the ductile behaviour of ice is according to the power law equation of creep stated in Equation 2.77 [33].

$$\dot{\epsilon} = A(\sigma_1 - \sigma_3)^n \exp\left(-\frac{Q}{RT}\right) \tag{2.77}$$

In this expression $\dot{\epsilon}$ is the strain rate. Strain is a measure for the deformation of a body, for instance the elongation of a rod relative to its own length. The strain rate $\dot{\epsilon}$ is the time rate of change of strain, or the derivative of strain with respect to time. The term $\sigma_1 - \sigma_3$ represents the differential stress, defined as the difference between the greatest and least compressive stress applied to a body. The parameters A and n are material constants and Q is the activation energy for the creep mechanism to occur. The temperature and the molar gas constant are denoted by T and R respectively. Linear regression analysis performed by Rist and Murrell of their measurement data resulted in the following constants:

$$\begin{aligned} Q &= 69\,\text{kJ / mol;} \\ n &= 4.2\ \pm 0.2; \\ \log A &= 14 \pm 3; \\ R &= 8.3144598\,\text{J / (mol K).} \end{aligned}$$

To create an accurate erosion prediction model, it would be desirable to have a wide range of experimental test results relating the test parameters to the amount of eroded ice.

Inspired by the lack a wide experimental data set, Wright et al. [43] introduced a method to estimate the effect of erosion. Their approach is to define a reference case: a certain mixed-phase icing case for which erosion does not occur, but is on the edge of being of influence. Other icing conditions are compared to this reference case and based on the difference the effect of erosion is estimated. For the reference case they use Run 19 from the work by Al-Khalil et al. [3]. The results from this run are shown in Figure 2.14 and indeed the effect of erosion appears to be minor. The choice of using Run 19 might however be questioned, since Al-Khalil et al. clearly stated that the effect of erosion is, however only minor, visible as the sandblasting effect of the surface [3].

The differential stress $\sigma_3 - \sigma_1$ from Equation 2.77 is defined by Wright et al. as proportional to the force of impact, which is the product of the momentum of impinging icing particles and the frequency of impingement. The resulting expression for the force of impact is given in Equation 2.78 [43].

$$F_{impact} = \left[\frac{\pi}{6}\rho_i d^3\right] U_{imp} \left[\frac{U_{imp}}{d}\left(\frac{IWC}{\rho_i}\right)^{1/3}\right] \tag{2.78}$$

In this equation, the first term between the brackets denotes the mass of a single ice crystal, assuming spherical particles. The term between the second pair of square brackets is the particle frequency of impingement. Although a dimensional analysis checks out, it is not clear upon what theory Equation 2.78 is based.

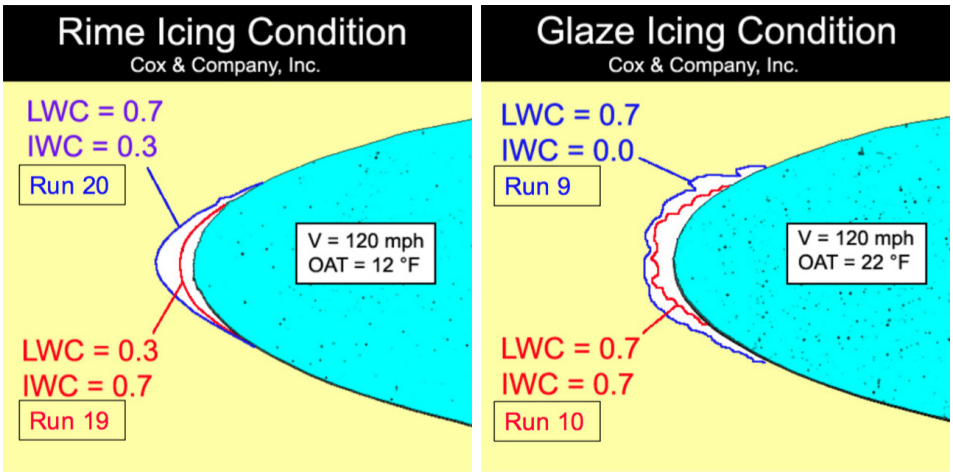

(a) Graph of rime ice thickess.

(b) Graph of glaze ice thickess.

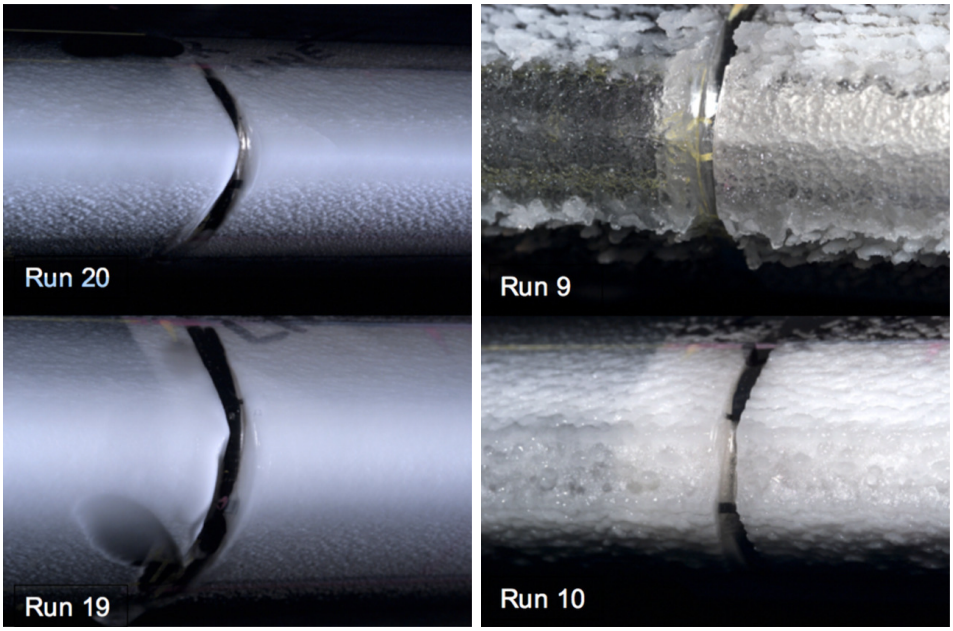

(c) Rime ice.

(d) Glaze ice.

Figure 2.14: Results from the ice accretion tests in the Cox icing wind tunnel. Note in the rime ice formation (left) the effects of erosion due to increased IWC. In the glaze ice formation (right), note the difference in roughness with the rime ice and the reduced ice shape due to splashing and erosion. The LWC and IWC denote the liquid- and ice water content of the flow [g m^{-3}] [3].

When Equation 2.78 is pluggend into Equation 2.77 a ratio of strain rate can be estimated by Equation 2.79 [43].

$$\frac{\dot{\epsilon}}{\dot{\epsilon}_t} \approx \left(\frac{d}{d_t}\right)^2 \left(\frac{U_{imp}}{U_{imp,t}}\right)^2 \left(\frac{IWC}{IWC_t}\right)^{1/3} \left(\frac{\exp\left(14 - \frac{Q}{RT}\right)}{\exp\left(14 - \frac{Q}{RT_t}\right)}\right) \tag{2.79}$$

The threshold values chosen by Wright et al. based on Run 19 from the work of Al-Khalil et al. and

are denoted by subscript t in Equation 2.79. These values are [43]

$$\begin{aligned} d_t &= 150\,\mu\text{m}; \\ V_t &= 100\,\text{kts} \approx 51\,\text{m/s}; \\ IWC_t &= 0.7\,\text{g/m}^3; \\ T_t &= 267\,\text{Kelvin}. \end{aligned}$$

Again the data specified by Wright et al. deviates from the values stated in the report from Al-Khalil et al.. The differenece in velocity is 4 kts, or 2 m/s, which could be explained by rounding. The temperature of 267 Kelvin mentioned by Wright et al. does not correspond to the temperature of Run 19 as stated by Al-Khalil et al., who specifies a temperature of 262 Kelvin.

When it is assumed that the amount of erosion is related to the strain rate, it is possible to relate the increase in erosion to the strain rate ratio from Equation 2.79. This is done by Wright et al. by comparing Run 19 (the threshold) to Run 10 from the report of Al-Khalil et al., see Figure 2.14. Plugging in the parameters from Run 10 in Equation 2.79 gives Equation 2.80 [43].

$$\frac{\dot{\epsilon}}{\dot{\epsilon}_t} \approx \left(\frac{200}{100}\right)^2 \left(\frac{100}{100}\right)^2 \left(\frac{0.7}{0.7}\right)^{1/3} \left(\frac{\exp\left(14 - \dfrac{69 \times 10^3}{8.314 \cdot 273}\right)}{\exp\left(14 - \dfrac{69 \times 10^3}{8.314 \cdot 267}\right)}\right) = 3.5 \tag{2.80}$$

The difference in ice mass between Run 9 (IWC = 0) and Run 10 (IWC = 0.7) due to erosion is according to Wright et al. 20 percent. Appart from the difference in IWC, Run 9 and Run 10 are identical, see also Figure 2.14. Based on this 20 percent reduction, Wright et al. suggests the empirical equation for erosion as stated in Equation 2.81.

$$\text{erosion} = 0.08\left(\frac{\dot{\epsilon}}{\dot{\epsilon}_t} - 1\right) \tag{2.81}$$

When plugging in the result from Equation 2.80, indeed a value of 0.2 is found for the erosion term. This is incorporated in the impingement model by multiplying the catching efficiency for ice crystals β_{ice} with $(1 - \text{erosion})$ and thus effectively reducing the amount of impinging droplets.

Although some inaccuracies are present in the work of Wright et al., the main idea remains very useful. Especially in the absence of quantitative data regarding the parameters of influence on erosion, the method introduced seems a good method to estimate and investigate the influence of erosion.

2.8 Impingement

When an ice crystals impacts a surface there are three possible scenarios that can occur:

1. the crystal sticks to the surface, usually under influence of water being present on the surface or in the form of (partly) melted ice crystals;
2. the crystal bounces off the surface, the velocity of the particle is changed however its size and shape are unaltered;
3. the crystal shatters into multiple smaller fragments, some of them remain on the surface, others are bouncing from the surface back into the flow field.

Depending on the characteristics of the crystal, its impact and the surface upon which it impacts, one of the three scenarios will occur. Due to a lack of experimental data it is very difficult to predict accurately which scenario occurs [40].

The importance of a water film present on the surface was recognised by Nilamdeen and Habashi [28]. They introduced a model that assumes a sticking coefficient which is linearly proportional to the water layer thickness and inversely proportional to the normal impact velocity. The sticking coefficient also

depends on the size of the ice crystal. Compared to larger ice crystals, a smaller ice crystal is for the same sticking fraction allowed to impact with a larger velocity normal to the surface. Also a threshold velocity is defined, such that particles exceeding this velocity will always bounce from the surface. A limitation is that this model does not take into account that ice crystals may break up into pieces upon impact, re-enter the flow field and impact on the surface further downstream [28]. Thereby model parameters such as the threshold velocity should be calibrated using experimental data. This will cause inaccuracies and possibly limits the general applicability of the model.

A model for the sticking efficiency which did not directly depend on the water film thickness was introduced by Currie et al. [11]. Calibrated using experiments they defined a sticking rate dependent of impact velocity and angle of impact, as well as a number of material properties. Their impingement model also incorporated erosive action on the surface. The material properties include erosion related mechanical properties and an experimentally determined factor that depends on the TWC of the flow [11]. The thickness of the water layer will vary with the TWC, since more water in the air will probably result in more water on the surface. When using the water film height to determine the sticking fraction, a feedback loop is required in the model to relate both parameters. Using the TWC instead of the water film thickness would circumvent the need of such a loop.

As a part of the HAIC project, preliminary laboratory experiments were performed by Hauk et al. in [13] to provide data to calibrate and validate the models introduced by Villedieu et al. [40] and Iuliano et al. [20]. The latter applied a sticking model based on the work of Currie et al. [11]. They adjusted and calibrated the model by Currie et al. to fit the results from the experiments performed by Hauk et al. [13]. Additionally they added a mechanism predicting ice crystal shattering comparable to Villedieu et al. [40]. This mechanism will be introduced later in this section.

The catching efficiency found by Iuliano et al. is shown in Figure 2.15 adapted from [20]. Whereas Currie et al. [11] used a spherical test object, Iuliano et al. [20] use a wedge shaped object. In Figure 2.15 the results are shown when no impact model is applied and when an impact model based on data from by Hauk et al. [13] is applied. The blue line shows results according to Currie et al. [11]. The wedge is positioned in the flow with a angle of attack unequal to zero. The dimensionless parameter S/c in Figure 2.15 denotes the distance from the trailing edge measured counter clockwise on the aerofoil. Hence, the value of S/c equal to one denotes the most forward sticking point of the wedge.

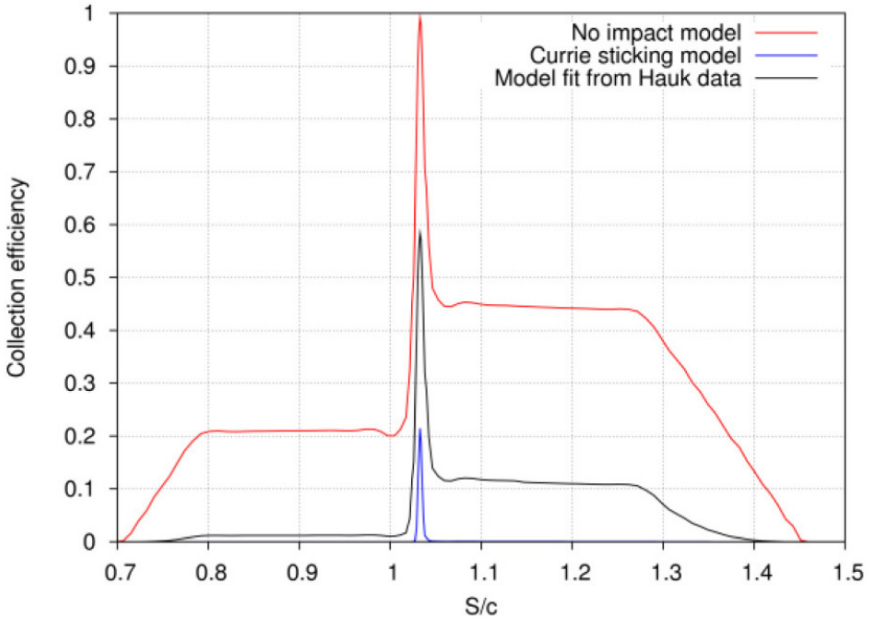

Figure 2.15: Graph of the catching efficiencies when no impact model is applied, when an impact model based on data from by Hauk et al. [13] is applied and when the model according to Currie et al. in [11] is applied. The figure is adapted from Iuliano et al. [20].

The shattering of ice crystals was accounted for in the model designed by Villedieu et al. [40]. Depending on the ratio $\mathcal{L}$ between the kinetic energy of an ice crystal and its surface energy they determined whether a crystal would bounce, shatter, or shatter and bounce. This ratio is given in Equation 2.82.

$$\mathcal{L} = \frac{1}{12} \frac{\rho_{ice} d_{ice} (v_n)^2}{e_{\sigma,0} \exp(\frac{Q}{RT} - \frac{Q}{RT_0})} \tag{2.82}$$

In this equation ρ_{ice} and d_{ice} denote respectively the density and diameter of an ice particle. The normal velocity of impact on the surface is denoted v_n. The expression for the surface energy per unit area sits in the denominator of Equation 2.82. Here the surface energy constant $e_{\sigma,0}$ equals 0.12 J/m^2. The activation energy Q is equal to 4.82×10^4 J/(mol K). The gas constant and absolute temperature are denoted R and T, where T_0 is equal to 253 Kelvin. A graph of Equation 2.82 is included in Figure 2.16. The value of T used when creating this graph is equal to 262 Kelvin. The value of $\mathcal{L}$ is seen to rapidly increase with temperature.

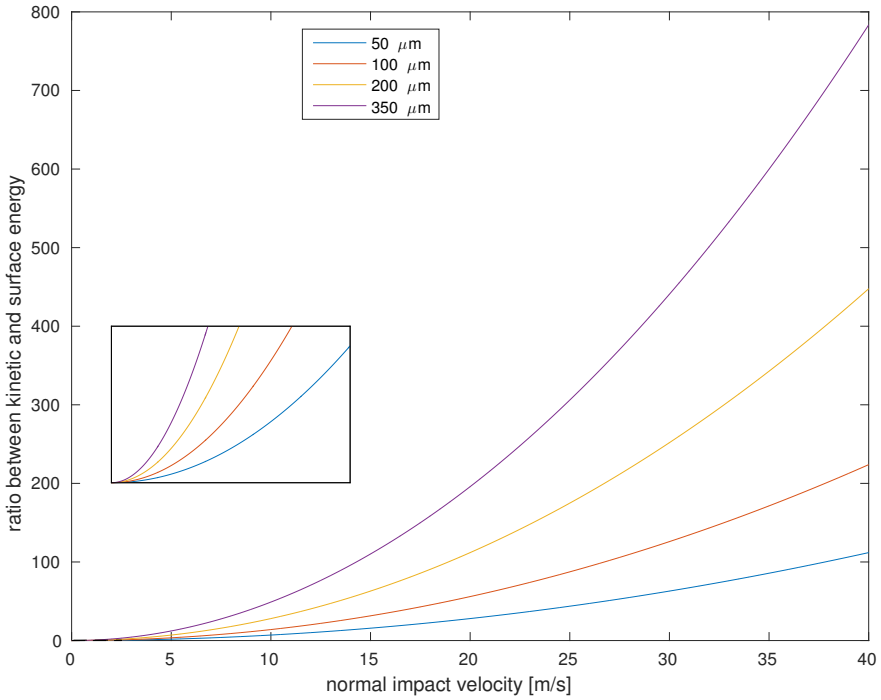

Figure 2.16: Plot of the ratio $\mathcal{L}$ between the kinetic and the surface energy for as a function of the normal impact velocity. Shown are the results for different particle diameters, the value for the temperature is chosen to be 262 Kelvin. The zoombox has x-dimensions [0;2.5] m/s and y-dimensions [0;0.5].

For values of $\mathcal{L}$ below a certain threshold $\mathcal{L} < \mathcal{L}_{c1}$, the ice crystal is assumed to bounce quasi-elastically without loss of kinetic energy. For values above a second threshold $\mathcal{L} > \mathcal{L}_{c2}$, the crystal is assumed to shatter with only very little kinetic energy left to rebound from the surface. The behaviour of crystals with values of $\mathcal{L}_{c1} < \mathcal{L} < \mathcal{L}_{c2}$ proved to be the most difficult to predict. For this range of values for $\mathcal{L}$ the crystal is assumed to scatter whilst retaining kinetic energy. Therefore the fractions of the scattered ice crystal contain kinetic energy which allows them to bounce from the surface. Using literature and experimental results, approximate values of $\mathcal{L}_{c1} \approx 0.5$ and $\mathcal{L}_{c2} \approx 90$ are suggested by Villedieu et al. [40]. The values of $\mathcal{L}_{c1}$ and $\mathcal{L}_{c2}$ will be dependent on the thickness of the water layer on top of the surface. Unfortunately, due to a lack of experimental data it was not possible to incorporate this in the determination of the values threshold values.

To account for the thickness of the water layer, a statistical approach is used. Somewhat similar to the method of Nilamdeen and Habashi in [28], the sticking fraction is determined dependent of particle size, water layer thickness and the fraction of the particle that has melted along its trajectory [40].

The velocity of the rebounding particle is determined using the normal and tangential restitution coefficients. Due to a lack of experimental data, the tangential restitution coefficient is assumed to be unity. For values of $\mathcal{L} < \mathcal{L}_{c1}$ the normal restitution coefficient is also assumed to be equal to one. For values of $\mathcal{L} > \mathcal{L}_{c2}$ it is assumed that the particle sticks to the wall and the the normal restitution coefficient is equal to zero. For values of $\mathcal{L}_{c1} < \mathcal{L} < \mathcal{L}_{c2}$ the normal restitution coefficient is defined in Equation 2.83. A graph of Equation 2.83 for values of $\mathcal{L}$ ranging between $\mathcal{L}_{c1}$ and $\mathcal{L}_{c2}$ is shown in Figure 2.17.

$$\xi_n = \left(\frac{\mathcal{L}_{c1}}{\mathcal{L}}\right)^{1/3} \tag{2.83}$$

The velocity vector of the rebounding particle is determined using a combination of the impacting velocities, the restitution coefficient and a random unit vector tangential to the surface [40].

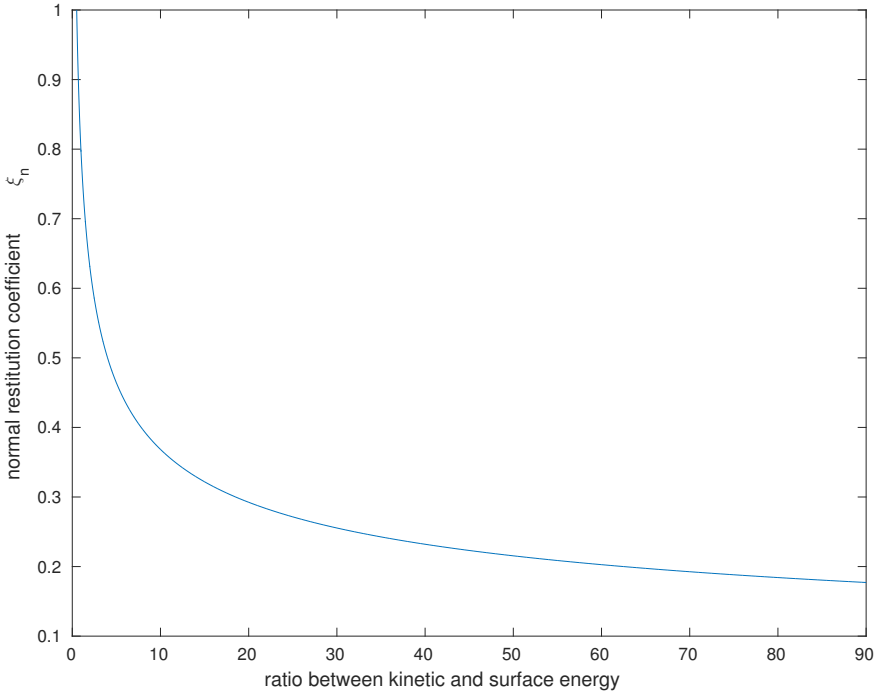

Figure 2.17: Graph of the normal restitution coefficient ξ_n for values of $\mathcal{L}$ ranging between $\mathcal{L}_{c1}$ and $\mathcal{L}_{c2}$

Chapter 3

Design of an extended Messinger model

The algorithm designed to predict the ice growth on an aerofoil caused by impinging ice crystals and water droplets is inspired by the original Messinger model and the work of CIRA, INTA and ONERA as presented in Section 2.6 [19, 25]. In the HAIC project a number of benchmarks are defined, which will be used to validate the outcomes of the new algorithm. In general the benchmarks are provided with the outcome of wind tunnel experiments and numerical simulations, similar to the simulations carried out in this research.

3.1 Input

The input data for the algorithm consists of the geometry of the aerofoil, flow properties and a catching efficiency of impinging particles. The geometry is captured in a mesh of the surface area as illustrated in Figure 3.1. For every node connecting two elements the input data is known or can be derived. Flow properties are for instance the free stream velocity, temperature and pressure, the temperature of the impinging particles and other thermodynamic properties. The catching efficiency is obtained from the solution of the flowfield and the particle trajectories around the aerofoil. The flow field and the particle trajectories are solved using a Eulerian-based computational method (MooseMBIce) developed in the group of Engineering Fluid Dynamics from the University of Twente. For more information regarding the flow field and particle trajectories is referred to Iuliano et al. [20]. From the particle trajectories a catching efficiency β_{ice} is defined for impinging ice crystals, whilst the catching efficiency for water β_{water} denotes the amount of impinging water. This water may be formed along the inlet trajectory of the turbine engine, when the ice crystals start to melt. The partly melted particles consist of a solid core and a mushy (liquid) shell. This is for instance also the case in HAIC benchmark number seven, where a melt ratio is given for the ice crystals entering the wind tunnel [38].

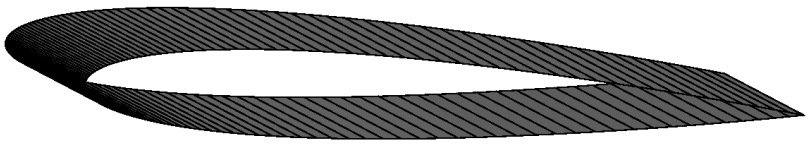

Figure 3.1: Example of a surface mesh of a NACA 0012 profile.

The input data is sorted clockwise around the aerofoil, starting from the trailing edge. Using the velocity field at the surface, the location of the leading edge is determined. This is demonstrated in

pseudo code in Algorithm 1. The normal and tangential vectors are determined using the geometry of the aerofoil. The procedure for this operation is given in Algorithm 2.

The format of the input data is the Plot3d file format which is used for writing CFD structured grids and solutions. From the input trajectory data of the ice crystals and water droplets only the catching efficiency is used. From the solution of the flow field of air the density, temperature and velocity is used. It is assumed that these are the values of the variables at the edge of the boundary layer.

Algorithm 1: Determination of the stagnation point

input : velocity field around the aerofoil
output: stagnation point

for $i = 1$ **to** *nCoordinates* **do**
    u_abs(i) = $\sqrt{\text{u(i)}^2 + \text{v(i)}^2}$
    if *i is on front half of aerofoil .AND. u_abs(i) < u_star* **then**
        u_star = u_abs(i)
        sp_coordinate = coordinate(i)
        sp_location = i
    end
end

Algorithm 2: Normal and tangential vectors

input : coordinates of the aerofoil
output: normal and tangential vectors

for $i = 1$ **to** *nCoordinates* **do**
    step_x(i) = coordinate(i+1,1) - coordinate(i,1)
    step_y(i) = coordinate(i+1,2) - coordinate(i,2)
    `/* the trailing edge is treated slightly different since the first and the last point of the aerofoil are positioned on the same coordinate */`
    if *i = nCoordinates* **then**
        step_x(i) = coordinate(2,1) - coordinate(i,1)
        step_y(i) = coordinate(2,2) - coordinate(i,2)
    end
    steplength(i) = $\sqrt{\text{step\_x(i)}^2 + \text{step\_y(i)}^2}$
    normal_x(i) = -step_y(i) / steplength(i)
    normal_y(i) = step_s(i) / steplength(i)
end

3.2 Output

The output data consists of the mass and energy flows, the surface temperatures and the coordinates of the outer edges of the ice layer. The net mass and energy flow are also part of the output, these values should equal zero. The coordinates of the ice layer are determined from the mass flow of freezing mass and the mass flow of impinging particles. Note that the freezing mass flow can also be negative, indicating that impinging ice crystals melt on the surface. With the mass flow into the ice layer known, its thickness can be determined from the density of ice, the area of the surface element and the icing time. Applying a similar procedure using the mass flow of water leaving the control volume it would also be possible to calculate the thickness of the water layer.

3.3 Ice accretion

The ice accretion part is the main part that solves the mass and energy balance for every element resulting in a prediction of the thickness of the ice layer. The central idea in this routine is that the sum of all energies should equal zero for every element. To accomplish this, the freezing or melting mass rate is determined while the temperature is set equal to the freezing temperature. When the freezing or melting mass rate exceeds a maximum value the temperature is determined by using this maximum value for the freezing or melting mass rate. This process is outlined in the flowchart in Figure 3.4.

Mass balance

The mass balance was introduced in Section 2.3. A schematic representation of the mass balance as used in the icing code introduced here is shown in Figure 3.2. The mass terms and their mathematical relations are listed in Table 3.1. As can be seen from Figure 3.2, it is assumed that the impinging

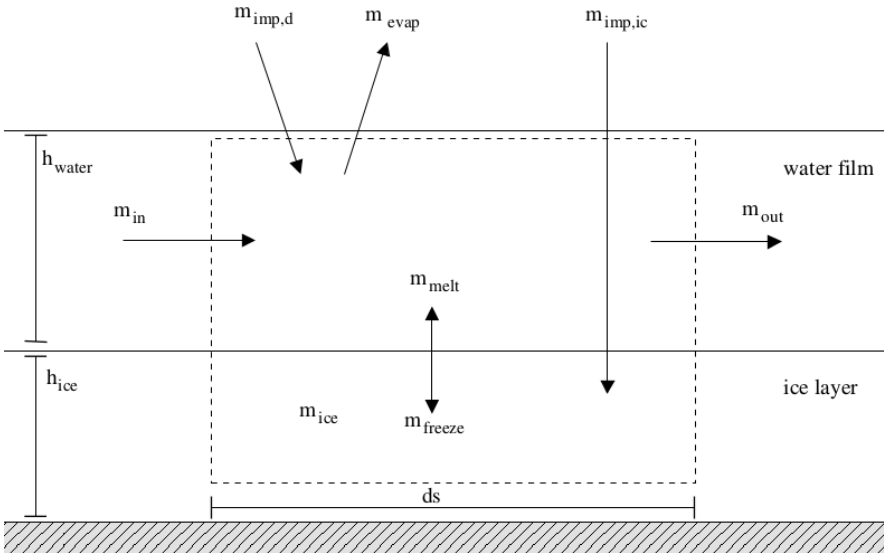

Figure 3.2: Schematic representation of the mass balance.

water moves into the water layer, whilst the impinging ice crystals move directly into the ice layer. Therefore the amount of ice in the ice layer is equal to the freezing mass and the amount of impinging ice crystals together.

$$\dot{m}_{sol} = \dot{m}_{imp,ic} + \dot{m}_{freeze} - \dot{m}_{melt} \tag{3.1}$$

In Equation 3.1 the term $\dot{m}_{sol}$ denotes the amount of solid (ice) in the ice layer. Since freezing and melting will not occur at the same time, $\dot{m}_{freeze}$ is defined as the mass transfer between the solid and the liquid state. For melting the term $\dot{m}_{freeze}$ is set to have a negative value. Therefore Equation 3.1 can be rewritten as

$$\dot{m}_{sol} = \dot{m}_{imp,ic} + \dot{m}_{freeze} \tag{3.2}$$

Similar the amount of liquid (water) in the water layer can be set equal to the water flowing in from the previous element, the impinging water droplets and the melting ice together. Since it is defined that the part of the water which remains unfrozen is flowing into the next element, the runback water is defined as in Equation 3.3

$$\dot{m}_{out} = \dot{m}_{imp,d} + \dot{m}_{in} - \dot{m}_{freeze} \tag{3.3}$$

Energy balance

The energy balance was introduced in Section 2.3. A schematic representation of the energy balance as used in the icing code introduced here is shown in Figure 3.3. The energy and enthalpy terms and

their mathematical relations are listed in Table 3.1.

The energy change associated with mass evaporation is left out of the energy balance. The reason for this is that the presence of evaporation in the energy balance would require an iterative method for solving. As shown in Section 2.5 the mass evaporation depends directly on the surface temperature. The strategy therefore used is to first solve the mass and energy balance without taking evaporation into the equation. With the surface temperature known, the amount of mass that evaporates is calculated. This mass lost due to evaporation is subtracted from the mass of water that leaving the control volume as runback water.

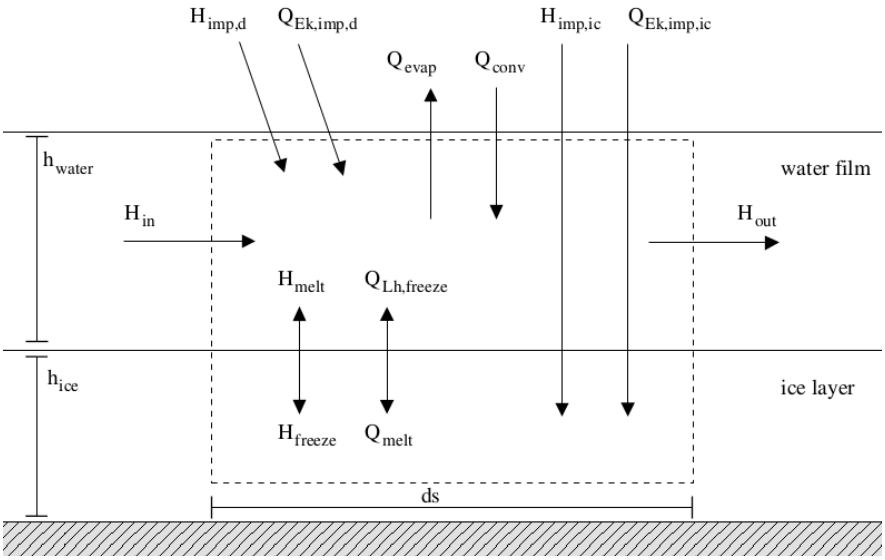

Figure 3.3: Schematic representation of the energy balance.

The potential energy contribution from the impinging water droplets and ice crystals are a result of the temperature difference between the particles and the surface. Thereby they also contribute their kinetic energy.

The energy term associated with the phase changes between water and ice out of three parts. One part is the latent heat required for the actual phase change, the other terms accounts for the temperature difference between the surface temperature and the freezing temperature. Note that H_{melt} and H_{freeze} in Figure 3.3 are actually on and the same term, since $H_{melt} = H_{freeze}$.

$$\dot{H}_{freeze} = \dot{m}_{freeze} \left[Lh_{freeze} + Cp_w(T - T_{freeze}) + Cp_i(T_{freeze} - T) \right] \tag{3.4}$$

Here Cp_w and Cp_i denote the specific heat of water and ice respectively, T is the surface temperature and T_f is the temperature of freezing. Note that when $T = T_{freeze}$, which is the starting condition for the algorithm, only the latent heat remains. When $T < T_{freeze}$, the amount of mass freezing is set equal to the fraction of liquid water entering the control volume $\dot{m}_{freeze} = \dot{m}_{imp,d} + \dot{m}_{in}$. Similarly when $T > T_{freeze}$ the melting mass is set equal to the amount of ice crystals entering the control volume $-\dot{m}_{freeze} = \dot{m}_{imp,ic}$.

The change in enthalpy due to the inflowing or outflowing runback water from unfrozen water is defined as the product of the mass flow, the specific heat and the temperature difference between the runback water and the element. For the inflow of runback water this reads as

$$\dot{H}_{in} = Cp_w \dot{m}_{in}(T_{in} - T) \tag{3.5}$$

where T is the surface temperature of the element. For the outflow of runback water this is written as

$$\dot{H}_{out} = Cp_w \dot{m}_{out}(T - T_{out}) \tag{3.6}$$

The temperature of the runback water is defined as the temperature of the element from where it originates. For the inflow this the temperature of the previous element $T_{in} = T_{prev}$. The temperature

of the outflowing runback water is equal to temperature of the element itself, hence the change in enthalpy due to the outflowing water is zero by definition $\dot{H}_{out} = 0$.

Convective heating is caused by the temperature difference between the the external flow and the element itself. The temperature of the flow near the surface is higher than the temperature of the flow far upstream of the surface. This is caused by the flow decelerating in the vicinity of the surface. The derivation of this recovery temperature is given in Section 2.4, together with the convective heat transfer coefficient. The expression used to determine the convective heat transfer rate is given by

$$\dot{Q}_{conv} = h_c(T - T_{rec})ds \tag{3.7}$$

with h_c [m/s] the heat transfer coefficient [m/s], T_{rec} the recovery temperature and ds the length of the element.

Free energy

The free energy Q^* is the sum of all the terms in the energy balance. The only two unknown variables in the energy balance are the amount of freezing mass $\dot{m}_{freeze}$ and the surface temperature T of the element. The energy balance is a linear equation with two unknowns, so an additional equation is required to solve the unknowns. Therefore the initial assumption is introduced that the surface temperature is equal to the freezing temperature $T = T_{freeze}$.

The energy balance with two variables is given in Equation 3.8.

$$\dot{H}_{imp,ic} + \dot{H}_{imp,d} + \dot{Q}_{ek,imp,ic} + \dot{Q}_{ek,imp,d} + \dot{H}_{in} + \dot{Q}_{conv} + \dot{Q}_{freeze} = 0 \tag{3.8}$$

Its extended form is shown in Equation 3.9.

$$\begin{aligned} Cp_i(T_{imp,ic} - T)\dot{m}_{imp,ic} + Cp_w(T_{imp,d} - T)\dot{m}_{imp,d} + \frac{1}{2}(\dot{m}_{imp,ic} + \dot{m}_{imp,d})U_\infty^2 + \\ + Cp_w(T_{in} - T)\dot{m}_{in} + h_c(T_{rec} - T)ds + Lh_{freeze}\dot{m}_{freeze} + \\ - Cp_w\dot{m}_{freeze}(T_{freeze} - T)\dot{m}_{freeze} + Cp_i(T_{freeze} - T)\dot{m}_{freeze} = 0 \end{aligned} \tag{3.9}$$

When T_{freeze} is filled in for T, Equation 3.9 is reduced to Equation 3.10.

$$\begin{aligned} Cp_i(T_{imp,ic} - T_{freeze})\dot{m}_{imp,ic} + Cp_w(T_{imp,d} - T_{freeze})\dot{m}_{imp,d} + \frac{1}{2}(\dot{m}_{imp,ic} + \dot{m}_{imp,d})U_\infty^2 + \\ + Cp_w(T_{in} - T_{freeze})\dot{m}_{in} + h_c(T_{rec} - T_{freeze})ds + Lh_{freeze}\dot{m}_{freeze} = 0 \end{aligned} \tag{3.10}$$

Now the freezing mass can be solved from the energy balance in Equation 3.10. This is given in Equation 3.11.

$$\dot{m}_{freeze} = \frac{-Q^*(T)|_{T=T_{freeze}}}{Lh_{freeze}}\,, \tag{3.11}$$

$$\begin{aligned} \text{where} \quad q^*(T)_{T=T_{freeze}} = Cp_i(T_{imp,ic} - T_{freeze})\dot{m}_{imp,ic} + Cp_w(T_{imp,d} - T_{freeze})\dot{m}_{imp,d} + \\ + \frac{1}{2}(\dot{m}_{imp,ic} + \dot{m}_{imp,d})U_\infty^2 + Cp_w(T_{in} - T_{freeze})\dot{m}_{in} + h_c(T_{rec} - T_{freeze})ds \end{aligned}$$

When the freezing mass rate $\dot{m}_{freeze}$ turns out to be larger than the total amount of water entering the element $\dot{m}_{imp,d} + \dot{m}_{in}$, the assumption that the surface temperature equals the freezing temperature $T = T_{freeze}$ can no longer be maintained. Since in order to keep $T = T_{freeze}$, more water should freeze than is available. To solve this the new assumption is introduced that all water freezes $\dot{m}_{freeze} = \dot{m}_{imp,d} + \dot{m}_{in}$.
Using this assumption the energy balance from Equation 3.9 can be written as given in Equation 3.12.

$$\begin{aligned} Cp_i(T_{imp,ic} - T)\dot{m}_{imp,ic} + Cp_w(T_{imp,d} - T)\dot{m}_{imp,d} + \frac{1}{2}(\dot{m}_{imp,ic} + \dot{m}_{imp,d})U_\infty^2 + \\ + Cp_w(T_{in} - T)\dot{m}_{in} + h_c(T_{rec} - T)ds + \\ \big(Lh_{freeze} + (Cp_i - Cp_w)(T_{freeze} - T)\big)(\dot{m}_{imp,d} + \dot{m}_{in}) = 0 \end{aligned} \tag{3.12}$$

Here all the terms in Equation 3.9 featuring the term $\dot{m}_{freeze}$ are combined and the term $\dot{m}_{freeze}$ itself is substituted with $\dot{m}_{imp,d} + \dot{m}_{in}$.

Using a similar reasoning it can be stated that when the melting mass rate $-\dot{m}_{freeze}$ exceeds the total amount of ice entering the element $\dot{m}_{imp,ic}$, a new assumption is required to balance the energy terms. This new assumption is that all the ice melts $\dot{m}_{freeze} = -\dot{m}_{imp,ic}$. Similar to Equation 3.12 the energy balance in Equation 3.13 is derived from Equation 3.9.

$$\begin{aligned} Cp_i(T_{imp,ic} - T)\dot{m}_{imp,ic} + Cp_w(T_{imp,d} - T)\dot{m}_{imp,d} + \frac{1}{2}(\dot{m}_{imp,ic} + \dot{m}_{imp,d})U_\infty^2 + \\ + Cp_w(T_{in} - T)\dot{m}_{in} + h_c(T_{rec} - T)ds + \\ \big(Lh_{freeze} + (Cp_i - Cp_w)(T_{freeze} - T)\big)\dot{m}_{imp,ic} = 0 \end{aligned} \tag{3.13}$$

From Equation 3.12 and Equation 3.13 the surface temperature T can be found by solving Equation 3.14. Here $\dot{m}_{freeze}$ should be substituted by either $-\dot{m}_{imp,ic}$ or $\dot{m}_{imp,d} + \dot{m}_{in}$, dependent which freezing or melting scenario is chosen.

$$T = \frac{f(\dot{m}_{freeze})}{g(\dot{m}_{freeze})} \tag{3.14}$$

$$\begin{aligned} \text{where} \quad f(\dot{m}_{freeze}) = Cp_i T_{imp,ic}\dot{m}_{imp,ic} + Cp_w T_{imp,d}\dot{m}_{imp,d} + \frac{1}{2}(\dot{m}_{imp,ic} + \dot{m}_{imp,d})U_\infty^2 + \\ + Cp_w T_{in}\dot{m}_{in} + h_c T_{rec} ds + \big(Lh_{freeze} + (Cp_i - Cp_w)T_{freeze}\big)\dot{m}_{freeze} \end{aligned}$$

$$\text{and} \quad g(\dot{m}_{freeze}) = Cp_i\dot{m}_{imp,ic} + Cp_w\dot{m}_{imp,d} + Cp_w\dot{m}_{in} + h_c ds + (Cp_i - Cp_w)\dot{m}_{freeze}$$

From Equation 3.14 the surface temperature can be calculated.

Figure 3.4: Flowchart for the routine of find the correct freezing mass rate and surface temperature.

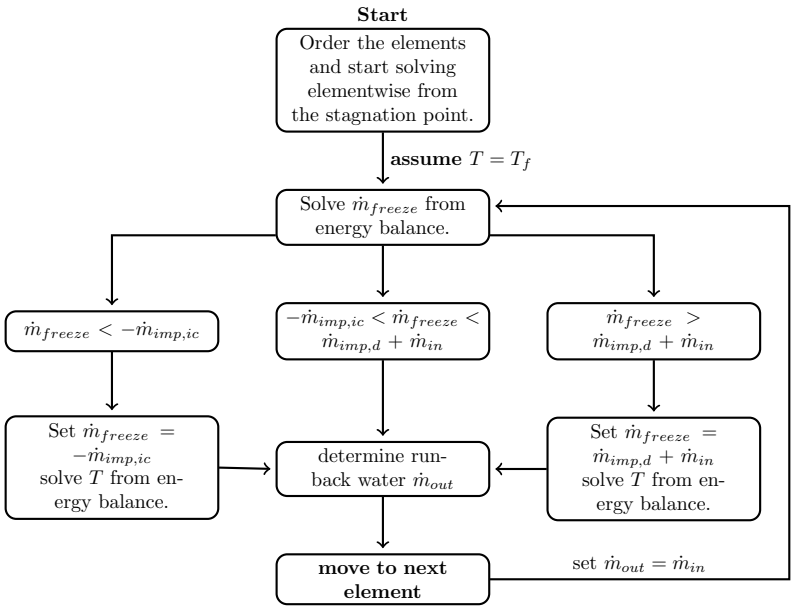

Initial assumption

The initial assumption that the surface temperature is equal to the freezing temperature is chosen since it allows the coexistence of water and ice in the same control volume. Although the water and ice in the control volume are assumed to form two separated layers in the model introduced here, it is more likely that in reality they form a sort of mushy mixed phase. Within the limits of this model, this coexistence at $T = T_{freeze}$ is the best possible representation of this mushy mixed phase.

Table 3.1: Overview of the individual mass and energy flux terms in the mixed-phase models.

symbol	formula	description
$\dot{m}_{in}$	$\iint_{\partial V_1} \rho_w \vec{u}_{in} \cdot \hat{n}_1 dS_1$	mass flow of water into the control volume
$\dot{m}_{out}$	$\iint_{\partial V_2} \rho_w \vec{u}_{out} \cdot \hat{n}_2 dS_2$	mass flow of water out of the control volume
$\dot{m}_{imp,d}$	$\iint_{\partial V_3} \beta_d \, LWC \, \vec{U}_\infty \cdot \hat{n}_3 dS_3$	droplets being caught by the surface
$\dot{m}_{imp,ic}$	$\iint_{\partial V_3} \beta_{ic} \, IWC \, \vec{U}_\infty \cdot \hat{n}_3 dS_3$	ice crystals being caught by the surface
$\dot{m}_{evap}$	$\iint_{\partial V_3} \bar{\rho} h_m (Y_{vs} - Y_{ve}) \hat{n}_3 dS_3$	the fraction of water that evaporates into the layer of air outside of the control volume
$\dot{m}_{freese}$	$f(\dot{m}_{in} + \dot{m}_{imp})$	mass flow out of the control volume due to freezing liquid
$\dot{H}_{in}$	$Cp_w(T_{in} - T_s)\dot{m}_{in}$	change in enthalpy due to the temperature difference between the inflowing run back water and the volume
$\dot{H}_{out}$	$Cp_w(T_s - T_{out})\dot{m}_{out}$	change in enthalpy due to the temperature difference between the outflowing run back water and the volume
$\dot{H}_{imp,d}$	$Cp_w(T_{imp,d} - T_s)\dot{m}_{imp,d}$	change in enthalpy to bring the temperature of impinging droplets to the temperature of the volume
$\dot{H}_{imp,ic}$	$Cp_i(T_{imp,ic} - T_s)\dot{m}_{imp,ic}$	change in enthalpy to bring the temperature of impinging droplets to the temperature of the volume
$\dot{H}_{freeze}$	$Cp_w(T_s - T_f)\dot{m}_{freeze}$	change in enthalpy due to freezing water leaving the control volume
$\dot{Q}_{Lh,f}$	$Lh_f \dot{m}_{freeze}$	latent heat of freezing
$\dot{Q}_{Ek,imp,d}$	$\frac{1}{2}U_\infty^2 \dot{m}_{imp,d}$	kinetic energy of impinging droplets
$\dot{Q}_{Ek,imp,ic}$	$\frac{1}{2}U_\infty^2 \dot{m}_{imp,ic}$	kinetic energy of impinging ice crystals
$\dot{Q}_{conv}$	$\iint_{\partial V_3} h_c(T - T_{rec}) \, dS$	energy lost due to convective cooling
$\dot{Q}_{Lh,sub}$	$Lh_{evap}\dot{m}_{evap}$	latent heat of sublimation
$\dot{Q}_{Lh,evap}$	$Lh_{evap}\dot{m}_{evap}$	latent heat of evaporation
$\dot{Q}_{Lh,melt}$	$Lh_{evap}\dot{m}_{evap}$	latent heat of melting ice crystals
Q^*	free energy in control volume	amount of latent heat required at $Ts = Tf$ for a physical phase change

Thereby it is also a realistic approximation to the temperature of the initial compressor stages of a turbine engine operating at cruising altitude. The temperature inside the turbine engine peaks at a value of roughly 1500 Kelvin inside the combustion chamber. The temperature of the flow at the inlet is however more or less equal to the ambient temperature. Along the inlet trajectory the temperature is increased to a value of about 700 Kelvin inside the compressor of the turbine engine [36]. At an altitude of 10 km, the temperature is defined to be about 220 Kelvin by the standard atmosphere [5]. Hence, somewhere between the engine inlet and the exit of the compressor the temperature of the flow and the engine itself will be equal to the freezing temperature of water.

The influence of the choice for the initial temperature assumption will be researched, since it can be argued that it will not be of any influence on the resulting solution. Arguments for this would be that the additional assumptions such as that the coexistence of water and ice the same element is only allowed when $T = T_{freeze}$ provides a sufficient restriction to rule out additional equilibrium points for combinations of the freezing mass and surface temperature. The initial assumption $T = T_{freeze}$ does however present a very good starting point to determine if freezing or melting will occur and if a temperature should be found above or below the freezing temperature.

Particle impingement

No particle impingement model is taken into account with the model introduced in this report. The particle impingement is planned to be taken into account with the model calculating the flow field and particle trajectories. The development of particle impingement model is still in progress. Therefore it has been assumed in this research that every crystal and droplet impinging the surface will stick to it.

Erosion

The erosion model introduced in Section 2.7 as suggested by Wright et al. [43] is applied in to the model in this research. The data used by Wright et al. to calibrate the erosion factor is available via the HAIC project [41]. This data will also be used to calibrate the erosion factor applied to the model introduced in this report. Different values for the erosion factor will be researched for calibration and to gain insight in the behaviour of the erosion model.

Particle bin distribution

In reality, the ice crystals and water droplets that imping the surface will not be of uniform size. Therefore a size dependent distribution is created that groups the particles over a number of bins. Each bin contains of particles with the same size. The particle trajectories will therefore slightly vary between bins, since the drag is the dominating force in determining the particle trajectory [17]. The particle bin distribution will also proof useful in future versions when particle shattering is included. The pieces of a particle that shatters will then move into a bin corresponding to a smaller size. For the mass flux of impinging particles the bin distribution will make no difference, since this is dependent of the catching efficiency and the LWC or IWC. The impinging mass as defined for multiple bins is given in Equation 3.15 and Equation 3.16.

$$\dot{m}_{imp,d} = \sum_{n=1}^{\#\text{bins}} \beta_{d,n} \, LWC \, U_\infty^2 ds \tag{3.15}$$

$$\dot{m}_{imp,ic} = \sum_{n=1}^{\#\text{bins}} \beta_{ic,n} \, IWC \, U_\infty^2 ds \tag{3.16}$$

Although in reality the particles will also vary in size, it is for the research presented in this report assumed that the particles are of uniform spherical size. The influence of particle shape is however planned to be accounted for in the model that solves the particle trajectories [20].

3.4 HAIC benchmarks

Within the HAIC project a number of benchmarks are defined to validate the tools and models developed to predict ice accretion. These benchmarks are used to demonstrate a certain Technology Readiness Level (TRL) which indicates the maturity of the technology developed. With the benchmarks used in this report TRL 4 should be obtained, which corresponds by the standards of the European Union to a technology being validated in the lab [39]. The highest level possible is TRL 9, which is the standard for an actual system in an operational environment. The highest level to be reached in the HAIC project is TRL 6, a technology demonstrated in a relevant environment [12] [39].

The four benchmarks defined to demonstrate TRL 4 consist of both experimental and numerical results. Two of the four benchmarks (TC8 and TC9) make use of a NACA 0012 wing profile, the third benchmark (TC3) uses a wedge whilst the last benchmark (TC7) makes use of a half cylinder with a streamlined afterbody. One of the NACA 0012 benchmarks (TC8) uses a heated leading edge for anti-icing. Since this is not incorporated in the model reviewed in this report, TC8 is not reviewed here. Only TC7 and TC9 will be used to test the model, since this will provide sufficient insight in the performance and capabilities of the model at the current stage of development.

3.4.1 Test case 7 - The crowned cylinder

The crowned cylinder, whose the three dimensional geometry is shown in Figure 3.5, is the object of study for one of the benchmarks issued by the HAIC project. The diameter of the cylinder varies with

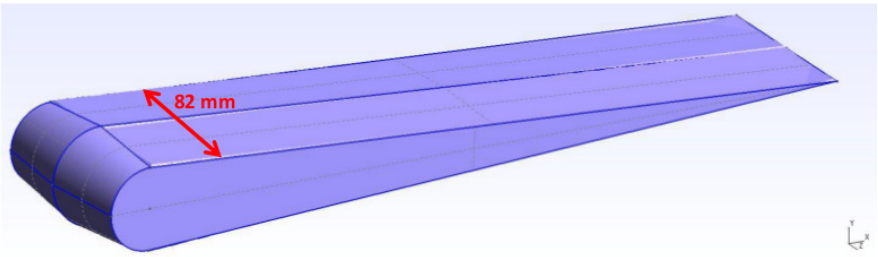

Figure 3.5: graphic representation of the crowned cylinder [38].

the span, reaching a maximum value of 44.6 mm at midspan, whilst the both ends hold a diameter of 36.8 mm. The length of the streamlined afterbody is 330 mm. For two-dimensional calculations it is intended to use the midspan geometry.

Table 3.2: Overview of the test setup parameters of the crowned cylinder wind tunnel experiments conducted in the NRC's RATFac altitude chamber [38].

Cylinder midplane diameter	0.0446 m
Cylinder sideplane diameter	0.0368 m
Afterbody length	0.3300 m
Angle of Attack	0 deg
Ice mean volume diameter	45 μm or according to 7-bin distribution
Initial particle temperature	273.15 K
Particle sphericity	1
Ice density	917 kg/m^3

A set of runs has been selected from the work of Currie et al., who performed wind tunnel tests as well as numerical simulations of the ice growth on the crowned cylinder [11]. These are distinguished by air flow conditions and ice particle parameters, introduced in Table 3.4 and Table 3.5. The values of the absolute humidity Yv1, Yv2 and Yv3 in Table 3.4 are given in Table 3.6. The wind tunnel experiments where conducted in the RATFac altitude chamber of the Canadian National Research Council (NRC). In the wind tunnel experiments a grinder was used to create the ice particles. The flow of these ice particles entering the wind tunnel mixes with a warm air stream, resulting in a net temperature which may well be above the freezing temperature. The ice crystals in this stream will therefore be partly melted when entering the test section of the wind tunnel [11]. Since the ice crystals now contain both ice and water, they will stick instantly to the surface they impact. The experiments were conducted with ice crystals only, so no water droplets were injected into the flow.
In the numerical simulations it may be assumed that the ice particles are of perfect sphericity. They enter the control volume with the free stream velocity at a temperature of 273.15 Kelvin. The mean volume diameter (MVD) of the particles is 45 μm in the case of a monodisperse size distribution, or divided over seven bins according to Table 3.3 in the case of a polydisperse distribution. The remaining test setup parameters are shown in Table 3.2.

Table 3.3: The 7-bin polydisperse size distribution [38].

Bin	1	2	3	4	5	6	7
Particle diameter [μm]	14.5	23	29	34.3	39.4	45	77.5
Mass fraction [%]	5	10	10	10	10	10	45

Table 3.4: Air flow conditions of the crowned cylinder wind tunnel experiments conducted in the NRC's RATFac altitude chamber [38].

Run	Ma	U_∞ [m/s]	a [m/s]	T_0 [K]	T_s [K]	p_0 [kPa]	p_s [kPa]	Absolute humidity
47	0.25	84.5	338	288.15	284.55	34.5	33.0	Yv2, Yv3
17, 77	0.25	84.5	338	288.15	284.55	34.5	33.0	Yv1, Yv2
67, 92, 57	0.25	84.5	338	288.15	284.55	34.5	33.0	Yv2, Yv3
233	0.4	136	335	288.15	278.95	34.5	30.8	Yv1, Yv2
238, 243, 246	0.4	136	335	288.15	278.95	34.5	30.8	Yv2, Yv3

Table 3.5: Ice particle parameters of the crowned cylinder wind tunnel experiments conducted in the NRC's RATFac altitude chamber [38].

Run	Melt ratio η [%]	TWC [g/m^3]	Accretion time t_{ac} [s]
17	6	6	300
47	16.6	4	61, 320
57	14	12	40, 116, 290
67	16.6	6	31, 148, 382
77	11.2	6	300
92	26.4	6	300
233	8.6	6	300
238	14	6	300
243	17.2	6	300
246	21.4	6	300

Table 3.6: Values of the humidity Yv [38].

	Ma	Yv [g/m^3]	T_{wb_0} [K]	Relative humidity [%]
Yv1	0.25	5.78×10^{-3}	273.15	23
Yv2	0.25	9.75×10^{-3}	276.15	38
Yv3	0.25	14.30×10^{-3}	279.15	56
Yv1	0.4	6.59×10^{-3}	273.15	35
Yv2	0.4	10.80×10^{-3}	276.15	57
Yv3	0.4	15.60×10^{-3}	279.15	81

According to the HAIC test case description cited in [38], run 17 to 92 can be used to demonstrate the behaviour of the model dependent of melt ratio η. With increasing melt ratio, the thickness of the accreted ice layer is expected to increase until it reaches a certain maximum. After reaching maximum thickness, the ice layer is expected to reduce when the melt ration η is further increased. The effect of erosion on the rate of ice growth and on the final ice shape in steady state can also be assessed from this set of runs. Run 233 to 246 can be used to check the behaviour of the model when subjected to a higher Mach number flow.

In this research only runs 47, 57, 67 and 238 will be reviewed, since from these runs the results are published in [11, 38].

3.4.2 Test case 9 - NACA 0012

Measurements of mixed-phased-flow ice accretion on a NACA 0012 aerofoil were performed by Al-Khalil et al. in the Cox icing wind tunnel [3]. The ice crystals were produced by a snow gun and a ice shaver and had a mean volume diameter of 150 and 200 μm respectively. The supercooled water droplets had a mean volume diameter of 20 μm. An example of the size distribution is shown in Figure 3.6. The NACA 0012 aerofoil has a cord length of 36", which equals 0.9144 m, and is installed under an angle of attack of zero degree. All the tests were conducted at a free stream velocity of 120 mph, which equals 53.64 m/s. The duration of the icing conditions in the runs was 10 minutes,

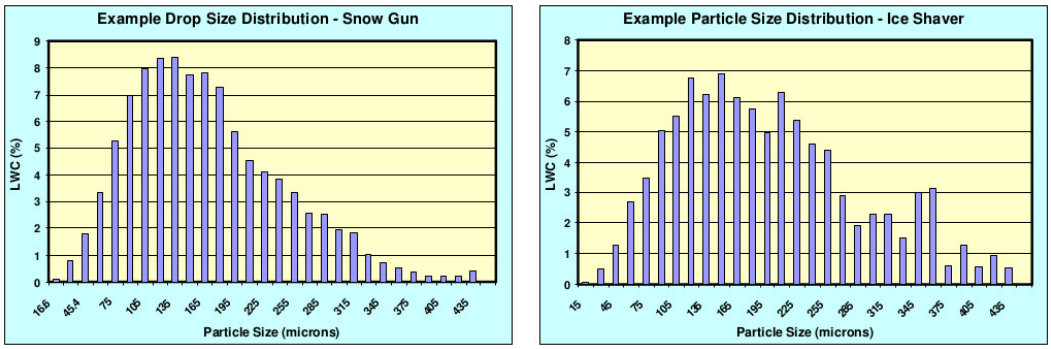

Figure 3.6: Particle diameter distribution in μm as percentage of the liquid water content (LWC). Left it is shown for the snow gun, right is for the ice shaver [3].

or until stable results were observed. The ambient total temperature of the experiments observed was 12 degree Fahrenheit, equalling 262.0 Kelvin, and 22 degree Fahrenheit, which equals 267.6 Kelvin. No information is found regarding the temperature of the ice particles [3]. From the experiments in

Table 3.7: Overview of the test setup parameters in the Cox icing wind tunnel.

Cord length	0.9144 m
Angle of attack	0 degree
Snow gun MVD	150 μm
Ice shaver MVD	200 μm
Water droplet MVD	20 μm
Max test duration	10 minutes

the Cox icing wind tunnel four different runs are selected for the HAIC test case [41]. The same runs were selected and reviewed by Nilamdeen and Habashi to verify their numerical results [28]. The parameters for these four different runs are given in Table 3.8. The numerical results from the work of Nilamdeen and Habashi will be used together with the experimental results by Al-Khalil et al. to evaluate the model presented in this report.

Table 3.8: Test conditions in the Cox icing wind tunnel.

Case	Temp. [K]	U_∞ [m/s]	IWC [g/m^3]	LWC [g/m^3]
19	262.0	54.64	0.7 (snow gun)	0.3
20	262.0	54.64	0.3 (snow gun)	0.7
9	267.6	54.64	0.0 (ice shaver)	0.7
10	267.6	54.64	0.7 (ice shaver)	0.7

The HAIC test case description cited in [41] states that the results from Run 9,10 and Run 19, 20 can be used to review the effect of erosion implemented in the model. Apart from the results as shown in Figure 2.14 no result data is provided in the test case description, nor in the literature on which the test case is based cited in [3]. Therefore the graphical representation of the experimental results by Nilamdeen and Habashi will be used in this report [28].

3.5 Model validation and verification

The outcomes of a (simulation) model that has not been properly revised in terms of for instance reliability, accuracy and its limitations are not very valuable. It is therefore important to think about model validation and verification. Critical evaluation of a models output, if it actually makes some sense, is usually an important approach to begin with.

Validation versus verification

There is a lot of confusion regarding validation and verification [42]. The two terms are often misinterpreted, mixed up and synonymously used, falsely resulting in claims of authenticity or truth of the outcomes of a model [30].

According to Oreskes et al. cited in [30], stating that a model is verified, is the same as stating that its truth has been demonstrated, which is only possible for closed systems. Validation on the other hand is a measure for the legitimacy of a model, defined within a range of limitations [30].

A more practical distinction is made by Whitner and Balci cited in [42], who state that validation is to make sure that the input-output transformation of a model is sufficiently accurate in representing the input-output transformation of a the system it describes. Verification on the other hand deals with the accuracy with which the simulation model is developed. Or more popularly said: validation is building the right model, verification is building the model right [42].

3.5.1 Verification

The process of verification as described by Whitner and Balci is subdivided in six different verification perspectives [42]. Listed in order ascending of both effectiveness and complexity the perspectives are explained below.

Informal analysis is the evaluation by the human mind. It includes the process of check the logic of a model, as well as its consistency and completeness. This can be performed by the developer himself, or with an inspection team.

Static analysis can be performed without running the code. It consists of for instance a syntax analysis and a semantic analysis by checking if one can understand from an algorithm the intentions of a modeller. Also important are consistency checks, that all specifications are clear and no contradictions are present. Also the data flow within the code should be checked.

Dynamic analysis is applied during execution of the code. Examples are black-box and white-box testing. Whereas the latter tests the function of a model by looking at what actually happens during the execution of a part of the code, is black-box testing only concerned with input and output. The procedure here is basically to see how the output changes when the input is altered. Debugging and stress testing by subjecting the model to extremities it will never encounter under normal operation are also considered to be part of dynamic analysis. The model introduced in this report was programmed to display some of its intermediate results on the screen. Examples include the calculated location of the stagnation point and valued read from the input files. The model was also programmed to display a warning and possibly take action when faulty values were detected.

Symbolic analysis is the execution of a model with symbolic values instead instead of real values. If for instance the goal of a model is to double the value of the input and this is tested with symbolic input x, then the output should equal $2x$. With x possibly equal to any value, this symbolic analysis represents an infinitely number of tests with actual (non-symbolic) values.

Constraint analysis is verification by comparing model assumptions and actual conditions during execution. An example is to check if what the modeller assumes that happens, actually does happen during execution.

Formal analysis is the most effective of verifying software. It is a based on a formal mathematical proof of correctness and very difficult, if not impossible, to achieve.

Oreskes et al. refer to the use of an analytical solution to verify a model, which is comparable to formal and symbolic analysis. They state that using an analytical solution is actually not really verification, but rather benchmarking, since the model is only verified to conditions for which the analytical solution is also applicable [30].

Proper verification is very difficult, or actually impossible according to Oreskes et al. [30]. However a number of the methods for analysis as stated by Whitner and Balci [42] seem to be pretty straightforward. In particular informal, static and dynamic analysis seem to be pretty achievable. These three analysis methods were very involved in the design and development phase of the code. For a more detailed discussion towards model verification is referred to the work of Whitner and Balci [42].

3.5.2 Validation

Model validation is quoted by Sargent [35] as defined to mean "substantiation that a computerized model within its domain of applicability possesses a satisfactory range of accuracy consistent with the intended application of the model." In order to achieve this, Sargent gives a number of techniques [35]. Here only the techniques that are used in this report are introduced. For a complete overview of possible techniques the reader is referred to the work of Sargent [35].

Comparison to other models such as an analytical solution, or by comparing the results to the outcomes of other simulation model which have been validated. In the literature research presented in Section 2 of this report, a number of mixed-phase ice accretion codes are introduced. In order to make a meaningful comparison, both the results and the input parameters of a simulation should be known. The HAIC project contributes to the validation process by providing a number of benchmarks. Two of these are used in this research and introduced in Section 3.4.

Extreme condition tests to check if the model can cope with extremities which will not occur in reality. In icing codes an example would be to check the results for very large water contents. Thereby tests have been performed with ambient temperatures that are considerably higher and lower than reasonably can be expected in normal operation.

Face validity is to ask people, with a certain level of expertise on the subject, to evaluate if the behaviour and results of the model are plausible. During meetings with supervisors the behaviour and intermediate results of the in this report introduced model were discussed.

Historical data validation by using existing system date to test model behaviour. Apart from comparing start input and end output, it is also possible to insert historical data halfway the code to see how this alters the output at the end of the code. Sources of historical data are wind tunnel experiments. These outcomes are also included in the benchmarks introduced in Section 3.4. It would be interesting to have exact measurement data of the amounts of particles that stick to and bounce from the surface. This would make it possible to perform separate tests of the performance of the impingement code and the actual ice accretion code that solves the mass and energy balances.

Parameter Variability Sensitivity Analysis to check the dependence of the outcome of a model on different parameters. When is established which parameters provide the greatest influence on the outcome, sufficient accuracy should be established in these parameters. An example of how this tool is used in this report can be found within the evaluation of the mass evaporation term in Section 2.5. Apart from the derivation of the term, also its influence on the ice shape is studied.

Validation as defined by Whitner and Balci and Sargent provides a solid basis for checking and determining the accuracy of a model. From the different techniques provided by Sargent [35] the

majority can be relatively easy applied when sufficient system data is available. It is however very important to not overestimate the capabilities of a model, which is according to Oreskes et al. a common mistake [30]. For a more detailed discussion towards model validation is referred to the work of Sargent [35].

From three different authors, three different definitions for both verification and validation are found [30, 35, 42]. This illustrates the different views on, but also the importance of, model evaluation. Some of the techniques introduced for validation closely resemble the techniques for model verification. For instance extreme condition tests (validation) and stress testing (verification) seem very alike. Both techniques should however be interpreted with the statement introduced at the beginning of this section in mind: validation is building the right model, verification is building the model right [42].

Chapter 4

Results and discussion

The in Section 3 introduced model for calculating ice accretion in mixed-phase ice accretion will be evaluated in this chapter. Central in the first part of this chapter are the two test cases introduced in Section 3.4. They form the basis for the evaluation of the suggested mixed-phase ice accretion code. In the second part of this chapter some input parameters of the test cases will be altered to test the behaviour and responses of the model. First however the erosion reduction factor introduced in Section 2.7 will be determined.

4.1 Erosion

The erosive model applied to the in this report introduced ice accretion model is similar to the erosive model by Wright et al. [43] and was introduced in Section 2.7. This erosive model is an empirical model, effectively reducing the amount of ice crystals impinging the surface. The erosive reduction factor found by Wright et al. is based on wind tunnel experiments by Al-Khalil et al. [3]. To account for the differences between the GlennICE ice accretion model used by Wright et al. and the ice accretion model introduced in this report, different erosion factors are researched. Shown in Figure 4.1a are the ice profiles calculated by applying different values for the reduction of the amount of impinging ice crystals. The corresponding reference result from wind tunnel experiments used by Wright et al. to calibrate the erosion reduction factor is shown in Figure 4.1b which is adapted from [28].

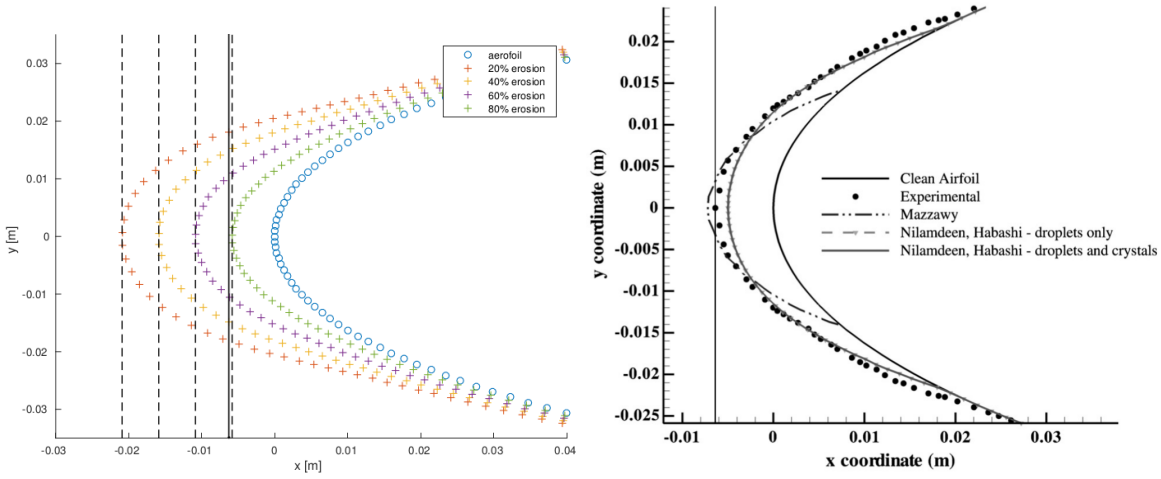

(a) Ice profiles for different erosion reduction factors.

(b) Reference measurement results [28].

Figure 4.1: Experimental and numerical used to determine the erosione reduction factor.

For the ice accretion model used by Wright et al. a reduction factor of 20% was found in [43]. From

Figure 4.1a can be learned that a factor of 20% does not give satisfactory results for the newly introduced ice accretion model. Rather an erosion factor of 80% results in the desired ice shape. This implies that only 20% of the impinging ice crystals are to be taken into account in the mass and energy balances.

The difference between the model introduced in this report and the model from Wright et al. is that the latter requires the presence of a water film for ice crystals to stick to the surface [43]. This gives rise to the idea that a particle impingement model is being used by Wright et al.. In the model introduced in this report it is assumed that every ice crystal impinging the surface will stick to it. This corresponds to a virtual water layer of sufficient thickness to catch every impacting ice crystal. The importance of the water layer on the impingement was discussed in Section 2.8. In this section also the lack of experimental data was pointed out, required to calibrate and validate the influence of the water layer in the impingement model of among others Villedieu et al. [40]. From Figure 2.15 the influence of an impingement model on the catching efficiency is shown. A reduction of 40% is seen in the stagnation point between a simulation with no impingement (similar to the model introduced in this report) and the results from experiments.

Unfortunately not much details are given regarding their impingement model by Wright et al. in [43]. Thereby no results are presented by Wright et al. in the form of for instance the mass flux of unfrozen runback water along the surface [43]. This lack of information makes it difficult to quantitatively compare results and to give a sound explanation for the difference in erosion factors.

4.2 Evaporation

In the early development phase of the mixed-phase icing model introduced in this report, the evaporative model used in other ice accretion codes such as Droplerian and LEWICE was carefully revised. The motivation behind this was the lack of supporting information on the evaporative model. During this part of the research presented in Section 2.5 it became clear that the influence of evaporating mass is only very small. In the test cases presented in the remainder of this chapter, the evaporative mass was less than one percent of the total impinging mass for every single case. The total impinging mass is without the ice crystal mass lost due to the erosive model.

This justifies the decision to keep the evaporative heat loss out of the energy balance. Although this introduces an extra inaccuracy, it is compensated by the reduced complexity of the ice accretion model introduced in Section 3. The dependency of the evaporative mass flux on the surface temperature would require the need of an iterative procedure for solving the surface temperature. Compared to the inaccuracy introduced by the empirical erosion model described in Section 2.7, the additional inaccuracy from leaving the evaporation out of the energy balance is negligible.

4.3 HAIC benchmarks

From the four test cases issued by HAIC, only test case 7 and test case 9 are evaluated in this report.

4.3.1 Test case 7 - The crowned cylinder

The results presented as a reference here are taken from the work of Currie et al. [11]. The ice particles and water droplets are size dependently divided over 7 bins as shown in Table 3.3. Run 47, 57 and 67 are performed under equal flow conditions (see Table 3.4) but vary in total water content (TWC) and melt ratio. Note that the temperature of the particles is set at the freezing temperature of 273.15 Kelvin, whereas the free stream temperature is above the freezing temperature. This corresponds to the environment hypothesized by Mason et al., stating that the ice crystals will (partly) melt, which enables them to stick to the surface forming a suitable location for other crystals to adhere. In the model introduced in this report, the fraction of ice crystals that have melted is added to the impinging water droplets. The flow conditions in Run 238 deviate from the other three runs, featuring

a higher Mach number of 0.4 versus 0.25 for the other runs. The differences in melt ratios are shown in Table 3.5.

Run 47 results by Currie et al. are shown in Figure 4.2a. The ice layers are the result of the crowned cylinder being exposed to mixed-phase icing conditions for 61 and 320 seconds. Whereas the icing exposure time is more than five times longer, the ice layer thickness is merely doubled in Figure 4.2a. Near the stagnation point of the crowned cylinder (Y location equals zero) the ice layer thickness is doubled. More close to the sides of the cylinder (Y location equals $\pm$ 10) however, the thickness of the ice layer is practically independent of exposure time. Hence, the shape of the ice layer is expected to change into a more pointy shape with increasing icing time.

This behaviour is not visible in the results presented in Figure 4.2b, obtained using the in this report presented model. These results display a more linear behaviour towards the increase in ice layer thickness with increased icing time. As a result from this, the presented ice shapes are not very pointy.

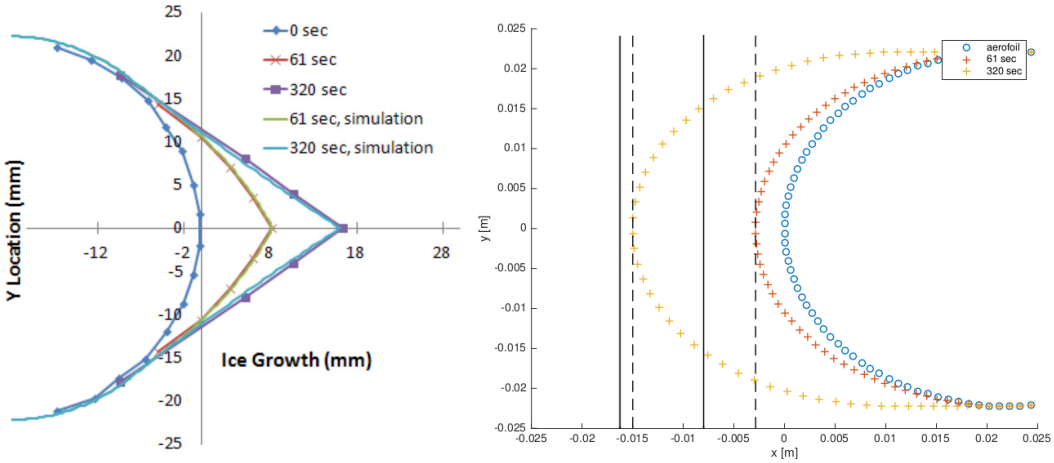

(a) Ice shape results from Currie et al..

(b) Ice shape results from the current model.

Figure 4.2: Experimental and numerical results of test case 7 Run 47. The melt ration η equals 6%, with a TWC (total water content) of 4 [g/m^3] [11].

The reason why Currie et al. are able to reproduce the experimental results with their numerical model is that their model is specifically designed for this test case. From previous work by Currie et al. [10] can be learned that they use a semi-empirical model, based on observations from earlier test runs. Using the initial growth rate and the final steady state ice shape, the ice shapes at intermediate times are predicted. The amount of impinging particles is not determined by numerically solving the flow field around the crowned cylinder. Instead the value of impingement at the stagnation point is found from experiments. To account for every position on the cylinder (all Y positions unequal to zero in Figure 4.2a) this value is multiplied with a correction factor. This correction factor is dependent of the angle between the normal vector of the surface and the flow [10].

Run 57 differs from Run 47 in having a TWC (total water content) which is three times larger than the TWC from Run 47. The melt ratio η is slightly lower. Three icing times are revised, 40, 116 and 290 seconds. Results from Currie et al. are shown in Figure 4.3a. The results obtained using the model described in this report are shown in Figure 4.3b. As a result of the higher level of TWC in Run 57, the thicknesses of the accreted ice layers are larger compared to Run 47, despite the shorter icing exposure times.

Note that although the shape of the predicted ice shape is much off the experimental one, the ice thickness at the stagnation point is only slightly under predicted compared to the wind tunnel experiments. The shape of the predicted ice layer can probably be improved by using an alternative formulation for the erosive action from impacting ice crystals. In the model introduced in this report

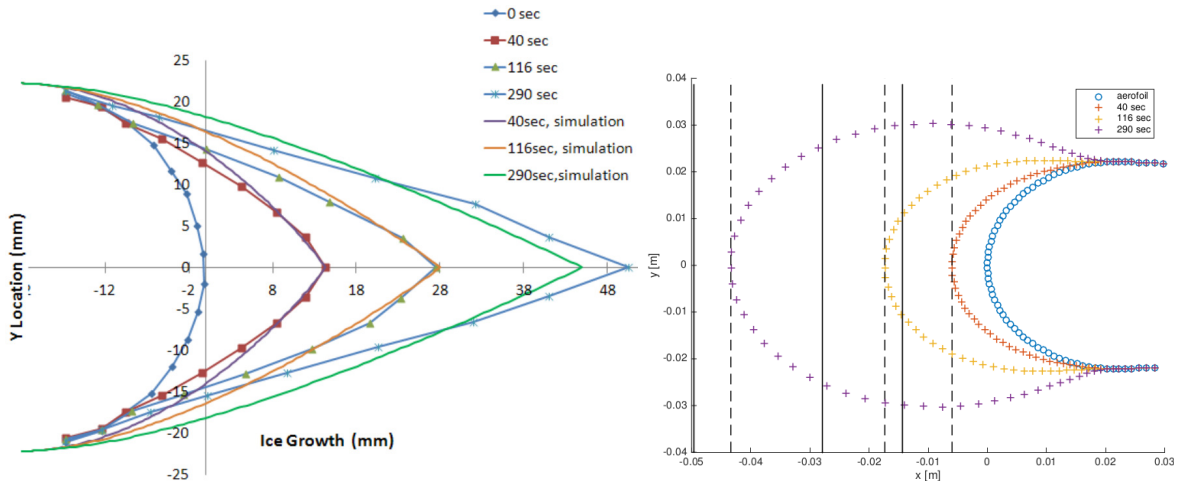

(a) Ice shape results from Currie et al..

(b) Ice shape results from the current model.

Figure 4.3: Experimental and numerical results of test case 7 Run 57. The melt ration η equals 14%, with a TWC of 12 [g/m^3] [11].

the empirical approach by Wright et al. [43] and introduced in Section 2.7 is applied. This method equally reduces the amount of impacting ice crystals for every position on the surface. Hence this will not influence the resulting shape of the ice layer, only its thickness. A model which takes into account the angle at which the particles impact the surface will be of influence on the shape of the ice layer. Such a model is suggested by Currie et al. in [11].

Run 67 The results as presented by Currie et al. are shown in Figure 4.4a. The results from the model presented in this research are shown in Figure 4.4b. From the longest icing time of 600 seconds is learned that the so called plateau phase when the ice layer thickness is no longer increasing with time is not accounted for in the proposed model. This was not anticipated for during the design of the model, hence as expected the thickness continues to increase with time.

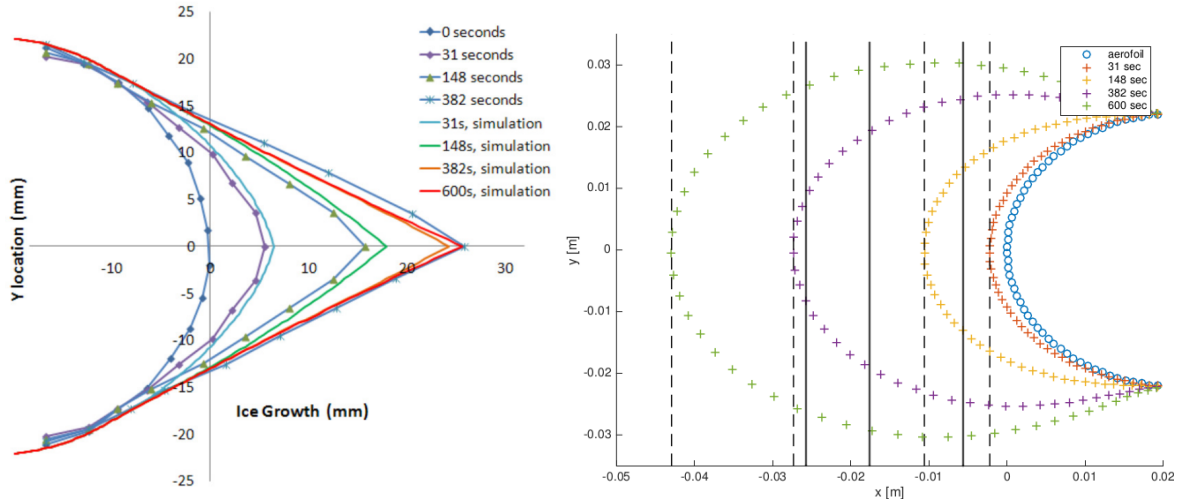

(a) Ice shape results from Currie et al..

(b) Ice shape results from the current model.

Figure 4.4: Experimental and numerical results of test case 7 Run 67. The melt ration η equals 16.6%, with a TWC of 6 [g/m^3] [11].

Run 238 Shown in Figure 4.5a are the results as presented by Currie et al.. The results from the model presented in this research are shown in Figure 4.5b. According to Currie et al. [11] the resulting ice layer is independent of the total water content (TWC) for higher Mach numbers. This is shown in Figure 4.5a, where the two lines closest to the surface are the results from the wind tunnel experiments [11]. The results from the model presented here do not show this behaviour. This is due to no impingement model being applied, which would incorporate such behaviour.

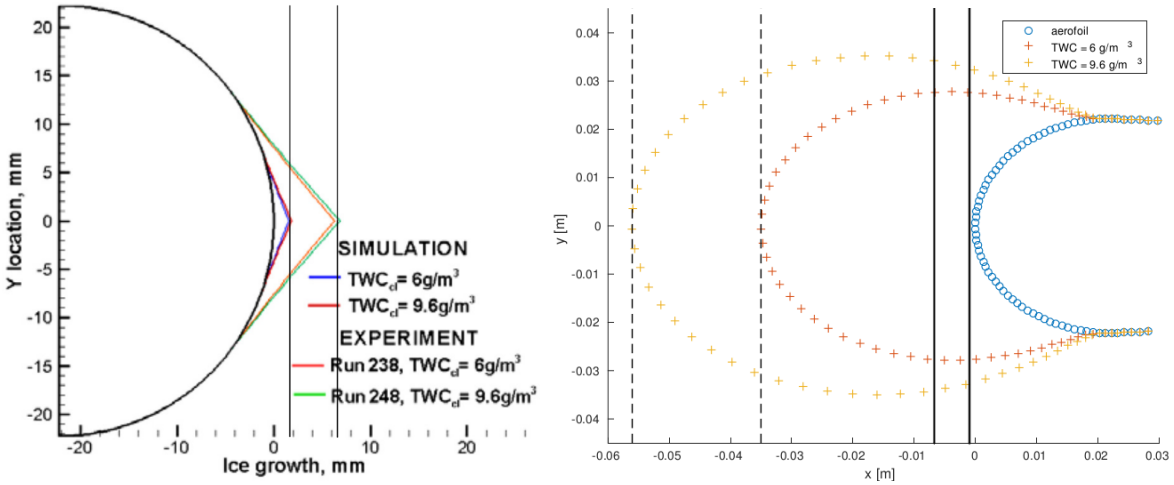

(a) Ice shape results from Currie et al..

(b) Ice shape results from the current model.

Figure 4.5: Experimental and numerical results of test case 7 Run 238. The melt ration η equals 14%, with a TWC of 6 [g/m^3] [11].

4.3.2 Test case 9 - NACA0012

The results presented here as a reference are from the work of Nilamdeen and Habashi [28]. Every ice particle is assumed to have the same diameter. The ice particle diameters are 150 μm for Run 19 and Run 20, and 200 μm for Run 10. Run 9 consists of water droplets only, with a diameter of 20 μm. The diameter of the water droplets is the same for every run.

According to the HAIC test case description, this test case is designed to gain insight in the behaviour of the model with respect to erosion [41]. In the ice accretion model introduced in this report it is assumed that all that ice crystals and water droplets that hit the surface will stick to it. Therefore it is not taken into account that ice crystals may bounce of from the surface, possibly break up into smaller crystals, and re-enter the flow. This effect is therefore also covered for by the erosion term.

The temperatures during the experiments of test case 9 (see Table 3.8) were below the freezing point. This resulted in a glaze ice layer for Run 9 and 10 and rime ice in Run 19 and 20. When supercooled water droplets impact a surface which has a temperature below freezing temperature, they instantly freeze to the surface. Ice crystals bounce off from such a surface and do not contribute to the ice accretion. The impacting ice crystals do however provide for erosive action, resulting in a reduction of the ice layer thickness. This is clearly visible in Figure 2.14 which shows photographs of the accreted ice in test case 9 from wind tunnel experiments performed by Al-Khalil et al. [3].

Run 9 and 10 results are shown in Figure 4.6. Additional results, which are not presented here, show the presence of runback water and a surface temperature equal to the freezing temperature. This suggests glaze ice conditions, which is in accordance with the wind tunnel experiments. The shape of the accreted ice does however not display the characteristic irregular glaze ice shape that can be seen in Figure 2.14d. This is due to the absence of a feedback loop between the model calculating the flow field and the particle impingement and the ice accretion model. The asymmetrical shape of the graphs in 4.6e is believed to be caused by the even amount of elements in the discretization of the

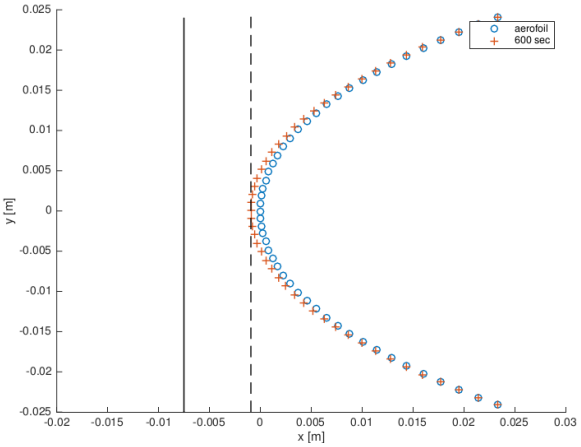

(a) Run 9. LWC is 0.7 and IWC is 0 [g/m^3].

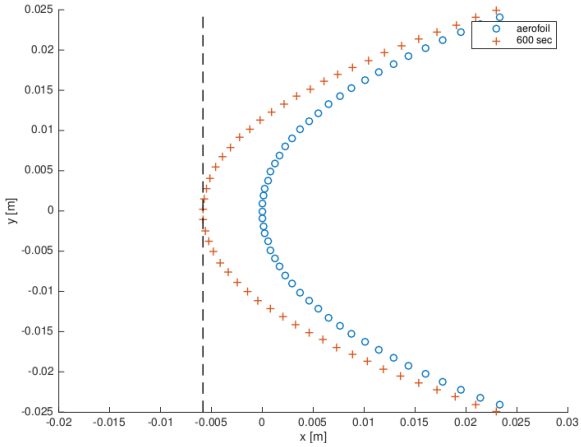

(b) Run 10. LWC is 0.7 and IWC is 0.7 [g/m^3].

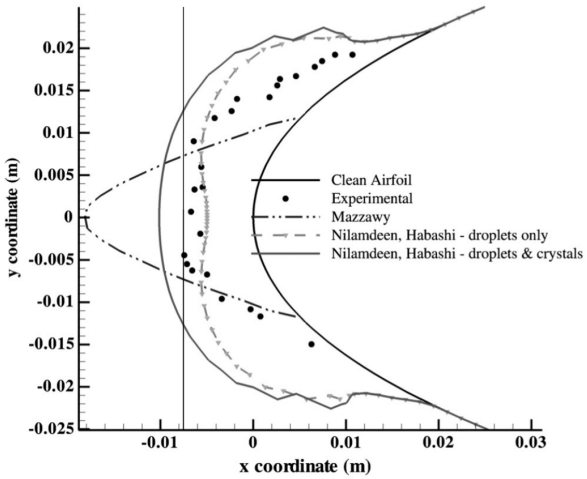

(c) Run 9 experimental and numerical. For "Nilamdeen, Habashi - droplets & crystals" IWC is 0.7 [g/m^3] [28]

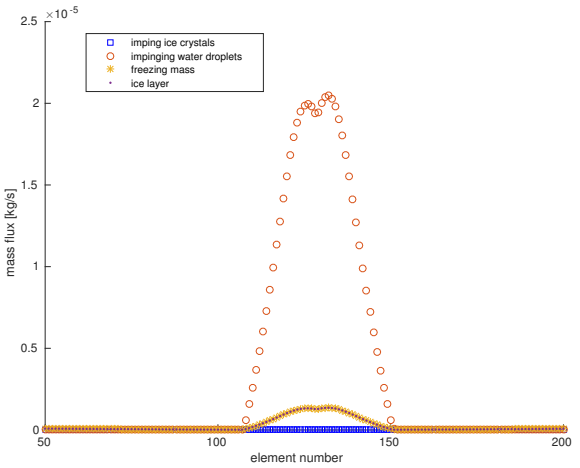

(d) Run 9 freezing and impinging mass.

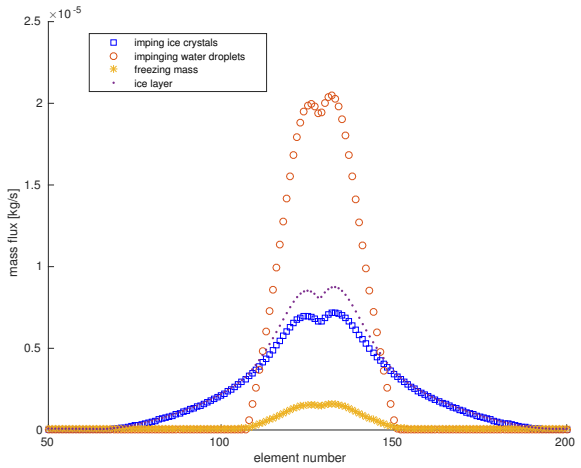

(e) Run 10 freezing and impinging mass.

Figure 4.6: Experimental and numerical results of test case 9, Run 9 and 10.

surface of the aerofoil. Therefore the stagnation point determined by the ice accretion model lies just above the location of the actual stagnation point. The actual stagnation point is located in between two elements. When the stagnation point was moved to the other element the symmetry was indeed

mirrored. Please note that this applies to all the mass flux and temperature graphs in the report create by the ice accretion model.

Ideally the flow field around the aerofoil and the particle impingement would be recalculated multiple times during a period of ice accretion. This incorporates the change in properties of the aerofoil due to the accreted ice layer in the calculation of the flow field and the impingement model. Nilamdeen and Habashi employ such a feedback loop, which relates the thickness of the water layer on the surface to the amount of ice crystals that stick to the surface [28].

The model presented in this research under-predicts the thickness of the ice layer in Run 9. A possible explanation for this is the initial assumption of the surface temperature being equal to the temperature of freezing. Effectively the model freezes a certain amount of the incoming water droplets which have a temperature below freezing, until enough heat is released to have the temperature of the surface element equal the freezing temperature. In the wind tunnel experiments however, the surface upon which the droplets imping has a temperature below freezing. The droplets freeze upon impact, whilst their kinetic energy will melt some part of the ice present in the control volume. The aerofoil itself can act as a heat sink in this process, absorbing a certain amount of kinetic energy. The model introduced in this report allows the coexistence of water and ice in the control volume only when the surface temperature is equal to the freezing temperature. This is the result of the assumption that no temperature gradient exists in the control volume. In reality however it might be the case that the temperature directly at the surface is of a below freezing temperature, whilst at the top of the accreted ice layer, the temperature is higher due to the effect of impinging droplets.

Contrary to the results from wind tunnel experiments by Al-Khalil et al. in [3] shown in Figure 4.6c, between Run 9 and 10 the ice layer thickness increases when ice crystals are added to the impinging flow. The impacting and freezing mass fluxes for Run 9 and Run 10 are shown in Figure 4.6e and Figure 4.6d. These graphs indicate that the increase in ice layer thickness between Run 9 and Run 10 is due to the presence of ice crystals. In the model introduced here, it is assumed that all the ice crystals contacting the surface stick to it and move into the ice layer. This not in line with the conclusions from Al-Khalil et al. in [3]. They states that the presence of ice crystals in Run 10 reduces the thickness of the ice layer with respect to Run 9. This is clearly visible in Figure 2.14. Note that in Figure 4.6d and 4.6e the elements are numbered clockwise starting from the trailing edge. The leading edge is positioned at element number 129. Element numbers above 129 and correspond to the top side of the aerofoil, numbers below 129 to the bottom.

Run 19 and 20 results are shown in Figure 4.8. Similar to Run 9 and Run 10 the here introduced model predicts a surface temperature which is in every element equal to the freezing temperature. This indicates, contrary to the wind tunnel experiments by Al-Khalil et al. [3], glaze ice is being formed. The presence of runback water confirms this. Similar to Run 10, the ice layer on the surface is mainly formed by the impinging ice crystals. This can be seen in Figure 4.8e from the small amount of freezing mass, which denotes the liquid water freezing into the ice layer. The freezing mass curve in Figure 4.8e starts to rise with the curve showing the amount of impacting droplets.

The impact locations of the droplets is more centred around the stagnation point whereas the ice crystals also impact on locations at a longer distance from the stagnation point. The explanation for this is the diameter of the ice particles which is 7.5 times larger than the diameter of the water droplets. This will influence the drag force they eparagraphxperience. As was stated in the Section 1.4, the drag force is of major influence on the trajectory of a particle [17]. At the locations where only ice crystals impact the surface, the curve showing the growth rate of the ice layer and curve for the impacting ice crystals almost coincide. This is shown in Figure 4.7a, offering an enhanced view of the edge of ice crystal impingement in Figure 4.8e.

Unfrozen water from upstream elements enters the control volume as runback mass. A fraction of this runback water freezes, making up for the freezing mass in the regions with no water droplet impingement in Figure 4.7a. A typical graph of the runback water flux in test case 9 is shown in Figure 4.7b. The mass flux of runback water which decreases with increasing distance from the leading edge indicates that water continues to freeze (with constant rate) to the surface.

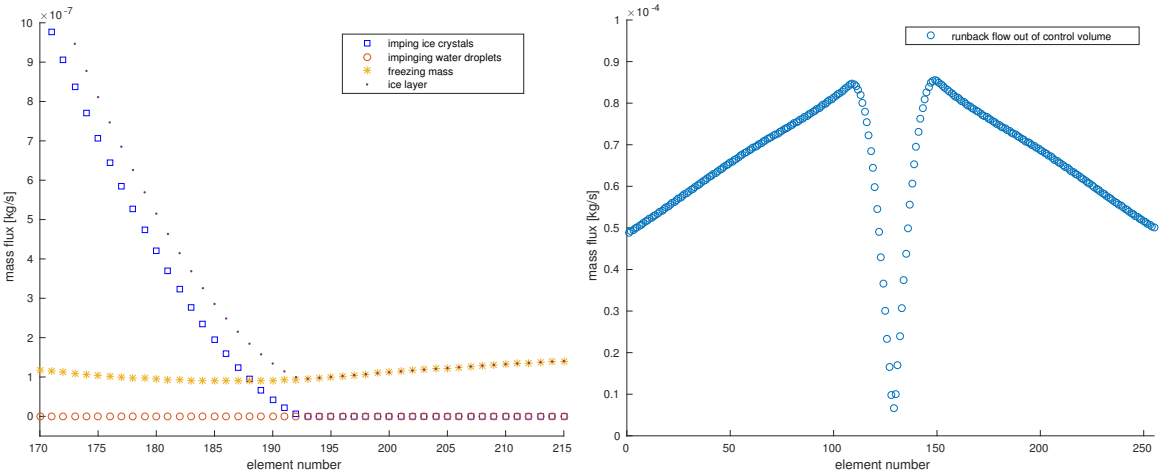

(a) Enhanced view of the freezing and impinging mass.

(b) Graph of the mass flux of runback water.

Figure 4.7: Numerical results of test case 9 Run 19.

4.4 General model behaviour

A parameter study is used to revise the behaviour of the model. Run 19 from test case 9 is used as the base model for this study. The original parameters of this run are a freestream, particle and droplet temperature of 262.05 Kelvin. The total water content (TWC) is 1 g/m^3, with a ice water content (IWC) and liquid water content (LWC) of 0.7 and 0.3 g/m^3 respectively. Although the ice water content is relatively low in test case 9 compared to test case 7, this is compensated for the longer ice accretion time of 600 seconds. In reality the IWC will also be higher, as stated in Section 1.1, values up to 8 g/m^3 are reported by Mason et al. in [24]. Since the impact of ice crystals in test case 9 is more widely distributed over the surface compared to the water droplets, this makes for ideal conditions to revise the influence of the water droplets and ice crystals individually.

The total water content dependency of the outcomes from the model introduced in this report is tested by gradually increasing and decreasing the TWC by a factor of ten. The ratio of 7:3 between the IWC and LWC remains unchanged.

With increasing TWC, the thickness of the ice layer increases linearly. Since no limitations are set to the maximum ice layer thickness it is allowed to grow to unrealistic proportions. An extension to the current erosive model which increases the erosive reduction factor with increasing ice layer thickness could possible account for this. The freezing mass rate is also seen to increase linearly with TWC. The temperature at every location on the surface remained equal to the temperature of freezing when the TWC was increased.

With decreasing TWC, the temperature profile of the surface is seen to change. This behaviour is graphically displayed in Figure 4.9. Less runback water flowing out of the control volume is available for the lower values of the TWC. Hence, less water can freeze to the surface at locations further downstream from the stagnation point. When no mass is available for freezing, it is impossible to maintain the assumption of the surface temperature being equal to the freezing temperature. To restore the energy balance, the surface temperature is then lowered to match the recovery temperature. In Figure 4.9b the surface temperature drops below the recovery temperature in the elements left of number 101 and right of 157. This is caused by the ice crystals still impacting those surface elements. The result is that the surface temperature is required to drop even below the recovery temperature in order to balance the energy terms. In Figure 4.9c the graph of runback water grows far beyond the maximum value of the other graphs. Therefore a range is chosen which provides a better view of the other graphs, which are of greater interest.

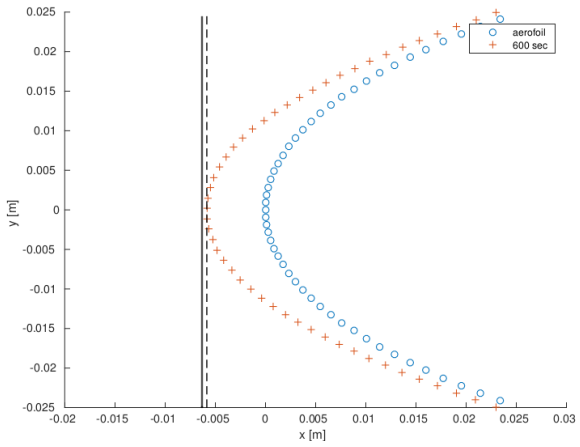

(a) Run 19. LWC is 0.3 and IWC is 0.7 [gm^{-3}].

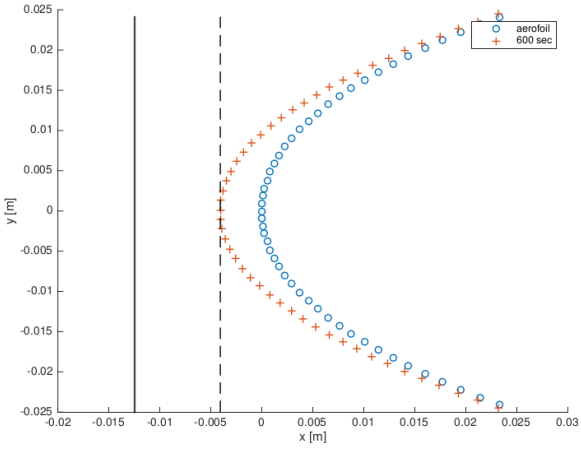

(b) Run 20. LWC is 0.7 and IWC is 0.3 [gm^{-3}].

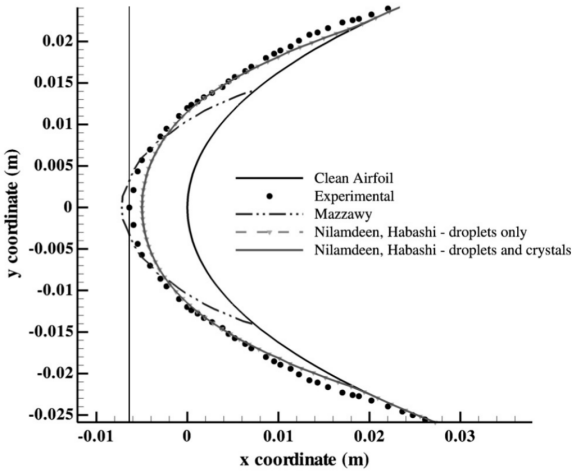

(c) Run 19 experimental and numerical [28].

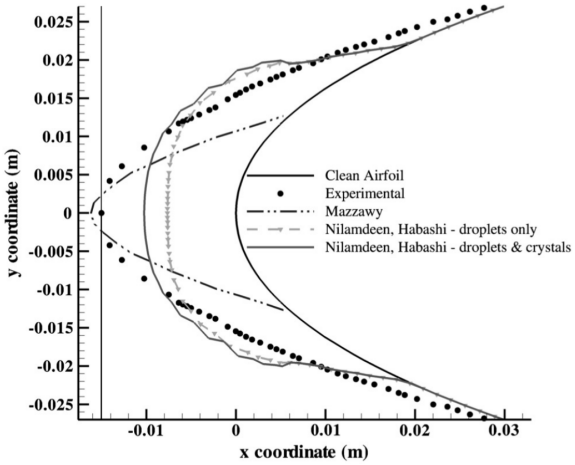

(d) Run 20 experimental and numerical [28].

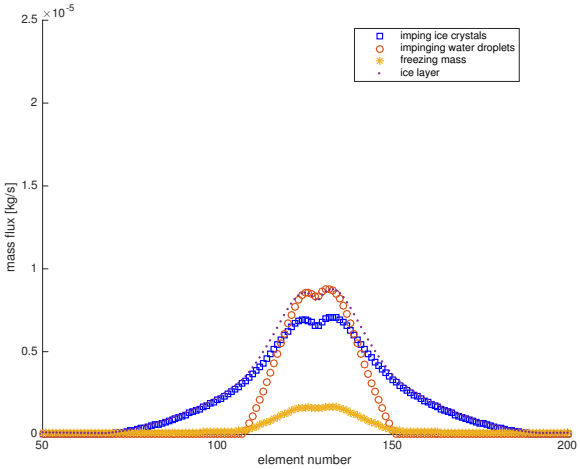

(e) Run 19 freezing and impinging mass.

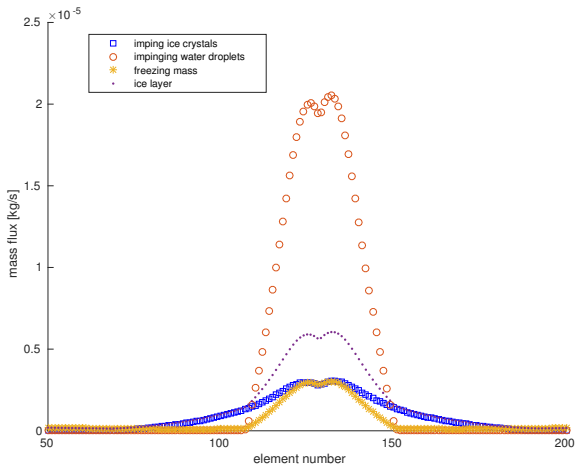

(f) Run 20 freezing and impinging mass.

Figure 4.8: Experimental and numerical results of test case 19 and 20.

The temperature dependency of the outcomes from the model introduced in this report is tested by gradually increasing and decreasing the temperature of the free stream and the impinging ice crystals and water droplets. The IWC and LWC values from Run 19 in test case 9 are maintained.

While the temperature of the impinging droplets and the flow at infinity upstream are increased, the temperature of the impinging ice crystals is set to the freezing temperature. Shown in Figure 4.10

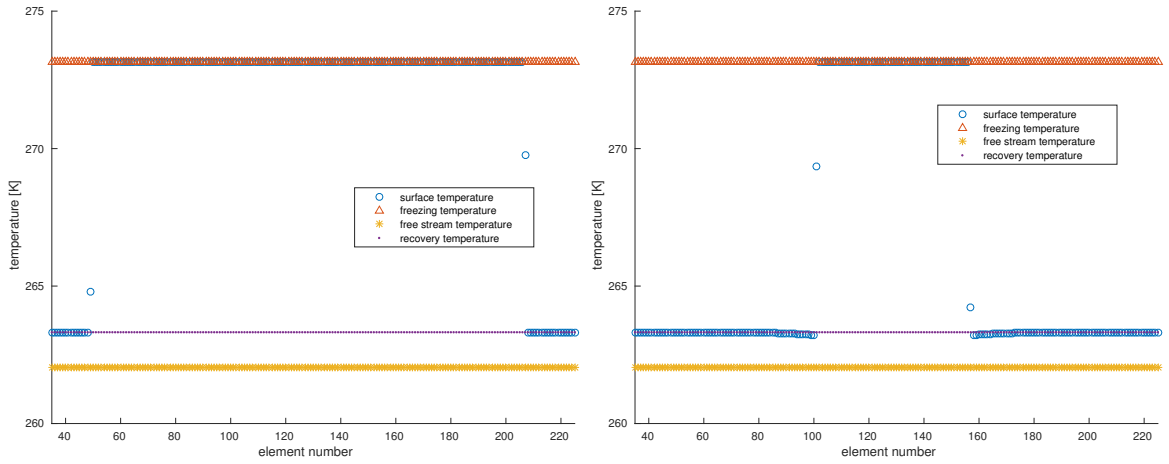

(a) Temperatures for 10% LWC_0.

(b) Temperatures for 1% LWC_0.

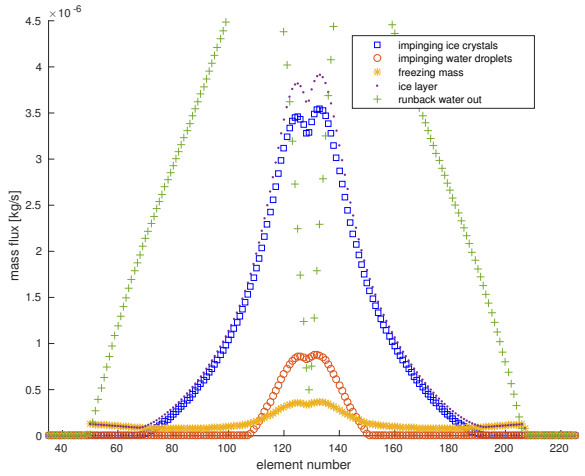

(c) Mass fluxes for 10% LWC_0.

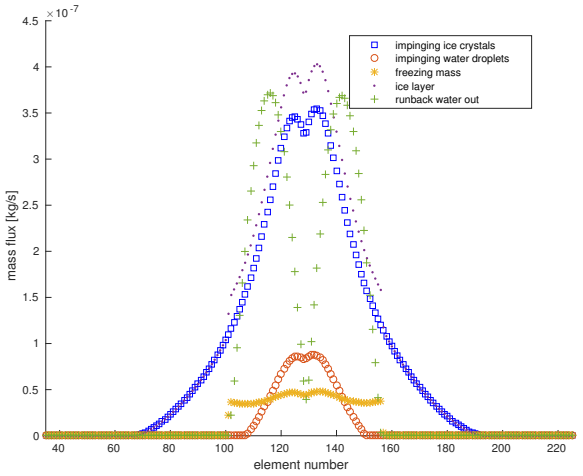

(d) Mass fluxes for 1% LWC_0.

Figure 4.9: Variation in temperature and mass fluxes for different values of LWC. The LWC_0 denotes the conditions for test case 9, Run 19.

are the temperatures and mass fluxes at the surface. Note that the negative freezing mass indicates that a fraction of the impinging ice crystals is melting. The runback water increases rapidly with the distance from the stagnation point. At the positions where no ice crystal impact the surface it reaches it maximum value. This value is about 4 times larger than the peak of the impinging ice crystals. With increasing temperatures of the impinging water droplets and the free stream, this effect will grow stronger. At some point, the temperature of the impinging droplets will be sufficiently high to melt all the impinging ice crystals. This is not a very realistic scenario, since there are more ice crystals impinging the surface than there are water droplets (ratio 7:3). Moreover the latent heat of freezing is about 80 times larger than the specific heat of water. At positions where no ice crystals impact the surface, only liquid water is present in the control volumes.

When the temperature of the free stream and impinging crystals and droplets are decreased, it is assumed that rime ice conditions will occur. In the wind tunnel experiments for Run 19 of test case this was indeed the case for the prescribed flow conditions. The model introduced in this report did not show this behaviour for the specified temperatures. As is shown in Figure 4.11a and Figure 4.11b, the temperatures need to drop below 246 Kelvin to achieve rime icing everywhere on the surface. For temperatures between 246 and 258 Kelvin glaze ice occurs in the vicinity of the stagnation point. The remaining runback water freezes at locations further downstream towards the trailing edge. Hence in the vicinity of the trailing edge neither ice or water are present on the aerofoil. The results in this temperature range are equal to the results from a low TWC such as shown in Figure 4.9b and Figure 4.9d.

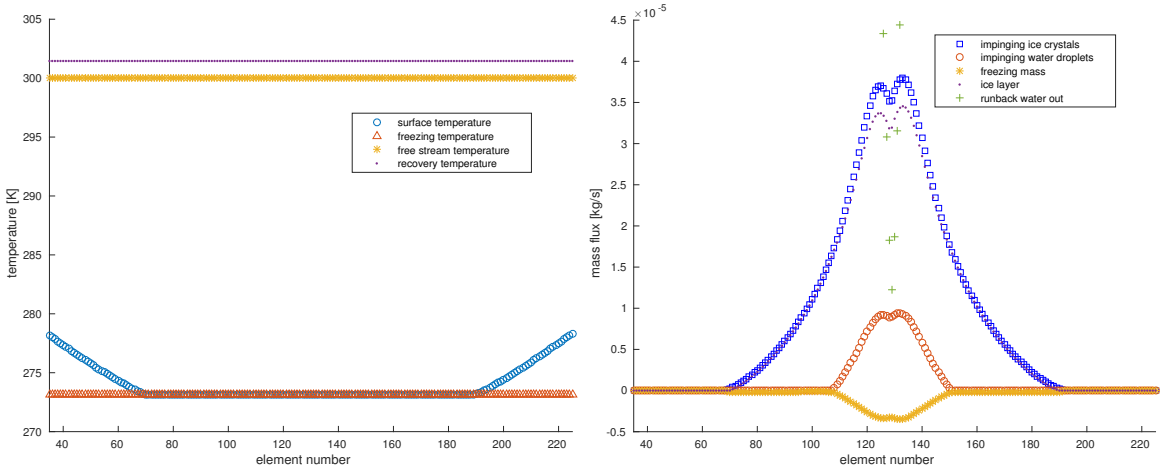

(a) Temperatures. (b) Mass fluxes.

Figure 4.10: Variation in temperature and mass fluxes for $T_\infty = T_{imp,d} = 300$ Kelvin, $T_{imp,ic} = 273.15$ Kelvin. Due to the increased temperature a negative freezing rate is found. The remaining test conditions correspond to test case 9, Run 19.

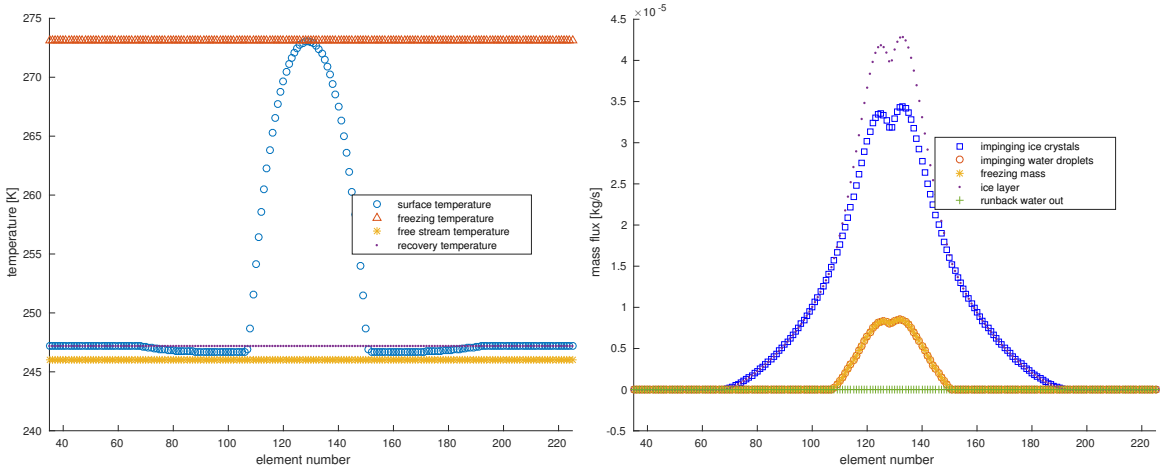

(a) Temperatures. (b) Mass fluxes.

Figure 4.11: Variation in temperature and mass fluxes for $T_\infty = T_{imp,d} = T_{imp,ic} = 246$ Kelvin. This is the largest value of the temperature for which only rime ice is present on the surface. The remaining test conditions correspond to test case 9, Run 19.

Chapter 5

Conclusions and recommendations

The most important conclusion from this research is that the mechanisms of erosion and particle impingement are very important for a mixed-phase ice accretion code. Without precise knowledge of the amount of ice crystals and water droplets sticking to the surface it is not possible to accurately predict the thickness of the resulting ice shape. Similar for the erosive modelling. A relatively simple model can be used to estimate the amount of mass lost due to erosive action by impacting ice crystals. It is however proven that such a simple model will not accurately predict how the erosion influences the shape of the ice layer.

5.1 Particle impingement

The design of a particle impingement model was not anticipated for in this research. The particle impingement is planned to be taken into account with the model calculating the flow field around the aerofoil. The development of this flow model is still in progress. Therefore it has been assumed in this research that every crystal and droplet impinging the surface will stick to it.

The absence and importance of such a particle impingement model is demonstrated by the results of Run 9 and Run 10 from test case 9. These results are discussed in Section 4.3.2. Regarding Run 10 Al-Khalil et al. conclude in [3] that compared to Run 9, the additional ice crystals in Run 10 do not contribute to the formation of the ice layer. Instead the ice crystals reduce the ice layer thickness due to erosive action. This is best visible in Figure 2.14b. The assumption that all the ice crystals stick to the surface results in the increase of the ice layer as is shown in Figure 4.6b. Instead of decreasing in size in Run 10, the ice layer grows to about five times the size of Run 9. Therefore it is concluded that a particle impingement model is required to increase the accuracy and generality of the ice accretion model.

Regarding the particle impingement model a number of recommendations can be made. Motivated by the results from Run 9 and 10 in test case 9 it is advised to incorporate the water layer thickness into the particle impingement model. Such a feedback loop is for instance used by the mixed-phase ice accretion codes developed by INTA and ONERA introduced in Section 2.6.3. A different impingement model is introduced by Nilamdeen and Habashi [28]. In this report this model is discussed in Section 2.8. Albeit being a proof of concept model, it does provide an interesting insight in the mechanisms involved in ice crystal impingement. To circumvent the requirement of a feedback loop, it would also be interesting to look into the model of Currie et al. [11] which was introduced in Section 2.8. This model relates the LWC to the fraction of crystals that sticks to surface. Due to a lack of research and experimental data it is difficult to compose a physically solid relation between the water layer thickness and the sticking rate. Therefore a model using the LWC might currently perform as good as a water film thickness model, without the trouble of a feedback loop.

A good impingement model should also take into account that ice crystals may break up into pieces upon impact, re-enter the flow field and impact on the surface further downstream. Important in this process is what happens with kinetic energy of the particle. As discussed in Section 2.8 some of it can

be used by the particle to bounce from the surface back into the flow field. The remaining fraction is transferred to the surface. As discussed in Section 4.3.2, the kinetic energy will melt some of the ice present in the control volume. Therefore this is an important mechanism. As an example of a model relating the shattering and bounce mechanism to impact velocities and particle properties, the model suggested by Villedieu et al. in [40] is introduced in Section 2.8. One of the conclusions of Villedieu et al. is that still more research and experimental work is required to gain better insight in these mechanisms and to derive better models [40].

The impingement model can be even further extended following the idea of Currie et al. [11]. They suggest an effect that occurs at higher Mach numbers such as in test case 7 Run 238. This reduces the energy of newly impinging particles by colliding with particles that already have bounced from the surface. After the collision both particles impinge the surface with a lower velocity, making them suitable candidates to stick to the surface.

5.2 Erosion

The model for erosion used in this research is acceptable. The predicted ice layer thicknesses in test case 9 and around the stagnation point in test case 7 are within reasonable limits of accuracy compared to the results from wind tunnel experiments. The reduction factor of 80% found in Section 4.1 is pretty large. Especially with retrospect taken to the value of 20% found by Wright et al. in [43]. This might however be explained due to the lack of an impingement model in the newly introduced ice accretion model. It is still advisable to look into a more sophisticated model for the erosive action.

The numerical model used by Currie et al. in [11] incorporates the angle between the surface and the impinging particles. This would be of influence on the resulting shape of the ice layer. Counter intuitive in this method is that the mass lost due to erosion is subtracted from the impinging ice crystal mass. Taking into account the mechanism of erosion, it would make more sense to calculate the force an impacting particle exerts on the surface. Dependent of the magnitude of the force a fraction of the ice layer is removed from the surface.

5.3 Test case results

The results from the test cases are presented in Section 4.3. Compared to the numerical results from other authors also presented in Section 4.3 the differences are quite extensive. Bearing in mind that the aim of this research was to develop a generally applicable mixed-phase icing model puts this in perspective. The numerical model proposed by Currie et al. in [11] is specifically designed around test case 7. The numerical model used by Wright et al. in [43] for test case 9 is simply in a further state of development. They built it on the well established NASA GlennICE software, which is the result of a combination of all the icing codes and knowledge available at NASA.

Compared to the wind tunnel experiments, the results from shorter icing times in test case 7 and runs with ice crystals in test case 9 give satisfactory results. In test case 7 this is mainly due to the ambient conditions being equal to the freezing temperature. For test case 9 this it probably due to the presence of ice crystals in the flow. This gives rise to the conclusion that the in this report introduced mixed-phase icing model performs best in conditions where the ambient conditions are equal or close to the freezing temperature and when the ice crystal content exceeds the liquid water content.

5.4 Validation and verification

The topic of model validation and verification was introduced in Section 3.5. It was simply stated that validation deals with building the right model and that verification is about building the model right.

Some of the mechanisms for model verification in Section 3.5 are pretty straight forward. At the same time, some of them are practically impossible. The less complex mechanisms were executed naturally during the design and development phase. These mechanisms include checking the syntax for errors, discussing it with other people and testing individual parts of the code to check if they perform as they are supposed to. Stress testing and a constraint analysis were performed with the parameter study described in Section 4.4. The total water content was increased and decreased to values beyond the limits of normal operation. In a similar fashion the ambient temperatures were increased and decreased. During this process the model displayed no unexpected behaviour.

The process of validation introduced in Section 3.5 can be executed simultaneously with the model verification. During the design and development phase results were discussed with experts on the topic of ice accretion. The comparison with other numerical models and wind tunnel experiments together with the parameter study contribute to the process of validation. From these can be concluded that within the vicinity of normal operating conditions such as a high ice crystal content and a temperature close to the freezing temperature, the output of the model and its response to input variations give a representation of reality which is acceptable within the framework of the HAIC project.

5.5 The updated model

The combination of all the recommendations from this chapter results in an updated version of the presented model. A suggestion for such a model is given in Figure 5.1. For convenience the current model is repeated in Figure 5.2. Here the icing exposure time is split up into multiple time steps. This allows to update the input conditions for the impingement and erosive model with increasing time. When the ice shape thickness exceeds a certain boundary, the flow solution should be updated. Although this is very time consuming, it will prove useful when is expected that the shape of the ice layer changes significantly with time. This is seen in test case 7. Here the ice layer has a pointy shape, whereas the surface itself is a round shape.

The updated model separates the impingement of ice crystals and water droplets. From the impinging droplets the water layer thickness is calculated. This is to ensure that in rime ice conditions the ice crystals will bounce from the surface. The energy balance will look different when also ice crystals are taken into account, who also contribute kinetic energy to the energy balance. Therefore an iterative procedure might be required to accurately solve this. Alternatively it might be sufficient to use a very small time step Δt.

Figure 5.1: Flowchart of the newly suggested solution procedure.

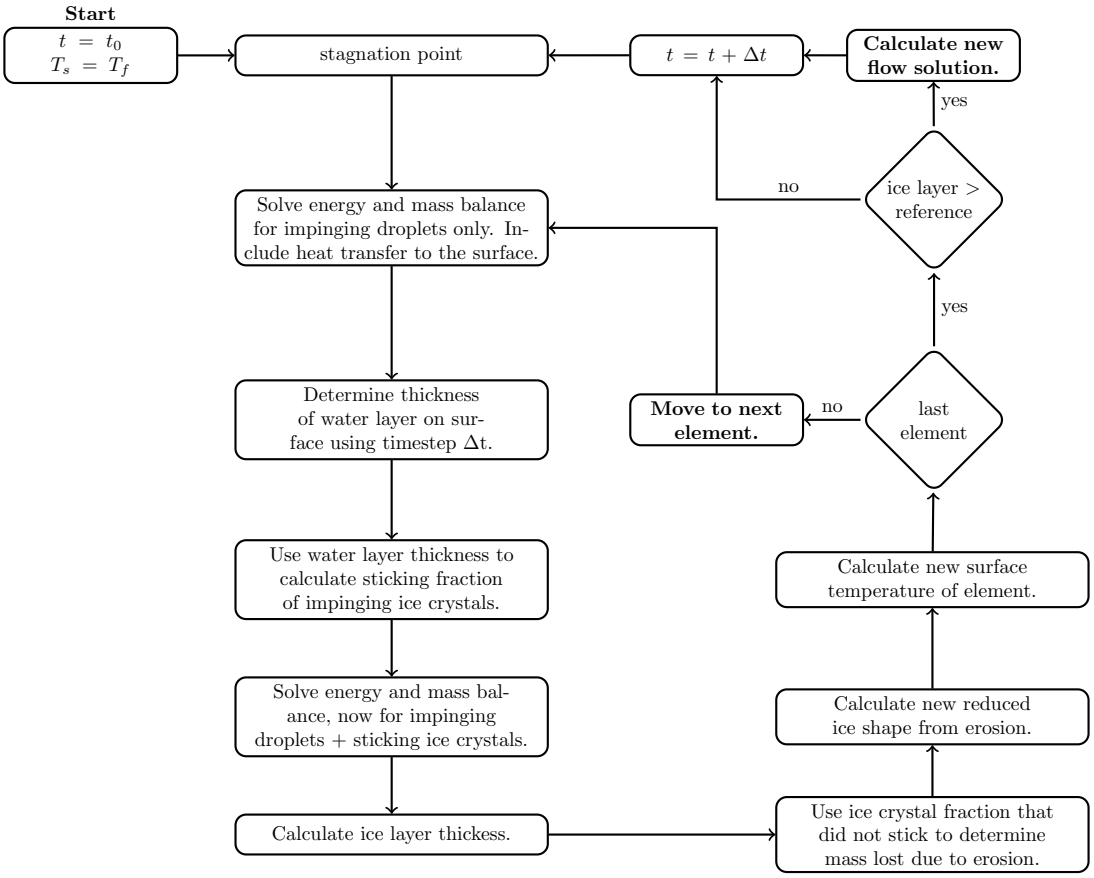

Figure 5.2: Flowchart of the in this report applied solution procedure.

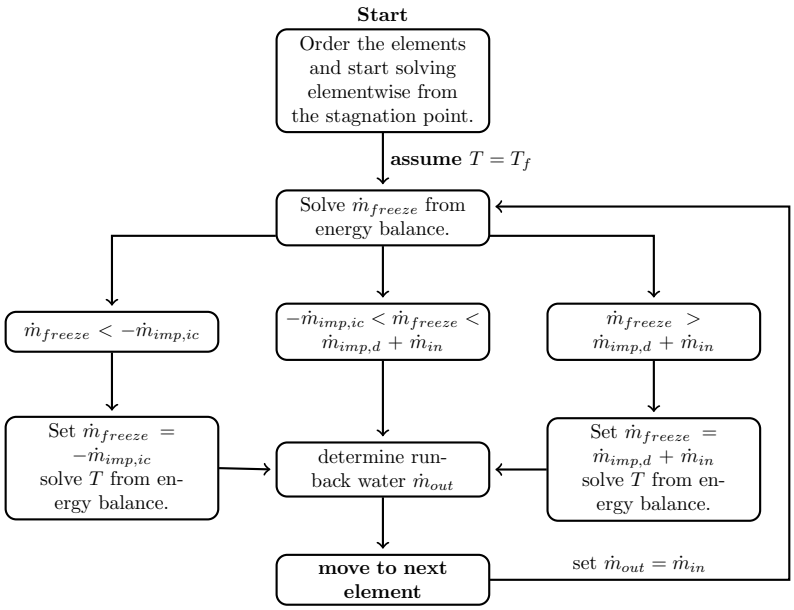

Bibliography

[1] High Altitude Ice Crystals project website, http://www.haic.eu, visited 01-11-2015.

[2] Aviation and space educational website aerospaceweb, http://www.aerospace.org, visited 08-11-2015.

[3] K. Al-Khalil, E. Irani, and D. Miller. Mixed-Phase Icing Simulation and Testing at the Cox Icing Wind Tunnel. Technical Report September, Glenn Research Center, 2003.

[4] C.N. Aliaga, M.S. Aubé, G.S. Baruzzi, and W.G. Habashi. FENSAP-ICE-Unsteady: Unified In-Flight Icing Simulation Methodology for Aircraft, Rotorcraft, and Jet Engines. *Journal of Aircraft*, 48(1), 2011. ISSN 0021-8669. doi: 10.2514/1.C000327.

[5] J.D. Jr. Anderson. *Introduction to Flight*. McGraw-Hill, 2012. ISBN 9780071086059.

[6] T.W. Brakel, J.P.F. Charpin, and T.G. Myers. One-dimensional ice growth due to incoming supercooled droplets impacting on a thin conducting substrate. *International Journal of Heat and Mass Transfer*, 50(9-10), May 2007. ISSN 00179310. doi: 10.1016/j.ijheatmasstransfer.2006.10.014.

[7] J. T. Cansdale and R. W. Gent. Ice accretion on aerofoils in two-dimensional compressible flow: a theoretical model. Technical report, Royal Aircraft Establishment, 1983.

[8] Y.A. Çengel. *Heat Transfer: A Practical Approach*. McGraw-Hill.

[9] T.C. Currie, P.M. Struk, J. Tsao, D. Fuleki, and D.C. Knezevici. Fundamental Study of Mixed-Phase Icing with Application to Ice Crystal Accretion in Aircraft Jet Engines. In *4th AIAA Atmospheric and Space Environments Conference*, number June, 2012.

[10] T.C. Currie, D. Fuleki, D.C. Knezevici, and J.D. MaCleod. Altitude Scaling of Ice Crystal Accretion. In *5th AIAA Atmospheric and Space Environments Conference*, San Diego, CA, 2013. doi: 10.2514/6.2013-2677.

[11] T.C. Currie, D. Fuleki, and A. Mahallati. Experimental Studies of Mixed-Phase Sticking Efficiency for Ice Crystal Accretion in Jet Engines. In *6th AIAA Atmospheric and Space Environments Conference*, number June, 2014.

[12] F. Dezitter, A. Grandin, J.L. Brenguier, F. Hervy, H. Schlager, P. Villedieu, and G. Zalamansky. HAIC (High Altitude Ice Crystals). In *5th AIAA Atmospheric and Space Environments Conference Aircraft Icing*, 2013.

[13] T. Hauk, I. Roisman, and C Tropea. Investiation of the Melting Behaviour of Ice Particles in an Acoustic Levitator. In *11th AIAA/ASME Joint Thermophysics and Heat Transfer Conference*, number June, 2014. doi: 10.2514/MTPHT14.

[14] H.W.M. Hoeijmakers. Lecture Notes - Fluid Dynamics. University of Twente, 2010.

[15] J. Holman. *Heat Transfer*. McGraw-Hill series in mechanical engineering. McGraw-Hill Education, 2009. ISBN 9780073529363.

[16] V. Horák, B. Hoení, and D. Rozehnal. Mathematical Simulation and Experimental Observations of Aircraft Icing. In *Proceedings of the International Scientific Conference Modern Safety Technologies in Transportation*, number September, Zlata Idka, 2007. ISBN 9788096976027.

[17] J.M. Hospers. *Eulerian method for super-cooled large-droplet ice-accretion on aircraft wings*. PhD thesis, University of Twente, 2013.

[18] E. Iuliano, D. Kintea, A.B. Miller, and P. Villedieu. Deliverable D6.5.1 - Literature review on mixed phase ice accretion models. Technical report, High Altitude Ice Crystals Consortium, 2013.

[19] E. Iuliano, P. Villedieu, and N. Caballero. Deliverable D6.5.2 - Final report on improved Messinger model for ice accretion in presence of ice crystals. Technical report, High Altitude Ice Crystals Consortium, 2014.

[20] E. Iuliano, E. Montreuil, E. Norde, E.T.A. van der Weide, and H.W.M. Hoeijmakers. Modelling of Non-Spherical Particle Evolution for Ice Crystals Simulation with an Eulerian Approach. *SAE Technical Paper*, (2015-01-2138), 2015. doi: 10.4271/2015-01-2138.

[21] S. Jacobs. Icing Simulation. Master's thesis, Twente University, 2005.

[22] S.J. Jacobs, J.M. Hospers, and H.W.M. Hoeijmakers. Numerical Simulation of Ice Accretion on Multiple-Element Airfoil Sections. In *26th Congress of International Council of the Aeronautical Sciences*, 2008. ISBN 9781605607153.

[23] P.K. Kundu, I.M. Cohen, and D.R. Dowling. *Fluid Mechanics*. Elsevier, 5th edition, 2012. ISBN 9780123821003.

[24] J.G. Mason, J.W. Strapp, and P. Chow. The Ice Particle Threat to Engines in Flight. In *44th AIAA Aerospace Sciences Meeting and Exhibit*, number January, 2006.

[25] B.L. Messinger. Equilibrium Temperature of an Unheated Icing Surface as a Function of Air Speed. *Journal of the Aeronautical Sciences*, 20(1), January 1953. doi: 10.2514/8.2520.

[26] D. M. Murphy and T. Koop. Review of the vapour pressures of ice and supercooled water for atmospheric applications. *Quarterly Journal of the Royal Meteorological Society*, 131(608), 2005. doi: 10.1256/qj.04.94.

[27] T.G. Myers. Extension to the Messinger model for aircraft icing. *AIAA Journal*, 39(2), 2001. doi: 10.2514/3.14720.

[28] S. Nilamdeen and W. Habashi. Multiphase Approach Toward Simulating Ice Crystal Ingestion in Jet Engines. *Journal of Propulsion and Power*, 27(5), September 2011. ISSN 0748-4658. doi: 10.2514/1.B34059.

[29] E. Norde. Splashing Model for Impact of Supercooled Large Droplets on a Thin Liquid Film. Master's thesis, University of Twente, 2013.

[30] N. Oreskes, K. Shrader-Frechette, and K. Belitz. Verification, Validation, and Confirmation of Numerical Models in the Earth Sciences. *Science*, 263(5147), 1994. ISSN 0036-8075. doi: 10.1126/science.263.5147.641.

[31] S. Özgen and M. CanIbek. Ice accretion simulation on multi-element airfoils using extended Messinger model. *Heat and Mass Transfer*, 45, 2009. ISSN 09477411. doi: 10.1007/s00231-008-0430-4.

[32] K.R. Petty and C.D.J. Floyd. A Statistical Review of Aviation Airframe Icing Accidents in the U.S. *11th Conference on Aviation, Range, and Aerospace Meteorology*, 54(March 1997), 2004.

[33] M. A. Rist and S. A. F. Murrell. Ice triaxial deformation and fracture. *Journal of Glaciology*, 44 (135), 1994. ISSN 0022-1430.

[34] B.M. Ruff, G.A., Berkowitz. Users Manual for the NASA Lewis Ice Accretion Prediction Code (LEWICE). Technical report, 1990.

[35] R.G. Sargent. Validation and verification of simulation models. In P. A. Farrington, H. B. Nembhard, D. T. Sturrock, and G. W. Evans, editors, *Proceedings of the 1999 Winter Simulation Conference*, 1999. ISBN 0-7803-8786-4. doi: 10.1109/WSC.2004.1371298.

[36] P.M. Sforza. *Theory of Aerospace Propulsion*. Elsevier, 2012. ISBN 9781856179126. doi: 10.1016/B978-1-85617-912-6.00012-8.

[37] H.H. Sogin. A design manual for thermal anti-icing systems. Technical report, Illinois Institute of Technology, 1954.

[38] P. Trontin, P. Villedieu, and D Kintea. Deliverable SP6 WP6.5 TRL4 Benchmark TC7. Technical report, High Altitude Ice Crystals Consortium, 2015.

[39] European Union. Commission Decision C4995, 2014.

[40] P. Villedieu, P. Trontin, and R. Chauvin. Glaciated and mixed-phase ice accretion modeling using ONERA 2D icing suite. In *6th AIAA Atmospheric and Space Environments Conferende*, number June, 2014.

[41] P. Villedieu, P. Trontin, and D Kintea. Deliverable SP6 WP6.5 TRL4 Benchmark TC9. Technical report, High Altitude Ice Crystals Consortium, 2015.

[42] R.B Whitner and O. Balci. Guidelines for selecting and using simulation model verification techniques. In *Proceedings of the 1989 Winter Simulation Conference*, 1989.

[43] W.B. Wright, P.C.E. Jorgenson, and J.P. Veres. Mixed Phase Modeling in GlennICE With Application to Engine Icing. In *Atmospheric and Space Environments Conference*, number August, Toronto, Ontario, 2010. doi: doi:10.2514/6.2010-7674.